

HERIOT-WATT UNIVERSITY

Femtosecond combs for optical frequency metrology

Veronika Tsatourian

July 2013

SUBMITTED FOR THE DEGREE OF
DOCTOR OF ENGINEERING IN PHOTONICS
ON COMPLETION OF RESEARCH IN THE
SCHOOL OF ENGINEERING AND PHYSICAL SCIENCES.

The copyright in this thesis is owned by the author. Any quotation from the thesis or use of any of the information contained in it must acknowledge this thesis as the source of the quotation or information.

Abstract

This thesis is dedicated to femtosecond combs as a tool for optical frequency metrology and as an integral part of an optical clock. After an overview of optical frequency measurement techniques, the design of two frequency combs based on mode-locked femtosecond lasers as they were at the beginning of my project is described. The first comb is based on an Er:fibre laser operating at a central wavelength of 1550 nm with a repetition rate of 100 MHz. The second is a Ti:sapphire-laser-based comb operating at a central wavelength of 810 nm with a repetition rate of 87 MHz.

Improvements to the original design of the Ti:sapphire comb are detailed in the next chapter. A novel f -to- $2f$ self-referencing scheme based on a pair of Wollaston prisms and employing a PPKTP crystal for SHG results in up to 20 dB enhancement of the signal to noise ratio in the carrier-envelope offset frequency beat signal f_0 and in up to 15 dB lower phase noise in the f_0 beat signal compared to a Michelson interferometer based system.

Next, the factors influencing the stability and accuracy of the microwave reference signal and the performance of two synthesisers used for the stabilisation of the frequency combs were investigated. It is shown that stability of the maser reference signal is reduced by the distribution system by factor of 1.5. A fractional frequency change of $4.1(0.7) \times 10^{-16} \text{ (K/h)}^{-1}$ was measured for the better of the two synthesisers (an IFR 2023A) indicating that for accurate frequency measurements the synthesiser signal should be monitored to enable systematic frequency corrections to be made.

Finally, an absolute frequency measurement of the electric quadrupole clock transition in a frequency standard based on a single $^{171}\text{Yb}^+$ trapped ion is described. The result $f = 688\,358\,979\,309\,310 \pm 9 \text{ Hz}$ agrees with an independent measurement made by the PTB group within the uncertainty of the measurements.

Acknowledgements

First of all, I would like to thank my supervisors, Dr Helen Margolis and Prof Deryck T. Reid. Their enormous support, encouragement and guidance were invaluable for the completion of this work.

I would also like to thank Dr Patrick Gill for useful discussions and critical views on the future of optical clock.

This work would not have been possible without the help of other members of the group. In particular, I am deeply grateful to Dr Stephen Lea for his help with the numerical simulations, and many useful discussions at the early stages of this work. It would be difficult to overestimate discussions with Dr Giuseppe Marra during the course of this work.

This thesis and a number of publications would not have been possible without Dr Rachel Godun and Dr Stephen Webster who run the $^{171}\text{Yb}^+$ ion trap. I would also like to thank Peter Whibberley and Dr Krzysztof Szymaniec for their support and useful consultations during the reference signal performance tests. I would like to acknowledge Dr Barney Walton, who helped me in the lab with the frequency measurements.

ACADEMIC REGISTRY

Research Thesis Submission



Name:	Veronika Tsaturian		
School/PGI:	School of Engineering and Physical Sciences		
Version: (i.e. First, Resubmission, Final)	First	Degree Sought (Award and Subject area)	Doctor of Engineering

Declaration

In accordance with the appropriate regulations I hereby submit my thesis and I declare that:

- 1) the thesis embodies the results of my own work and has been composed by myself
- 2) where appropriate, I have made acknowledgement of the work of others and have made reference to work carried out in collaboration with other persons
- 3) the thesis is the correct version of the thesis for submission and is the same version as any electronic versions submitted*.
- 4) my thesis for the award referred to, deposited in the Heriot-Watt University Library, should be made available for loan or photocopying and be available via the Institutional Repository, subject to such conditions as the Librarian may require
- 5) I understand that as a student of the University I am required to abide by the Regulations of the University and to conform to its discipline.

* Please note that it is the responsibility of the candidate to ensure that the correct version of the thesis is submitted.

Signature of Candidate:		Date:	14 July 2013
-------------------------	--	-------	--------------

Submission

Submitted By (name in capitals):	Prof D. T. REID
Signature of Individual Submitting:	
Date Submitted:	

For Completion in the Student Service Centre (SSC)

Received in the SSC by (name in capitals):			
Method of Submission (Handed in to SSC; posted through internal/external mail):			
E-thesis Submitted (mandatory for final theses)			
Signature:		Date:	

Please note this form should bound into the submitted thesis.

Updated February 2008, November 2008, February 2009, January 2011

Contents

1	Introduction	1
2	Introduction to frequency combs	5
2.1	Time, frequency and clocks	6
2.1.1	Definition of time and frequency	6
2.1.2	Timescales and time keeping	6
2.1.3	Clocks and frequency standards	7
2.2	Historical overview of optical frequency measurement techniques . . .	8
2.2.1	Frequency multiplication using harmonic frequency chains	9
2.2.2	Frequency division techniques	11
2.3	Femtosecond optical frequency combs	13
2.3.1	Basic concepts	14
2.3.1.1	Self-referencing technique	17
2.3.1.2	Femtosecond comb stabilisation	19

2.3.2	Laser sources for comb generation	20
2.4	Optical frequency standards and clocks	22
2.4.1	Optical frequency standards	22
2.4.1.1	Atomic references based on a single trapped ion . . .	23
2.4.1.2	Atomic references based on neutral atoms	25
2.4.1.3	Stable probe laser	26
2.4.1.4	Laser cooling	28
2.4.1.5	Clock transition detection	29
2.4.2	Characterisation of frequency stability	30
2.4.2.1	Amplitude and phase noise	31
2.4.2.2	Allan variance	33
2.4.3	Optical frequency standards performance	35
2.4.4	Frequency comb performance	40
2.5	Summary	42
3	Introduction to the NPL combs	44
3.1	Fibre-laser-based-comb	44
3.2	Low-repetition-rate Ti:Sapphire comb	47
3.2.1	Optical arrangement	48
3.2.2	Frequency counting and comb stabilisation	49
3.2.2.1	Repetition rate	50

3.2.2.2	Offset and beat frequencies	50
3.3	Summary	51
4	Improvements to the Ti:Sapphire low repetition rate comb	53
4.1	Modifications to the spectral broadening scheme	54
4.2	Carrier envelope offset frequency stabilisation	55
4.3	Improvement to the frequency doubling efficiency in non-linear crystals	56
4.3.1	Second harmonic generation in KTP	57
4.3.1.1	Phase-matching	57
4.3.1.2	Non-linear susceptibility and effective nonlinear coefficient	60
4.3.1.3	Walk-off mechanism	61
4.3.1.4	Second harmonic generation bandwidth	62
4.3.1.5	Calculations of second harmonic conversion efficiency	63
4.3.2	Second harmonic generation in periodically poled KTP	65
4.3.2.1	Quasi phase matching and poling period	65
4.3.2.2	Second harmonic generation bandwidth	66
4.3.2.3	Second harmonic conversion efficiency calculations .	68
4.3.3	Comparison of the KTP and PPKTP crystals	68
4.3.4	Signal to noise ratio calculations	69
4.4	Group velocity dispersion assessment	73

4.4.1	Microstructure fibre	73
4.4.2	Non-linear crystal	75
4.5	Dispersion compensation methods used in self-referencing schemes . .	76
4.5.1	Methods based on spectral separation	76
4.5.2	Dispersion compensation with a common-path interferometer .	79
4.6	Wollaston prism-based self referencing setup	80
4.6.1	Wollaston prism principles of operation	80
4.6.2	Relative delay between the two output beams	81
4.6.3	Self-referencing setup description	86
4.7	Experimental characterisation of novel self-referencing scheme	89
4.7.1	Comparison of Wollaston prisms and Michelson interferometer based schemes	90
4.7.1.1	Phase error measurements	92
4.7.1.2	Phase noise measurements	94
4.7.2	Single Wollaston prism compact setup	95
4.8	Summary	96
5	Sources of systematic uncertainty and instability of frequency combs	98
5.1	Microwave frequency reference sources	98
5.1.1	Caesium primary frequency standards	99
5.1.1.1	Principles of operation	99

5.1.1.2	Uncertainty budget	102
5.1.2	Hydrogen maser	104
5.1.3	GPS-disciplined oscillator	106
5.2	Stability and accuracy of the 10-MHz reference signal in the combs laboratory	110
5.2.1	Influence of distribution system on the 10-MHz signal stability	112
5.2.2	Accuracy of the 10-MHz signal delivered to the combs laboratory	116
5.3	Stability and accuracy of maser-referenced synthesisers	119
5.3.1	Stability	120
5.3.2	Temperature sensitivity	122
5.3.2.1	IFR 2023A synthesiser	123
5.3.2.2	HP 8662A synthesiser	125
5.3.3	Accuracy	128
5.4	Conclusions	131
6	Absolute frequency measurement of the 436 nm clock transition in a single $^{171}\text{Yb}^+$ ion	134
6.1	$^{171}\text{Yb}^+$ optical frequency standard	135
6.2	Measurements of the absolute frequency of the E2 clock transition .	137
6.2.1	$^{171}\text{Yb}^+$ ion preparation and detection	137
6.2.2	Frequency measurements and data analysis	139
6.2.3	Frequency correction using Circular T	142

6.2.4	Results and discussion	145
6.3	Conclusions	149
7	Conclusions and summary	151
7.1	Technical Summary	151
7.2	Further Work	154

Chapter 1

Introduction

In the modern world the accurate measurement of time and frequency is vital to the success of many fields of science and technology. In order to compare results obtained at different times and locations, a common basis for frequency measurements is needed. This is provided by frequency standards, which are capable of producing particular frequencies with a given accuracy and form an important component of clocks. The current primary time and frequency standard is based on the ground state hyperfine transition in the ^{133}Cs atom, which occurs at a microwave frequency of approximately 9.2 GHz.

The stability and accuracy of an atomic frequency standard are related to the ratio of the reference transition frequency to its linewidth. Optical frequencies are five orders of magnitude higher than microwave frequencies, while linewidth-limiting processes in the two domains are similar. Frequency standards based on transitions in the optical spectral region therefore have the potential to achieve stability and accuracy much higher than microwave standards. State-of-the-art optical frequency standards based on narrow transitions in cold atoms and ions show good accuracy, reproducibility and frequency stability at the level of a few parts in $10^{15}/\sqrt{\tau}$ [1, 2, 3]. At present, the accuracy of absolute frequency measurements of optical standards is limited to a few parts in 10^{16} by the accuracy of caesium primary frequency standards but

reproducibilities of 10^{-18} could be achieved [4].

The use of optical frequency standards until recently was complicated by the difficulties of measuring high frequencies, because an absolute measurement of frequency must be based on the microwave primary frequency standard and therefore required a complex clockwork to connect optical frequencies to those in the microwave region. Now the femtosecond frequency comb produces an optical spectrum a few hundred terahertz wide consisting of distinct lines with well-defined separation of the order of hundreds of megahertz. This comb of frequencies can be used as a precise frequency ruler for measurements of an arbitrary optical frequency by heterodyning the optical frequency with the nearest comb line. The resulting beat signal is in the radio frequency (RF) spectral region, and so can easily be compared to the primary frequency standard.

There are many examples of the application of optical frequency standards and clocks in fundamental physics, atomic spectroscopy, astronomy and other areas of modern science [5, 6, 7, 8]. In metrology, apart from applications in clocks and maintenance of time scales, frequency standards are vital in establishing standards for a number of other physical quantities. Since frequency is the quantity which can be measured with the highest degree of accuracy, other physical quantities can often be determined with improved precision if they can be traced back to a frequency measurement. For example, the unit of length is derived from the distance that an electromagnetic wave travels in vacuum during a specified period of time [9]. Furthermore, there are many more ordinary applications of accurate clocks such as satellite-based navigation, management of electric power networks and telecommunication networks, which require synchronization of local timing sources with accepted national or international standards.

The quest for more precise time keeping and a potential redefinition of the second [2] is ongoing. A frequency comb is the enabling mechanism, the clockwork for the next generation of clocks – optical clocks. In line with continuous improvements to the

accuracy of optical frequency standards, it is vital to ensure that the contribution of the frequency combs to the inaccuracy of the measured frequency remains negligible. This thesis is dedicated to the frequency combs as an integral part of an optical clock and an ultimate tool for optical frequency metrology.

The history of optical frequency measurement techniques and the principles of operation of femtosecond mode-locked laser-based frequency combs are given in Chapter 2, followed by a discussion of various comb designs and one of the applications of frequency combs – optical clocks.

In Chapter 3 the design of the two NPL frequency combs used for the research presented in this thesis – the low repetition rate Ti:Sapphire comb and the transportable fibre comb – as they were at the beginning of my project is described in detail.

Improvements made to the original design of the low repetition rate Ti:Sapphire laser based comb, mainly focused on the f -to- $2f$ self referencing system, are detailed in Chapter 4. Initially, the theory of second harmonic generation in two types of non linear crystals is given and it is shown that the conversion efficiency is higher for one of these types, which could give better signal to noise ratio in a beat signal generated from the second harmonic. This is then demonstrated experimentally. A novel design of self-referencing scheme is then described and its performance is compared to the performance of a more conventional self-referencing scheme. The new system [10] is based on a common-path interferometer for group velocity dispersion compensation, using the difference in the group velocities of orthogonally polarised light in a Wollaston prism. The main advantage of the common-path interferometer over commonly used interferometers such as Mach-Zehnder or Michelson interferometers, is that all spectral components travel along the same optical path, resulting in common-mode acoustic noise rejection. It is experimentally demonstrated that the use of the Wollaston prism based interferometer provides up to 15 dB lower phase noise compared to a Michelson interferometer. Furthermore, a compact setup based on a single Wollaston prism and a concave mirror is also described, which reduces the size of the

self-referencing system and brings further improvement to the signal to noise ratio (SNR) in the beat signal.

In Chapter 5 one of the sources of systematic uncertainties and instabilities (the microwave reference frequency) affecting the results of frequency measurements performed with the frequency combs is described. Firstly, various sources of microwave frequency signal are described and the limitations to the stability and accuracy of the reference signal provided by these sources are analysed. Next, the degradation of the signal from a hydrogen maser delivered into the combs laboratory is analysed, considering the effects of distribution amplifiers as well as the quality of the signal produced by two types of synthesisers referenced to the maser signal from the last distribution amplifier. Finally, the impact of temperature variations on the accuracy of the frequency signal produced by maser-referenced synthesisers is analysed.

Chapter 6 describes an absolute frequency measurement of the electric quadrupole clock transition at 436 nm in a frequency standard based on a single $^{171}\text{Yb}^+$ trapped ion, performed using the transportable fibre laser-based comb [11]. Initially, a description of the $^{171}\text{Yb}^+$ optical frequency standard is given followed by a description of the arrangement of the experiment. Next, the data processing is detailed including the analysis of the measured frequency of the clock transition and the calibration of the reference signal used during the measurements. Finally, the frequency of the clock transition is calculated including an estimate of its uncertainty, and this result is compared to that obtained for the same transition measured by another group [12] showing good agreement within the uncertainty of the measurements.

Results of the work described in this thesis and proposed future work are summarised in Chapter 7. Some of these improvements have been already implemented at NPL during the time passed since the work described in this thesis was finished, and have demonstrated that the comb's contribution to the total uncertainty of the measured frequency of an optical frequency standard is negligible compared to the uncertainty due to the systematic frequency shifts of the transition frequency itself.

Chapter 2

Introduction to frequency combs

This chapter gives an overview of the background material referred to in subsequent chapters of this thesis. Firstly, the definition of the SI unit of time, timescales and timekeeping, and the concept of a frequency standard as part of an atomic clock are discussed. Next, a historical overview of optical frequency measurement techniques is presented and a modern method employing femtosecond frequency combs is described. The principles of operation and basic design concepts of a femtosecond combs are presented, together with an overview of various laser sources used for comb generation. Finally, optical clocks as one of the applications of frequency combs are reviewed. The concept of an atomic frequency standard, the methods of characterising clock performance and various atomic references and examples of the best performance achieved are described. Lastly, the comparison of frequency combs is presented, showing that the performance of the optical clock is not limited by the frequency comb performance.

2.1 Time, frequency and clocks

2.1.1 Definition of time and frequency

The unit of time interval, the second, is one of the base units of the International System of Units (SI). In 1967 the 13th General Conference for Weights and Measures (CGPM) defined the second as follows: “The second is the duration of 9 192 631 770 periods of the radiation corresponding to the transition between the two hyperfine levels of the ground state of the caesium 133 atom” [13]. Based on this definition the unit of frequency, the hertz, representing the number of cycles in one second is defined.

2.1.2 Timescales and time keeping

The oldest function of clocks is timekeeping. One of the applications of precise timekeeping is celestial navigation, which requires accurate knowledge of the Earth’s rotation angle or mean solar time. One of the time scales currently used is Universal Time (UT1) – an astronomical time scale based on the mean solar day, which is defined to consist of 86400 seconds [14]. However, due to irregularities in the Earth’s rotation, UT1 is not uniform.

The present definition of the SI second allows an atomic time scale to be formed – International Atomic Time (TAI). The International Bureau of Weights and Measures (BIPM) calculate International Atomic Time (TAI) retrospectively from data provided by about 69 national timing laboratories around the world. Each laboratory reports the time differences between each of its clocks and its local timescale, designated UTC(lab). To make it possible to compare data from different laboratories, each laboratory also provides the time differences between UTC(lab) and GPS time, measured using an algorithm defined by the BIPM and at times specified in the BIPM tracking schedules. BIPM calculates the weighted average of these data to derive the

free atomic timescale (EAL). The duration of the scale interval of EAL calculated in this way is compared to the data from caesium primary frequency standards and if necessary corrected to bring it as close as possible to the SI second realised by these primary standards. The resulting steered timescale is TAI.

Unfortunately the length of the day defined as 86400 TAI seconds is shorter than astronomical day defined using UT1. Given that astronomical navigation as well as everyday life is regulated by the rotation of the Earth, another atomic time scale called Universal Coordinated Time (UTC) was introduced in 1972. The scale interval of UTC is the same as that of TAI and the difference between UTC and astronomical time is removed by the occasional insertion of leap seconds into UTC. These leap seconds are inserted in such a way that the absolute magnitude of the difference between UTC and UT1 is always less than 0.9 s.

The deviation of local time scales UTC(lab) from UTC is calculated by BIPM from the data supplied by each laboratory and distributed in a monthly bulletin called “Circular T”. The data in “Circular T” can be used for subsequent corrections of the local time scale used in real time during frequency measurements.

2.1.3 Clocks and frequency standards

Every clock consists of two principal components: an oscillator which produces the “ticks” of the clock and a clockwork used to generate a usable signal for reading and displaying this readout. In an atomic clock the clock “ticks” are provided by a frequency standard, comprised of an oscillator providing a periodic signal of a given frequency and an atomic resonance which is used to control the frequency of the oscillator. In an optical clock, a frequency comb based on a femtosecond mode-locked laser is used as the clockwork to facilitate translation of the frequency signal provided by a precision optical oscillator into the microwave frequency domain.

Frequency standards can be divided into two groups: active and passive [15]. Active

frequency standards are based on a collection of excited oscillators producing a signal at a frequency specified by the properties of the atoms. Usually a fraction of the emitted signal is used to stimulate the emission of other excited atoms leading to a highly coherent output signal, for example in gas lasers or hydrogen masers (discussed in Section 5.1.2).

In contrast to active standards, passive standards are based on devices or materials sensitive to particular frequencies. Such references can be based on macroscopic devices such as resonators or microscopic systems such as atoms. The interrogation of an atomic reference by an oscillator produces an absorption line with a minimum at the resonance frequency ν_0 . A servo signal generated from the absorption signal is fed back to the oscillator to tune its frequency as close as possible to the frequency ν_0 of the reference. When the servo loop is closed, the oscillator frequency is locked to the reference frequency ν_0 and the system can be used as a frequency standard.

Amongst all frequency standards, primary frequency standards based on Cs atoms have a special place because they are used to realise the SI second. There are several configurations of Cs atomic clocks, but the most accurate primary frequency standards are realised using laser cooled atoms in a fountain configuration as discussed in detail in Section 5.1.1. The frequency of other frequency standards must be traceable back to a primary frequency standard.

2.2 Historical overview of optical frequency measurement techniques

High accuracy frequency measurement is straightforward at low (RF or microwave) frequencies, where counters and synthesisers are readily available. The heterodyne technique, which produces an easily measurable frequency difference between known and unknown frequencies, can further extend the limit of measurable frequency. This

technique allows microwave frequencies up to few hundred gigahertz to be measured. The problem of measuring optical frequencies lies in the availability of accurately known frequencies to beat an unknown frequency with. The first aspect of this problem is that only a few known frequencies exist in the optical region, and consequently the nearest one could be a few terahertz away from the unknown frequency to be determined. The second aspect is the difficulty of establishing the known frequency, which requires a complicated “clockwork” to connect optical to microwave frequencies, since as discussed in the previous section an absolute measurement of frequency must be based on the SI second.

Different techniques for optical frequency measurements such as frequency chains and various frequency division methods were developed over the last 45 years [16, 17, 18, 19, 20]. However, after the invention of femtosecond frequency combs, which provide the ultimate solution to the problem of measuring an arbitrary optical frequency and which were recognised by the Nobel Prize in 2005 [21, 22], all other methods of optical frequency measurements became history. Sections 2.2.1 and 2.2.2 present brief descriptions of these historical techniques.

2.2.1 Frequency multiplication using harmonic frequency chains

Optical frequencies can be measured with the aid of frequency multiplication chains [23]. The idea of such a chain is to start from a low frequency and to generate higher harmonics of this frequency using different non-linear devices. A harmonic of the precisely known low frequency is generated and used to determine an unknown higher frequency by measuring their beat frequency. Afterwards a harmonic of this higher frequency can be used for measurements at even higher frequency and so on until the required optical frequency is determined.

The first measurement of laser frequency (rather than of wavelength) was done in

1967 when the frequencies of single mode emission of the NCH laser at 890 GHz and 964 GHz ($337\ \mu\text{m}$ and $311\ \mu\text{m}$) were measured to within a few parts in 10^7 by mixing the laser frequencies with high order harmonics of a microwave signal in a silicon diode [24]. In 1972 the frequency measurements were extended to 88 THz ($3.39\ \mu\text{m}$) when the frequency of a CH_4 -stabilised He-Ne laser was measured using harmonic mixing [25]. In 1973 the same frequency was measured using one of the first harmonic frequency chains connecting the Cs primary standard to the CH_4 -stabilised He-Ne laser [26] with an uncertainty of 6 parts in 10^{10} compared to 5 parts in 10^7 reported before [25]. In 1979 the first frequency measurement of visible radiation (520 THz) was reported [27]. The accuracy of frequency measurements continued to improve during the following years. This can be illustrated by the improvement of the HeNe/ CH_4 laser frequency measurement uncertainty to 8.3×10^{-13} reported in 1993 [28]. Another example is the iodine-stabilised He-Ne laser (473 THz) frequency measurement precision. In 1983 the frequency was measured with an uncertainty of 1.6 parts in 10^{10} [29], while ten years later, in 1993, ten times better uncertainty was reported [30].

Frequency measurements can be based either on a primary Cs standard or on a secondary standard, which is linked to a Cs clock in separate measurements. The secondary standards themselves contribute to the uncertainty of the measured frequency value. In order to avoid additional uncertainties, phase-coherent frequency measurements should link the unknown frequency to the primary Cs standard. Absolute phase-coherent frequency measurements were first performed in the near infrared region [31]. Frequency measurements in the visible region were based on secondary standards until 1996, when the first fully phase-coherent frequency chain connecting the Cs primary standard of time and frequency to a Ca optical frequency standard (456 THz) was reported [32].

The development of frequency chains made accurate frequency metrology possible. This resulted in significantly improved uncertainty for the value of the speed of light in a vacuum [33, 25], leading to the redefinition of the metre in 1983 [9]. Although

significant progress in frequency metrology was achieved, bridging large frequency gaps remained a very demanding task. The conventional method of optical frequency synthesis from the microwave is a complicated procedure involving a variety of different oscillators needed after each step, so a harmonic frequency chain covering a large frequency span becomes a highly complex, large-scale and expensive system, which involves significant efforts to build and operate. Furthermore, each frequency chain targets only one specific optical frequency.

2.2.2 Frequency division techniques

The alternative approach to optical frequency measurements is frequency division. The idea of this method is to divide a large frequency gap into smaller measurable frequency intervals with a known relationship to the original, so that by measuring the small frequency differences the original frequency interval can be established.

One of the techniques providing optical to radio frequency division is frequency interval bisection [34]. One bisection stage of such a system generates the arithmetic average of two laser frequencies f_1 and f_2 by phase locking a second harmonic of a third laser at frequency f_3 to the sum frequency of f_1 and f_2 . Cascading of n stages will provide frequency division by 2^n .

The use of optical parametric oscillators (OPOs) for frequency division was proposed in [35]. This scheme converts an input signal into two coherent subharmonic outputs with tunable frequencies and linewidths limited by the input pump linewidth. The OPO's input pump or output frequencies can be precisely determined by phase locking the difference frequency between the outputs to a microwave standard. The proposed divider can operate in parallel or in series to provide multistep frequency division. However, the difficulty of finding nonlinear crystals suitable for OPO operation in different spectral regions prevented this system from practical realisation [19].

A method of optical frequency measurement in the near infrared based on sum and

difference frequency generation using non-linear optics was proposed in [36]. The sum of two frequencies can be compared with a visible frequency standard, while the difference frequency can be compared to a standard in the far-infrared.

Four-wave mixing in laser diodes can be used for difference frequency generation [37]. In this configuration two external cavity laser diodes (ECLD) with frequencies f_1 and f_2 separated by 1 – 2 THz are optically injected into a third ECLD. When the frequency of a third ECLD (f_3) is tuned near to the centre of the interval between f_1 and f_2 , f_3 locks to the four-wave mixing product $f_1 + f_2 - f_3$, leading to the interval bisection condition $f_3 = (f_1 + f_2)/2$. Phase matching in the mixing diode limits the bandwidth to a few THz.

Another technique for difference frequency synthesis is to generate a comb of frequencies by placing an electro-optic modulator (EOM) inside a Fabry-Perot (FP) cavity which is resonant with both the carrier frequency and all generated sidebands [38]. When the modulation frequency is equal to an integer multiple of the free spectral range of the FP cavity, the sidebands generated from the carrier pass back through the EOM and generate secondary sidebands, which also generate further sidebands. This optical frequency comb generator (OFCG) produces a wide comb of modes spaced exactly by the modulation frequency.

The maximum detectable beat frequency between the comb modes and the source of unknown frequency is theoretically restricted by the power of the sidebands. The power in a particular high order sideband increases as either the finesse of the FP cavity or the modulation index increases. This type of OFCG bridges frequency gaps on the order of 10 THz. However, even with higher modulation index and finesse of the FP cavity the comb width is still limited to about 5% of the carrier frequency. Further increase of the span is limited by chromatic dispersion of the crystal [39], mirror reflection bandwidth and incident microwave power limitation (to prevent damage to the EOM) [40]. Additional bandwidth increase can be achieved using self-phase modulation in an optical fibre; in this way increase of the comb width

up to 30 THz has been reported [40].

2.3 Femtosecond optical frequency combs

The other method of producing a frequency comb is to use a mode-locked laser. Mode-locking is the regime in which a laser emits a number of longitudinal modes with synchronised phases. If the laser modes have a fixed phase relationship, such a laser produces a periodic train of short pulses and the spectrum of this emission corresponds to a comb of distinct equally spaced lines. In order to achieve phase difference stabilisation a periodic modulation of either the amplitude or phase of the field in the resonator is used [41]. There are two types of mode-locking: active and passive. In the first case an amplitude modulator with the modulation frequency tuned to the frequency difference between the adjacent modes of the laser resonator is placed inside the laser cavity. Passive mode-locking is realised via a saturable absorber, an element whose optical absorption is constant at low intensities, but saturates and decreases to lower values as the incident light intensity increases [42]. In this case a saturable absorber inside a laser cavity enables self-amplitude modulation of the laser pulse. To generate femtosecond pulses passive mode-locked lasers are used.

The first use of a mode-locked laser for optical frequency metrology was reported in 1978 [43], when a synchronously pumped picosecond mode-locked dye laser was used for Doppler-free two-photon spectroscopy. However, although the concept of using a mode-locked laser as an optical frequency comb generator was demonstrated, because of the bandwidth limitation it did not provide a practical tool for optical frequency measurements. The spectral bandwidth of such a comb is approximately the inverse of the Fourier-limited pulse duration, which is of the order of terahertz for a picosecond laser. The discovery of Kerr-lens mode-locked (KLM) Ti:sapphire lasers capable of producing femtosecond pulses [44, 45] opened a new chapter in optical frequency metrology. Since the first frequency measurements using a KLM

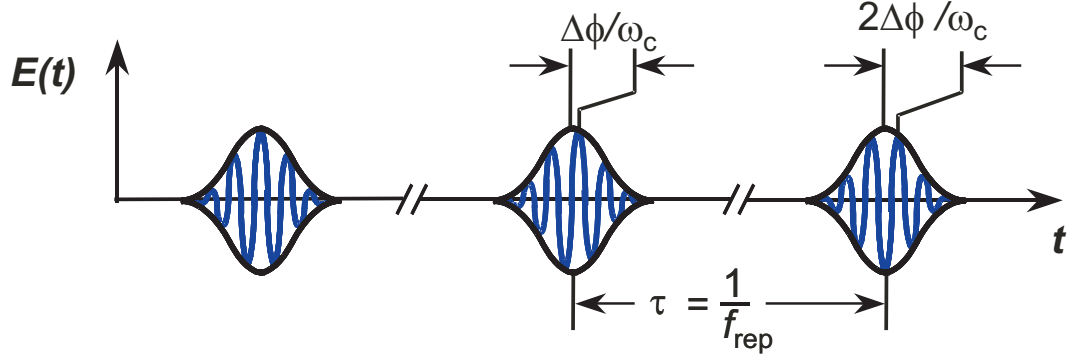


Figure 2.1: A pulse train representation in the time domain.

Ti:sapphire laser-based optical frequency comb were reported in 1999 [46, 47] the design of frequency combs has been significantly improved and they have become a standard tool in frequency metrology. Section 2.3.1 gives the basic concepts of optical frequency combs, while Section 2.3.2 describes the types of frequency comb technology in use in different laboratories worldwide.

2.3.1 Basic concepts

A mode-locked laser produces a train of short pulses each separated by a time interval

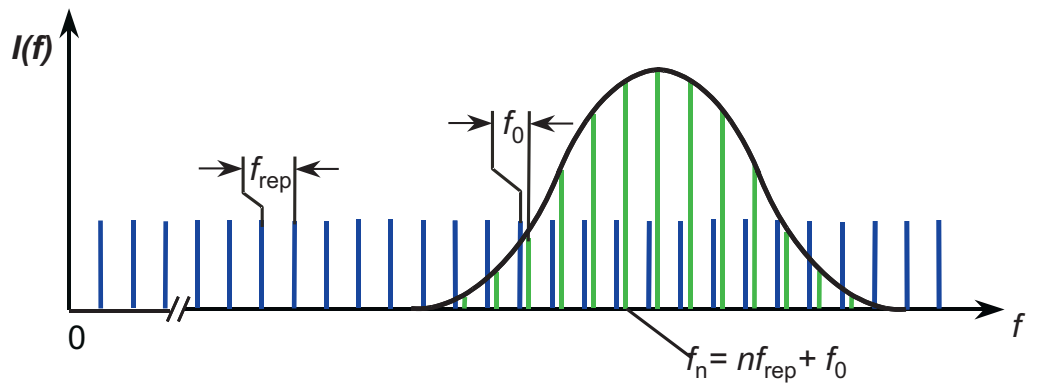


Figure 2.2: A pulse train representation in the frequency domain.

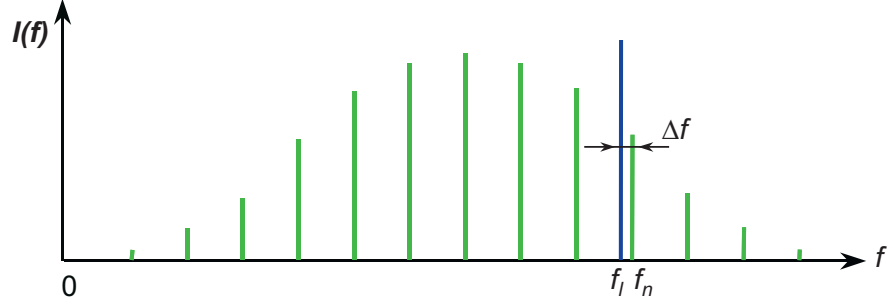


Figure 2.3: Measurements of an optical frequency f_l using the frequency comb produced by a mode-locked laser.

$$\tau = \frac{l_c}{v_g}, \quad (2.1)$$

where l_c is the roundtrip length of the laser cavity and v_g is the group velocity (Fig. 2.1). A pulse is emitted every time a pulse circulating inside the cavity reaches the output coupler. Due to dispersion inside the cavity the group and phase velocities are different. This difference leads to a phase shift $\Delta\phi$ between the carrier wave and the peak of the envelope for each round trip given by

$$\Delta\phi = \left(\frac{1}{v_g} - \frac{1}{v_p} \right) l_c \omega_c \text{mod}(2\pi), \quad (2.2)$$

where v_p is the intracavity phase velocity and ω_c is the carrier frequency [19]. This pulse-to-pulse shift is shown in Fig. 2.1. The frequency spectrum of the pulse train with pulse separation τ consists of a comb of frequencies separated by $f_{\text{rep}} = 1/\tau$ (Fig. 2.2). The frequency of each comb line is given by

$$f_n = f_0 + n f_{\text{rep}}, \quad (2.3)$$

where n is an integer comb line number and f_0 is the carrier envelope offset frequency given by

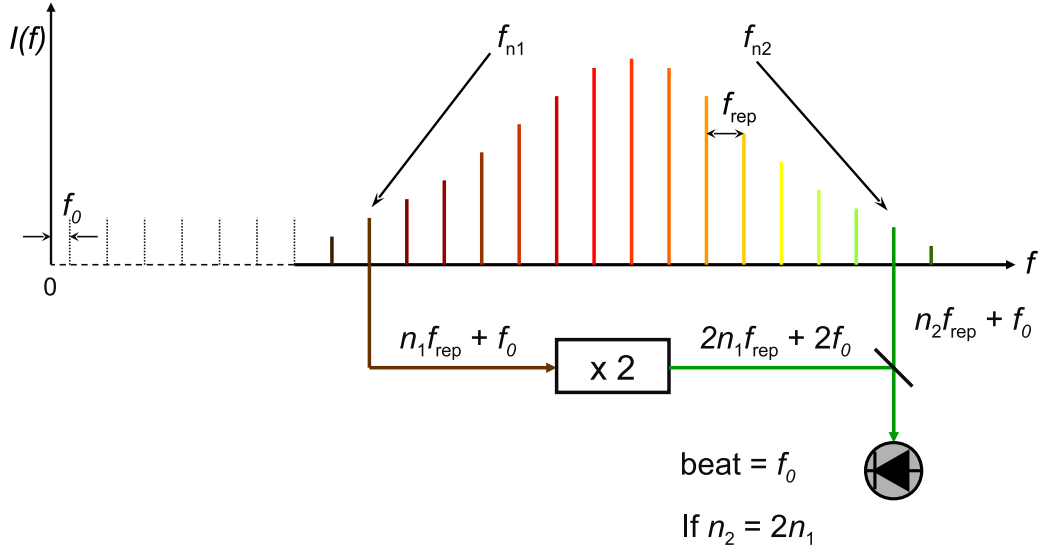


Figure 2.4: Self-referencing technique for offset frequency measurement.

$$f_0 = \frac{\Delta\phi}{2\pi} f_{\text{rep}}, \quad (2.4)$$

as shown in Fig. 2.2.

Figure 2.3 shows how a frequency comb can be used to measure an unknown optical frequency f_l . The heterodyne beat Δf between the laser frequency f_l and the frequency of the nearest comb line f_n can easily be measured with standard RF equipment. Consequently, absolute frequency measurements can be made if the repetition rate and offset frequencies of the comb as well as the mode number n are known.

The repetition frequency can be measured straightforwardly by detecting the pulse train with a fast photodiode [48]. In the case of direct counting of the detected beat the accuracy of the measurements would be limited by the resolution of the frequency counter used. To avoid this limitation, the signal can be down converted by frequency mixing and the signal at lower frequency can be counted.

2.3.1.1 Self-referencing technique

The easiest way to determine the offset frequency f_0 is the f -to- $2f$ self-referencing technique [49], which is based on the measurement of a heterodyne beat between a mode from the high frequency side of the comb and a frequency doubled mode from the low-frequency side of the comb (Fig. 2.4). For this measurement the frequency comb should span at least one octave, i.e. the highest frequencies should be larger than the lowest by a factor of 2. In this case the difference between a low frequency f_n doubled in a non-linear crystal and a high frequency f_{2n} is given by

$$2f_n - f_{2n} = 2(nf_{\text{rep}} + f_0) - (2nf_{\text{rep}} + f_0) = f_0, \quad (2.5)$$

which is exactly the offset frequency. Note that self-referencing is the simplest, but not the only method of offset frequency measurements [48]. It can even be achieved with a comb spacing less than an octave, but this requires extra steps of non-linear conversion [18]. A summary of these options can be found in [50].

One of the methods of spectral broadening used to obtain an octave-spanning spectrum is based on self-phase modulation, the non-linear effect generating new frequencies and as a result broadening the pulse spectrum. Since the amount of broadening depends on peak power, mode area and interaction length, an optical fibre is often used as a non-linear medium providing power confinement in a fibre core. The amount of broadening in ordinary fibre is limited by group velocity dispersion which leads to temporal pulse spreading and peak intensity reduction. Although an octave-spanning spectrum in standard fibre has been demonstrated, it requires high pulse energy [51]. The invention of single mode photonic crystal fibre (PCF) [52], which can have zero group velocity dispersion within the Ti:sapphire emission spectrum [53] eliminated this problem, allowing broadband continuum generation with only nanojoule pulse energies [48].

Photonic crystal fibre used for spectral broadening has a fused silica core surrounded

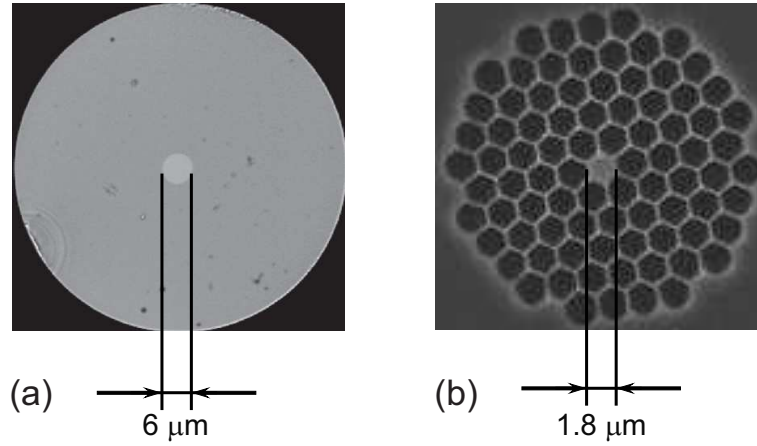


Figure 2.5: Standard single mode fibre (a) and silica-core photonic crystal fibre (b) [picture courtesy of OFS].

by the comb-like array of air holes, as shown in Fig. 2.5. Similarly to conventional optical fibre, the guiding mechanism of the silica-core PCF is based on the index of refraction contrast between the core and partially air-filled cladding. However, the index contrast in PCF is much higher than in conventional single mode fibre, allowing fibre to be designed with smaller core size. Since the non-linear coefficient is inversely proportional to the effective area, the non-linear effects are enhanced by both the higher energy density inside the fibre core and the higher non-linear coefficient. Furthermore, the chromatic dispersion can also be adjusted by changing the number and size of the air holes to further increase non-linear induced spectral broadening. Another result of the high index contrast is that PCF is single mode for any wavelength [54], hence at the output of the fibre only fundamental mode is present, which gives an advantage of the efficient second harmonic generation and strong interference necessary for the operation of the f -to- $2f$ interferometer. Although octave-spanning Ti:sapphire lasers produced directly by optimising cavity alignment and dispersion have been reported [55, 56, 57], spectral broadening in microstructure fibre remains the most popular technique.

2.3.1.2 Femtosecond comb stabilisation

In order to determine an absolute optical frequency the beat frequency (Δf) between the unknown frequency and the nearest comb line, the offset frequency (f_0) and the comb line separation (f_{rep}) could be simply measured simultaneously (Fig. 2.3). However, it is usually preferable to actively stabilise them in a feedback loop. The intermode separation given by

$$f_{\text{rep}} = \frac{1}{\tau} = \frac{v_g}{l_c} \quad (2.6)$$

is determined by the laser cavity length, which drifts over long timescales due to thermal effects and varies on short timescales due to acoustic noise. It is possible to compensate both of these effects by adjusting the cavity length using a mirror mounted on a piezo-electric actuator controlled by a phase-locked loop that compares an external clock signal to f_{rep} or one of its harmonics.

There are two different techniques for offset frequency control. One of these can be implemented in lasers which use prisms for dispersion compensation. Since the spectrum is spatially dispersed on the end mirror of the laser cavity, a small rotation (swivel) of the mirror produces a linear phase delay with frequency, which is equivalent to a group velocity delay, and hence adjusts the offset frequency [58]. Another method of locking f_0 , which can be implemented in any laser cavity, relies on the pulse-to-pulse phase shift with a change of the pump power [59]. Electro-optic modulators [60, 61] or acousto-optic modulators (AOMs) [55, 56] can be used for pump power modulation in solid state lasers. In fibre combs the pump power can be modulated via the pump laser current.

2.3.2 Laser sources for comb generation

The first measurement of an optical frequency with a femtosecond laser based frequency comb was made with a KLM Ti:sapphire laser based comb with 75 MHz repetition rate [46, 47]. Since that time Ti:sapphire-based combs have become a widely used tool for optical frequency metrology. There are two types of Ti:sapphire-based combs used at present: ones where the octave-spanning spectrum required for the f -to- $2f$ self-referencing is obtained with additional spectral broadening in microstructure fibre [53] and combs which are capable of producing an octave-spanning spectrum directly from the laser [62]. The repetition rates of Ti:sapphire-based combs vary from a few tens of megahertz [49] to 10 GHz [63] depending on the laser design. For frequency metrology Ti:Sapphire frequency combs have several advantages such as high repetition rate (which provides increased power per mode and simpler access to comb lines), the possibility to generate an octave-spanning spectrum directly from the laser and low-noise performance. However they also have several drawbacks. Ti:sapphire based systems need a green pump laser, typically a frequency doubled Nd:YVO₄ solid-state laser, which is an expensive large footprint device, requiring water cooling for its operation. The bulk-optic design of these lasers also means that they require careful alignment. These limitations have inspired a search for alternative potentially transportable and less expensive laser systems. One of the alternatives is to use erbium or ytterbium fibre doped lasers, while another is to use diode-pumped solid-state laser based systems.

An Er-doped fibre laser based comb was demonstrated for the first time in 2004 [64]. These lasers are directly pumped with laser diodes at 980 nm or 1490 nm, which makes them compact, robust and power efficient. The centre wavelength of 1550 nm gives the advantage of using robust and low-cost integrated fibre optic components designed for telecommunications systems, which means that these lasers require less alignment than bulk solid-state laser systems. Fibre-based combs are less expensive and more robust than Ti:sapphire based combs and allow for turnkey operation. In

addition, they are capable of covering both the near infrared region as well as the visible region by using non-linear frequency conversion. Furthermore, active stabilization techniques have reduced the close-to-carrier frequency noise to levels similar to those of Ti:sapphire lasers [65].

Yb-fibre laser based frequency combs have superior power scalability which is critical for multi-GHz frequency combs involved in nonlinear optical applications such as wavelength conversion into the visible wavelength range. For example, an Yb-based frequency comb with 80 W average power has been demonstrated [66], but at low repetition rate (154 MHz). Even though a fundamentally mode-locked femtosecond Yb-fibre laser with 3 GHz repetition rate has been demonstrated [67], GHz repetition rates are not easily accessible in fibre lasers. Furthermore, only two fibre laser-based fully stabilized frequency combs with 1 GHz repetition rates have been reported up to date: one Yb laser-based comb [68], and one Er laser based comb [69].

There are several drawbacks of fibre frequency combs such as the need for external amplification, higher frequency noise and broader optical comb lines associated with the lower cavity quality factor (Q) and amplified spontaneous emission in the laser and external fibre amplifier. Although techniques to reduce the broadband phase noise of Yb-based combs have been reported [70], noise suppression in fibre lasers remains more challenging than in solid state lasers.

Another alternative to Ti:sapphire based combs is diode-pumped solid-state laser based systems. The first carrier-envelope offset frequency measurement for this type of comb was performed in 2001 [71]; the comb was based on a Cr:LiSAF laser operating at 93 MHz repetition rate. In 2004 a self-referenced frequency comb based on a Cr:forsterite laser with a repetition rate of 433 MHz was reported [72]. However, the disadvantages of colquirite laser crystals, such as relatively low thermal conductivity and non-linearity needed for KLM, switched attention to various Yb-doped hosts.

As femtosecond laser sources, Yb-doped crystals have several advantages: the possibility of direct pumping by common laser diodes, the high efficiency and low power

requirements which make them suitable for transportable combs and the fact that reliable femtosecond operation is easily achieved by passive mode locking via KLM or a semiconductor saturable absorber mirror. In addition, low intrinsic noise and higher cavity Q , compared to fibre lasers, result in lower phase noise on the frequency comb. Although a large number of femtosecond laser sources have been demonstrated, only two fully stabilised combs have been reported to date: an Yb:KYW femtosecond laser based comb with a repetition rate of 160 MHz and spectral coverage 650 – 1450 nm in 2008 [73] and a comb based on an Er:Yb:glass laser operating in the 1.5 μm spectral region at a 75 MHz repetition rate in 2011 [74]. The carrier envelope offset frequency has been detected for an Yb:KGW laser (central wavelength 1.04 μm) with a repetition rate of 1 GHz [75]; however locking has not yet been demonstrated.

2.4 Optical frequency standards and clocks

In an optical clock, a frequency comb is used to generate a countable frequency from an optical frequency standard consisting of an atomic reference and a narrow linewidth probe laser. This section describes the basic principles of optical frequency standards, measures used to characterise their performance and gives an overview of state of the art performance of optical frequency standards together with the performance of the frequency combs.

2.4.1 Optical frequency standards

Figure 2.6 shows a schematic of an optical frequency standard consisting of an atomic reference providing a narrow optical transition at frequency ν_0 and a narrow linewidth probe laser emitting a frequency ν which can be adjusted to the frequency ν_0 using a servo control loop.

The main requirement for the atomic reference is the presence of both a strong allowed

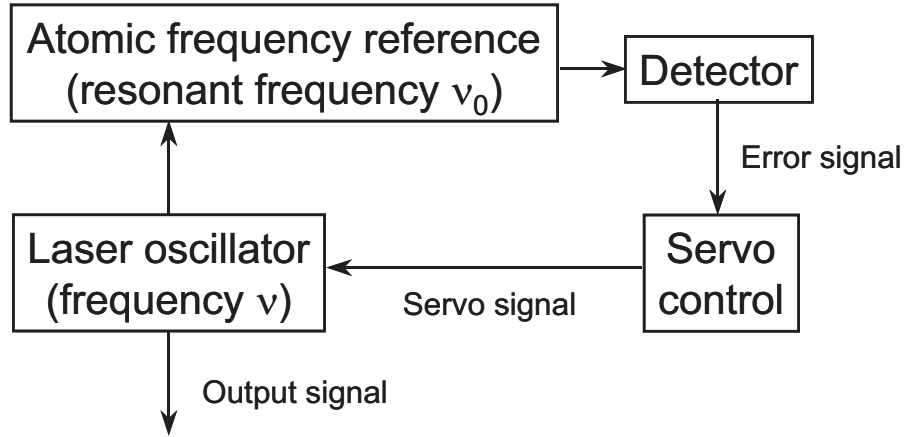


Figure 2.6: Schematic diagram of a passive optical frequency standard.

transition suitable for laser cooling and a weak forbidden clock transition, as shown in Fig. 2.7.

Natural linewidths for optical transitions range from tens of megahertz for strongly allowed transitions to a few hertz or less for weak forbidden absorptions. There are two different types of reference transitions: transitions in a single laser-cooled trapped ion and transitions in cold neutral atoms.

2.4.1.1 Atomic references based on a single trapped ion

A charged particle such as an ion can be confined to a region of space using the interaction of the ion's charge with applied electric and magnetic fields. There are two main techniques used to implement confinement: Penning and Paul traps. In the Penning trap, a combination of static magnetic and electric fields confines the ion; however the applied magnetic field strongly perturbs its energy levels. This effect makes the use of Penning traps for frequency standards impractical.

On the other hand, a trapping field in the Paul trap is purely electrical, close to an ideal quadrupole potential [76] causing only small perturbations to trapped ions when they are confined in the centre. The Paul trap uses time-varying voltages between

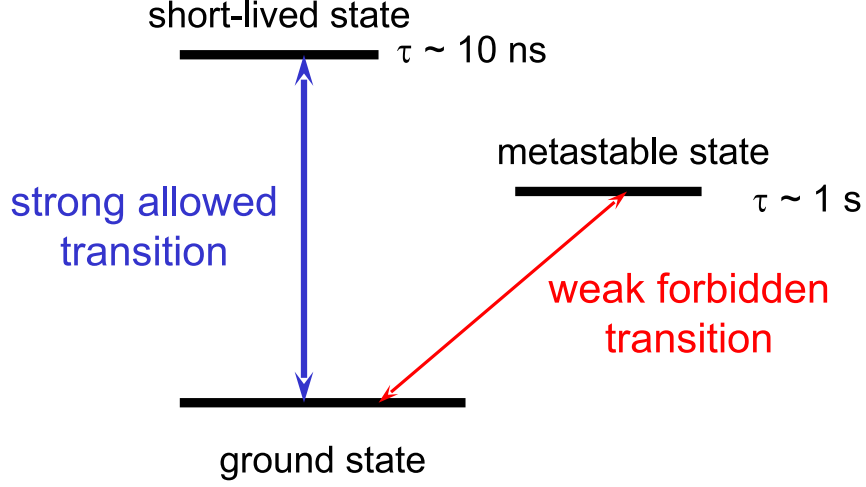


Figure 2.7: Schematic diagram of the cooling (strongly allowed) and clock (weak forbidden) transitions in an atomic frequency reference.

electrodes to create a dynamic pseudopotential well in all three directions. Although at any given time the force acting on the ion provides confinement only in two directions, the time averaged force is not zero due to the trapping field inhomogeneity. This force averaged over a period of oscillation is directed towards the regions of weak electric field; thus the appropriate choice of the field amplitude and frequency provides a time-averaged force directed towards the trap centre as required for confinement.

For a single laser-cooled ion in a Paul trap, such as used for frequency standards, a precise quadrupole field distribution over the entire trapping region is not required [77]. Furthermore, easy optical access for laser beams is desirable. Therefore, simpler variations of the conventional Paul trap providing improved optical access, at the price of achieving a quadrupole field distribution only over a central region, are used for trapped ion optical frequency standards. These include Paul-Straubel (ring) traps [77, 78] consisting of a ring with supporting leads and the endcaps reduced to a pair of distant compensation plates, a linear trap [79] where an ion is confined on axis by four rod-electrodes and a pair of endcaps, and an endcap trap composed of only two pairs of electrodes as endcaps such as the one used for trapping Yb^+ ions at NPL

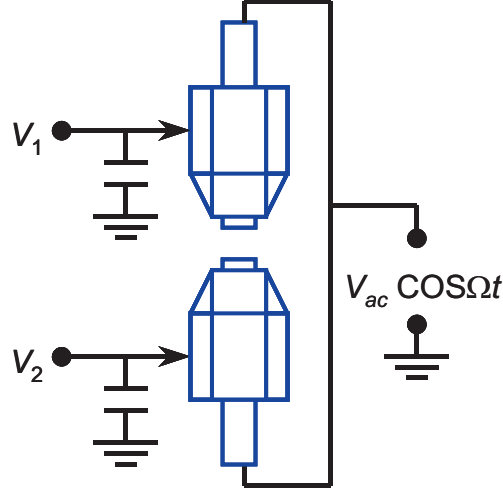


Figure 2.8: Schematic diagram of an endcap trap. The typical parameters are an RF frequency $\Omega/2\pi$ of several tens of MHz and an amplitude V_{ac} of several hundred volts; the DC voltages V_1 and V_2 are a few volts while the spacing between the inner endcap electrodes is around 0.5 mm [1].

(Fig. 2.8).

2.4.1.2 Atomic references based on neutral atoms

An advantage of optical frequency standards based on N atoms over single ion based standards is the potential improvement of stability by a factor of \sqrt{N} . Laser cooling the atoms, for example in a magneto-optical trap (MOT), substantially reduces residual first-order and second-order Doppler shifts [1]. However, the trapping methods for neutral atoms perturb the atomic energy levels, which is undesirable for use in a frequency standard. To avoid the broadening and shifts associated with the trap, neutral atoms are released from the trap before the clock transition is probed. The atoms fall from the trap under the influence of gravity and the atom cloud expands due to the thermal velocities of the atoms. The resulting atomic motion leads to serious limitations in accuracy and stability that are associated with velocity dependent frequency shifts [80]. Two of the more undesirable effects are the limited observation

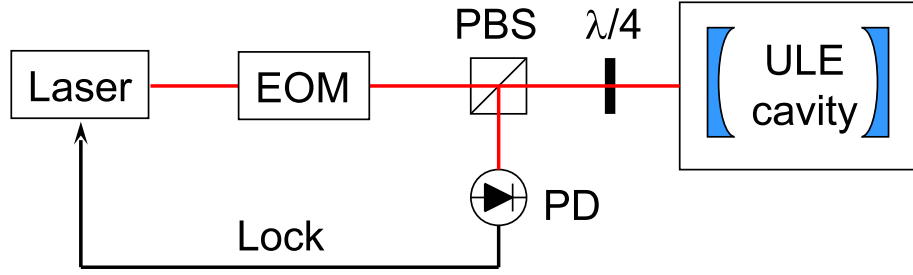


Figure 2.9: Schematic diagram of the optics required for the Pound-Drever-Hall locking technique. EOM - electro-optic phase modulator; PBS - polarizing beam-splitter; ULE cavity - ultra-low expansion cavity; PD - photodetector.

time, and the incomplete cancellation of the first order Doppler shift.

The solution to these problems is to confine atoms in an optical lattice trap as suggested by Katori in 2002 [81]. This arrangement offers the prospect of excellent stability due to the large atom number, and the tight confinement of the lattice allows for effectively Doppler-free interrogation and long interrogation times [3]. In an optical lattice clock the atomic energy level perturbations caused by the light fields used to create the optical lattice are eliminated by tuning the lattice laser to a so-called ‘magic wavelength’ where the ground and excited states of the clock transition are shifted by precisely the same amount [81, 4]. The first time clock spectroscopy of atoms held in an optical lattice at the zero-shift wavelength was demonstrated was in 2003 for ^{87}Sr atoms [82], and since then optical lattice clocks based on various neutral atoms have been investigated in a number of laboratories.

2.4.1.3 Stable probe laser

The linewidth of the laser used to probe the clock transition needs to be comparable with the natural linewidth of the optical transition. Since typical clock transition linewidths are a few hertz or less, to reduce the laser linewidth to this level the Pound-Drever-Hall technique illustrated in Fig. 2.9 is used [83].

This technique is based on locking the probe laser to a high finesse ultra-stable optical cavity. The laser light with carrier frequency f_{car} is phase modulated at frequency f_{m} , providing modulation sidebands used for subsequent heterodyne detection. The frequency f_{m} is chosen in such a way that the modulation sidebands are spectrally outside the cavity passband, and hence reflected from the cavity input mirror. The reflected light is directed to the fast photodetector. The carrier component of the reflected light consists of the beam reflected from the input mirror and the beam leaking back from the cavity through the input mirror. When the carrier frequency f_{car} is close to the cavity resonance frequency f_{res} the phase shift between these beams is strongly frequency dependent. The phase sensitive detection of the reflected light relative to the modulation frequency f_{m} gives the error signal used to lock the laser. This error signal is an antisymmetric function of frequency, which close to resonance is proportional to the frequency offset from the resonance frequency $f_{\text{res}} - f_{\text{car}}$, hence it contains information about how far the laser frequency is off resonance as well as which side of the resonance the laser frequency is.

A high finesse ultra-stable cavity used for clock laser locking consists of two concave mirrors optically contacted onto each end of an ultra-low expansion (ULE) glass spacer. Typical cavity lengths are about 10 cm and typical cavity resonance linewidths are 5 – 10 kHz. As the cavity resonance frequency does not match the frequency of the reference transition, an acousto-optic modulator (AOM) is used to shift it into resonance.

Given that the resonance frequency depends on the cavity length, the cavity must be isolated from environmental perturbations. To achieve this the cavity is mounted on a vibration isolation platform and thermally stabilised to ensure operation at a temperature where the linear coefficient of thermal expansion of the ULE spacer is close to zero. Furthermore, a box providing isolation from acoustic noise is usually built around the laser.

Even with the vibration isolation in place length fluctuations of the ULE cavity can

still occur due to seismic and acoustic vibrations. There are a number of cavity geometries designed to reduce vibration sensitivity; the one used for the NPL $^{171}\text{Yb}^+$ ion frequency standard was reported in [84].

2.4.1.4 Laser cooling

The observation of narrow optical transitions requires laser cooling [85] to remove the Doppler broadening of the clock natural linewidth. The basic principle of laser cooling is that the average energy of the radiation absorbed by the particle is smaller than the energy lost by the particle during the subsequent emission. To illustrate this principle, consider a two-level atom propagating in a vacuum with a known speed. If the stationary atom is illuminated by a laser with photon energy equal to the energy between the ground and excited states, the photon can be absorbed and the atom excited to the upper energy level. However, if the atom is moving towards the laser light, it will see the laser frequency Doppler-shifted to higher frequencies, compared to a stationary observer. Therefore, the atom can only absorb the photon if the laser frequency is lower than the resonant frequency by an amount corresponding to the Doppler shift. If the photon is absorbed, the momentum of the atom will be reduced by an amount equal to the photon momentum. A short time later, the spontaneous emission of a photon will return the atom to the ground state and modify its momentum again. Although due to the Doppler shift the photon absorption can only occur in case of counter-propagating atom and laser beams, for the event of spontaneous emission, the probability of emitting a photon in any direction is equal. Considering a sufficiently large number of interactions between the atom and the incoming light, the atom momentum will be reduced by an amount proportional to the number of absorbed photons.

The absorption and re-emission mechanism is similar for trapped ions providing that the frequency of oscillation within the trap is significantly lower than the resonance linewidth. In this case when the difference between the laser frequency and the

resonance frequency is bigger than the atomic linewidth, photons can be absorbed only when the laser is directed against the ion movement. In the case when the laser frequency is just below the resonance frequency, the probability of absorbing a photon during the movement towards the laser is higher than in the case when the laser beam and the ion are moving in the same direction. Therefore, in both cases the interactions of the ion with the laser light lead to a cooling of the ion.

2.4.1.5 Clock transition detection

Observation of the light absorption by an ion or atom at the frequency corresponding to a strong allowed transition can easily be realised by detecting the resonance fluorescence. However this method cannot be used to probe the weak forbidden transition. In this case the detection is realised using the electron shelving technique [86, 87] described below.

Consider an ion with three energy levels as shown in Fig. 2.7: the ground state, a short-lived excited state and a metastable excited state with a long lifetime. In this case transitions between the ground state and the short-lived excited state have a very high probability, compared to the transitions between the ground state and the metastable state. When laser light with a wavelength corresponding to the transition between the ground state and the short-lived state is applied to the ion, the ion will absorb this and subsequently spontaneously re-emit photons. In the absence of other influences, the ion will cycle between the ground and the short-lived states emitting one photon per cycle. As a result of the short lifetime of the excited state, fluorescence corresponding to the photon emission from the short-lived state will be observed. Now, if in addition a second laser with a wavelength corresponding to the transition between the ground and metastable states is switched on, there is a probability of the ion making a transition between these two levels. However, due to the long lifetime of the metastable state, the probability of this transition is significantly smaller than the probability of the transition between the ground and the short-lived states. Even so,

when a transition to the metastable state takes place, transitions between the ground and the short-lived states can no longer be excited as long as the electron is “shelved” in the metastable state. This effect is observed as an abrupt end of the fluorescence produced by the transition between the short-lived and the ground states. Therefore, observing the presence or the absence of the fluorescent light resulting from the strong transitions between the ground and the short-lived states, the weak transition between the ground and the metastable states can be detected with an efficiency close to 100%. This effect is illustrated in Fig. 2.10.

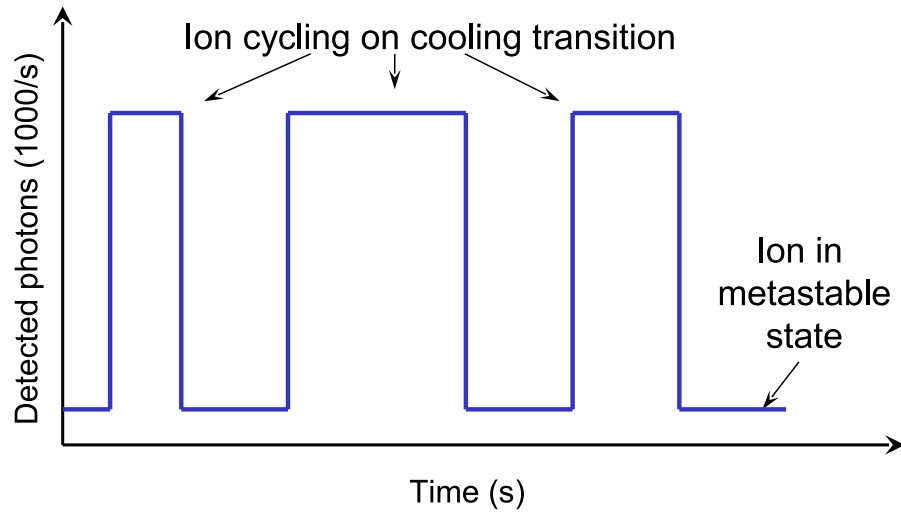


Figure 2.10: Schematic diagram of electron shelving: fluorescence from a single ion as a function of time. The abrupt jumps in fluorescence are due to quantum jumps as the ion is shelved in the metastable state and unable to fluoresce until it returns to the ground state.

2.4.2 Characterisation of frequency stability

The important properties of a frequency standard are its reproducibility, accuracy and stability. Reproducibility is the degree to which a standard can be replicated in time and location. Preferably, reproducibility is provided by an intrinsically stable property, e.g. the frequency of the transition between the two hyperfine levels of

the ground state of the Cs atom. Accuracy is the measure of uncertainty associated with the measurement of the given frequency including random errors and systematic shifts. Stability is a measure of how constant a frequency produced by the standard is.

For a device producing a signal

$$I(t) = I_0(t)\cos(2\pi\nu_0 t + \phi(t)), \quad (2.7)$$

the normalised time deviation

$$x(t) = \frac{\phi(t)}{2\pi\nu_0} \quad (2.8)$$

and the instantaneous fractional frequency deviation

$$y(t) = \frac{dx(t)}{dt} = \frac{\Delta\nu(t)}{\nu_0}, \quad (2.9)$$

where $\Delta\nu(t)$ is the frequency difference from the nominal absolute frequency of the device ν_0 , can give an instantaneous measure of the device accuracy. To obtain the information about the influence of noise on the stability of a frequency standard and its performance at different time scales statistical measurements have to be used. Since noise processes in clocks are far from Gaussian, standard statistical measures like the mean and the standard deviation cannot be used to describe their stability. The most commonly used measure is the two-sample or Allan variance (AV). In this case the Allan deviation – the square root of Allan variance – is analogous to the standard deviation.

2.4.2.1 Amplitude and phase noise

An ideal sine wave generator produces a voltage that changes in time as

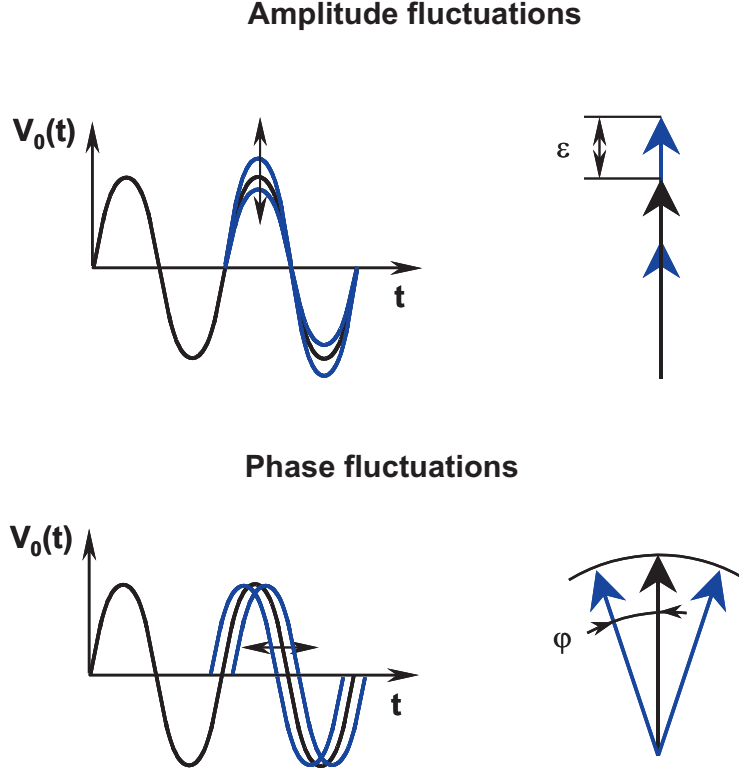


Figure 2.11: Phasor representation of amplitude and phase noise [picture courtesy of Dr. Marra].

$$V(t) = V_0 \sin(\omega_0 t + \varphi_0) \quad (2.10)$$

where V_0 is the peak signal amplitude, ω_0 is the angular frequency and φ_0 is a constant phase shift. However, the sine-wave signal can be perturbed by noise. In this case, amplitude variations (amplitude noise) or phase variations (phase noise) arise and the instantaneous signal is described as [88]

$$V(t) = [V_0 + \epsilon(t)] \sin(\omega_0 t + \varphi_0 + \delta\varphi(t)) \quad (2.11)$$

where $\epsilon(t)$ and $\delta\varphi(t)$ represent fluctuations of the signal amplitude and phase respectively. The concept of amplitude and phase noise can also be illustrated using the

phasor representation as shown in Fig. 2.11.

One method of measuring phase noise is based on the comparison of two signals of the same frequency. In this case the relative phase between the two signals can be measured with a double-balanced mixer, which if the two input signals are in phase quadrature, acts as a phase detector. The output consists of small voltage fluctuations proportional to the phase fluctuations. The amplitude noise can be measured by measuring the power fluctuations. A power detector produces a voltage that is linearly proportional to the power. In order to obtain the power spectral density (PSD) from the voltage fluctuations a Fast Fourier Transform (FFT) analyser is used. PSD is the frequency response of a signal, which shows the distribution of power over frequency. The PSD of fractional frequency fluctuations can be described as a superposition of five independent noise processes [89]

$$S_y(f) = \sum_{\alpha=-2}^{\alpha=2} h_{\alpha} f^{\alpha}, \quad (2.12)$$

where h_{α} is a constant scale factor and $-2 \leq \alpha \leq 2$ is an integer. On a log-log plot the contributions to Eq. 2.12 can be identified by their slope and the noise mechanisms can be distinguished using the value of α as summarised in Table 2.1. PSD plots are also useful for revealing the origin of frequency noise, e.g. acoustic noise, as discussed in Section 4.7.1.2.

2.4.2.2 Allan variance

The normalised time deviation $x(t)$ measured in seconds and the dimensionless instantaneous fractional frequency deviation $y(t)$ given by Eq. 2.8 and Eq. 2.9 respectively, can be used to determine the normalised frequency deviation averaged over the time interval τ as

$$y_i = \frac{x_{i+1} - x_i}{\tau}, \quad (2.13)$$

where x_i and x_{i+1} are the time difference from the clock's nominal value measured at the beginning and the end of τ . The change in y from one time interval to the next

$$\Delta y_i = y_{i+1} - y_i \quad (2.14)$$

gives a measure of instability, which can be expressed as Allan variance

$$\sigma_y^2(\tau) = \frac{1}{2} \langle (\Delta y_i)^2 \rangle, \quad (2.15)$$

where $\langle \rangle$ denotes an infinite time average. Since an infinitely long data set is not possible, an approximation of the Allan variance for a series of N measurements can be found as [90]

$$\sigma_y^2(\tau) \cong \frac{1}{2(N-2)} \sum_{i=1}^{N-2} (\Delta y)^2 = \frac{1}{2(N-2)\tau^2} \sum_{i=1}^{N-2} (x_{i+2} - 2x_{i+1} + x_i)^2. \quad (2.16)$$

A statistical analysis of this equation shows that five different noise types, characterised by different slopes of the Allan variance, can be identified, as shown in Fig. 2.12. The origin of these noise types [89, 90] is outlined below and the summary of the corresponding slopes of the PSD and the Allan variance is given in Table 2.1.

1. White phase noise is broadband noise created during the measurement process by generator and detectors.
2. Flicker phase noise arises from noisy electronic components such as amplifiers and frequency multipliers.
3. White frequency noise is the noise in the feedback loop used to lock an oscillator to a frequency reference arising from the shot noise in the number of atoms that are

Type of noise	Slope of $S_y(f)$	Slope of $\sigma_y^2(\tau)$
White phase noise	2	-2
Flicker phase noise	1	-2
White frequency noise	0	-1
Flicker frequency noise	-1	0
Random walk frequency noise	-2	1

Table 2.1: Summary of noise types and corresponding slopes of the PSD $S_y(f)$ and Allan variance $\sigma_y^2(\tau)$ on a log-log plot.

interrogated or Johnson noise in the circuit resistors.

4. Flicker frequency noise is typically related to the physical resonance mechanism of the active oscillator.

5. Random walk frequency noise arises from environmental factors such as mechanical shock, vibration and temperature fluctuations.

Since the slope of the Allan variance for both white phase noise and flicker phase noise shows a $1/\tau^2$ dependency on averaging time it is not possible to distinguish between these two types of noise using this measure of stability. This problem is addressed by introducing modified Allan variance (MAV), which replaces the frequencies in Eq. 2.16 with averages over a number of adjacent intervals [89], in which case white phase noise and flicker phase noise have different slopes, as shown in Fig. 2.12.

2.4.3 Optical frequency standards performance

A number of optical frequency standards based on narrow transitions in trapped ions and neutral atoms are being investigated in laboratories worldwide. Each of these standards has its own advantages and disadvantages as a potential optical clock when intrinsic sensitivity to environmental perturbations, transition parameters and

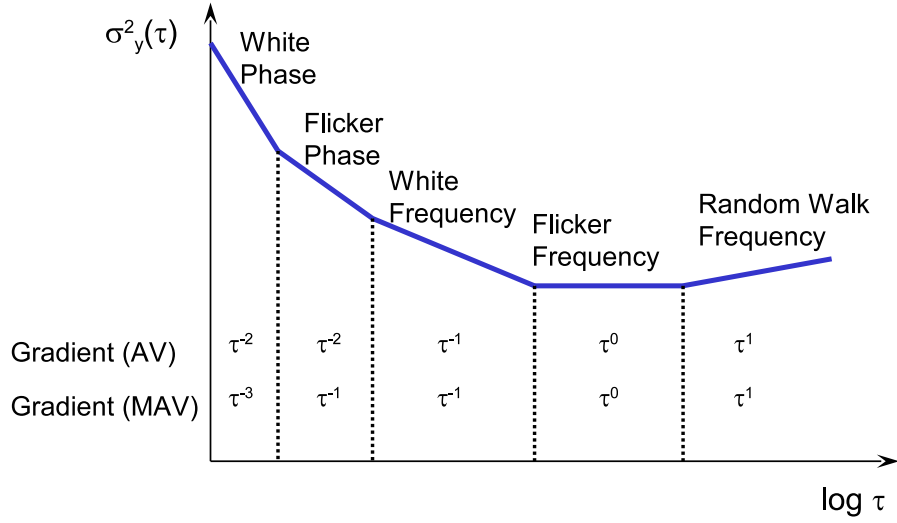


Figure 2.12: Schematic of variance as a function of averaging time, illustrating the gradients of Allan variance (AV) and Modified Allan variance (MAV) corresponding to different types of noise.

complexity of the experimental arrangement are compared. The laser-cooled atoms as well as the single ions considered as potential candidates for optical frequency standards of high stability and accuracy are summarised in table 2.2. Note that the uncertainties shown in this table represent the current state of development, not the fundamental limit to the accuracy.

In general, optical frequency standards based on single trapped ions can be divided into two groups: standards based on ions with alkali-like or quasi-alkali-like atomic structure (Ca^+ , Sr^+ , Yb^+ and Hg^+) and ions with two valence electrons, which have an atomic structure similar to that of the alkaline earth elements ($^{27}\text{Al}^+$ and $^{115}\text{In}^+$). In the first group the lowest excited ^2D states lie below the lowest ^2P states in energy, therefore the electric quadrupole transition between the metastable ^2D state and the $^2\text{S}_{1/2}$ ground state can be used as a clock transition. These transitions have natural linewidths in the range 0.2–3 Hz. The best accuracy in this group of clocks reported to date is for the $^{199}\text{Hg}^+$ clock, with an estimated systematic fractional frequency uncertainty of 1.9×10^{-17} [92]. The latest development of the $^{88}\text{Sr}^+$ clock reduced

Standard	λ , nm	$\Delta\nu_{\text{nat}}$, Hz	$(\delta\nu/\nu)_{\text{estimated}}$	$(\delta\nu/\nu)_{\text{freq}}$	Reference
$^{27}\text{Al}^+$	276	8×10^{-3}	8.6×10^{-18}	6.5×10^{-16}	[91], [92]
$^{199}\text{Hg}^+$	282	1.8	1.9×10^{-17}	6.5×10^{-16}	[92], [93]
$^{88}\text{Sr}^+$	674	0.4	2.2×10^{-17}	2.0×10^{-15}	[94]
$^{171}\text{Yb}^+$	467	$\sim 10^{-9}$	7.1×10^{-17}	8.0×10^{-16}	[95]
$^{171}\text{Yb}^+$	436	3.1	4.4×10^{-16}	1.1×10^{-15}	[12]
$^{40}\text{Ca}^+$	729	0.14	7.8×10^{-16}	2.4×10^{-15}	[96], [97]
$^{115}\text{In}^+$	237	0.8		1.8×10^{-13}	[98]
^{87}Sr	698	8×10^{-3}	1.1×10^{-16}	3.1×10^{-16}	[99]
^{171}Yb	578	4.4×10^{-3}	3.4×10^{-16}	1.4×10^{-15}	[100]
^1H	243	1.3	1.6×10^{-15}	4.2×10^{-15}	[101]
^{199}Hg	266	~ 0.1	5.7×10^{-15}	5.7×10^{-15}	[102]
^{40}Ca	657	375	6.6×10^{-15}	7.5×10^{-15}	[103]
^{201}Hg	266	0.1	5×10^{-12}		[104]
^{174}Yb	578	field dependent	1.5×10^{-15}	1.7×10^{-15}	[105]
^{88}Sr	698	field dependent	6.8×10^{-15}	7.0×10^{-14}	[106]

Table 2.2: Current optical frequency standards performance. λ is the wavelength of the clock transition and $\Delta\nu_{\text{nat}}$ is its natural linewidth, $(\delta\nu/\nu)_{\text{estimated}}$ is the estimated systematic frequency uncertainty of the standard and $(\delta\nu/\nu)_{\text{freq}}$ is the uncertainty of the measured absolute frequency of the transition.

its uncertainty to the similar level (2.2×10^{-17} [94]). These values are lower than the uncertainty of the best current realisation of the SI second, which at present is 2.1×10^{-16} [107].

The exception from the first group of ions is the $^{171}\text{Yb}^+$ ion, which also has an electric octupole transition to the ground state from a low-lying $^2\text{F}_{7/2}$ state with a lifetime of about six years [108]. Although this transition is much harder to drive than the electric quadrupole transitions, the potential frequency stability is higher than achievable with the electric quadrupole transition in this ion. To date, the best reported systematic frequency uncertainty for this transition is 7.1×10^{-17} [95].

The reference transition in the second group of ions is the weakly allowed $^1\text{S}_0 - ^3\text{P}_0$ transition. The advantage of this group is potentially very low systematic frequency shifts and a narrow linewidth of 0.8 Hz in $^{115}\text{In}^+$ and 8 mHz in $^{27}\text{Al}^+$. However they require deep UV laser sources for cooling and probing, leading to experimental difficulties.

The $^{27}\text{Al}^+$ ion is particularly challenging as there is no available laser source to drive its cooling transition, so the clock transition can not be detected via the standard electron shelving technique. Therefore the $^{27}\text{Al}^+$ ion is trapped together with a “logic ion” ($^9\text{Be}^+$) that can be cooled [92]. The coupling between their motion via the Coulomb interaction facilitates sympathetic cooling of the $^{27}\text{Al}^+$ ion and its state information is mapped onto the $^9\text{Be}^+$ ion using quantum logic spectroscopy techniques [109]. This mapping is performed through the transfer mode shared by both ions, with an excitation of the motional state being produced only if the clock transition in the $^{27}\text{Al}^+$ ion was internally excited. This is the key element of quantum logic that allows the clock transition in the $^{27}\text{Al}^+$ ion to be detected.

A number of improvements to the Al-Be clock including replacement of the $^9\text{Be}^+$ logic ion with a $^{25}\text{Mg}^+$ ion whose mass closely matches that of $^{27}\text{Al}^+$, therefore providing more efficient laser cooling, are reported in [91]. These changes resulted in improvement of clock inaccuracy to 8.6×10^{-18} , the lowest inaccuracy of any optical clock

reported to date.

As described in Section 2.4.1.2, optical frequency standards based on cold neutral atoms can be studied in a trapped atom cloud and an optical lattice. Another configuration for studying of cold neutral atoms is atomic beams. One of the most interesting atomic beam standards in the optical spectral region is the two-photon 1S–2S transition in atomic hydrogen, which gives the opportunity of testing fundamental physical theories such as quantum electrodynamics. The unique property of hydrogen is the presence of a wide range of reference frequencies with the scaling factor given by the Rydberg constant which has been measured with an uncertainty of 6.6×10^{-12} [110]. The frequency of the two-photon 1S–2S transition has been measured with an uncertainty of 4.2×10^{-15} [101]. An example of a trapped atom cloud based standard is the 1S_0 – 3P_1 transition in ^{40}Ca . The absolute frequency of this clock transition has been measured with a relative uncertainty of 7.5×10^{-15} [103].

Today the most promising neutral atom based frequency standards are optical lattice clocks. For clock operation, the biggest advantage is obtained by using the spin-forbidden 1S_0 – 3P_0 clock transition in alkaline-earth atoms or the alkaline-earth-like Yb, which have extremely narrow linewidth. A number of alkaline-earth elements are being studied as possible standards today. The two undergoing the most rapid developments are Sr and Yb [3].

For bosonic (even) isotopes, the narrow clock transition is completely forbidden so a small magnetic mixing field must be added in order to use the clock transition. The advantage of using bosonic isotopes is that the transition linewidth is dependent on the strength of the applied magnetic field, so the clock performance can in principle be optimised by choosing the linewidth of the clock transition. However, in practice, fermionic isotopes have achieved better performance today (see table 2.2). The best results reported today give a fractional uncertainty of 7.0×10^{-14} for ^{88}Sr [106] and 1.5×10^{-15} for ^{174}Yb [105] bosonic isotopes.

For the fermionic (odd) isotopes, which all have nuclear spin, hyperfine-induced mix-

ing leads to the clock transition being weakly allowed. To date, the optical lattice clock with the lowest reported systematic uncertainty of 1.1×10^{-16} [99] is the ^{87}Sr clock. The absolute frequency of this clock has been measured simultaneously against the three independent caesium fountains with a total uncertainty of 3.1×10^{-16} , which was limited by the Cs fountain clock.

Another potential for the lattice clocks is a clock based on the $^1\text{S}_0\text{--}^3\text{P}_0$ transition in mercury which has relatively low sensitivity to blackbody radiation. The clock transition frequency in the ^{199}Hg isotope have been determined with a fractional uncertainty of 5.7×10^{-15} [102].

2.4.4 Frequency comb performance

As described in the previous section, state-of-the-art optical frequency standards based on laser-cooled ions and atoms demonstrate accuracy at the parts in $\times 10^{17}$ level and have the potential to be further improved. Table 2.2 illustrates that at present the accuracy of absolute optical frequency measurements is limited by the current realization of the SI second based on a microwave transition in Cs atoms. The accuracy of direct measurements of the ratio of optical frequencies, where the contribution of the microwave reference is eliminated, reaches the level of a few parts in 10^{17} [92]. To achieve such results, it is vital to ensure that the contribution of the frequency combs to the total uncertainty of the measured frequency ratio remains negligible.

The potential limitations of frequency combs have been evaluated by comparing four combs constructed at three different institutes [111]. All the combs were Ti:sapphire laser based; two of them were constructed at the National Institute of Standards and Technology (NIST) and the other two were transportable combs constructed at the Bureau International de Poids et Mesures (BIPM) and the East China Normal University (ECNU) and brought to NIST for measurements. Pairs of frequency combs

were compared and three techniques – optical heterodyne technique, nonlinear cross correlation and photodetection – were used to verify that the output modes and repetition rates have their expected frequencies. The most accurate results were obtained using the optical heterodyne technique described below.

Two phase-lock-loops were employed to servo-control f_0 and f_{rep} of the combs relative to an optical reference signal f_L from a cavity-stabilized diode laser at 657 nm. In this case, f_{rep} is given by

$$f_{\text{rep}} = \frac{f_L - f_0 - f_b}{N_L}, \quad (2.17)$$

where f_b is the beat frequency between f_L and N_L -th mode of the comb. In these experiments comb modes with the same index N were compared, thus the beat frequency between the comb lines of the two combs was given by

$$\Delta f = f^1(N) - f^2(N) = (f_0^1 - f_0^2) + N(f_{\text{rep}}^1 - f_{\text{rep}}^2) = (f_0^1 - f_0^2) + N\Delta f_{\text{rep}}. \quad (2.18)$$

Eqs. 2.17 and 2.18 allow precise values of Δf and Δf_{rep} to be determined and compared to the measured values. In most cases, the repetition rates of two combs were equal, allowing the frequency difference signal to be generated from groups of lines from each of the two combs. In a few cases, when the repetition rates were similar but not equal, the frequencies of single lines adjacent to the N_L -th mode from each of the two combs were compared. The weighted mean obtained from 10 measurements was 3.2×10^{-20} with an uncertainty of 7.8×10^{-20} . This result shows that the performance of the optical clock is not limited by the comb performance.

2.5 Summary

In this chapter the background material necessary to understand the rest of this thesis was reviewed. Firstly, the definition of the SI units of time and frequency were given and modern timescales and timekeeping were described, followed by the concept of a frequency standard as the oscillator for an atomic clock including the distinction between active and passive frequency standards.

Next, a historical overview of optical frequency measurement techniques such as frequency chains and frequency division methods was given, showing examples of early optical frequency measurements. In these experiments a number of specific optical frequencies were measured; however the task of measuring an arbitrary frequency in the optical spectral region remained extremely challenging. This challenge was resolved by the introduction of optical frequency combs, which are described in the following section.

The concept of frequency combs based on femtosecond mode locked lasers as a tool for optical frequency measurements together with the origin and necessity of stabilising the two key parameters of the frequency comb, the repetition rate f_{rep} and carrier envelope offset frequency f_0 were discussed. A description of the concept of self-referencing, the most commonly used technique for measuring f_0 , and the methods of controlling f_{rep} and f_0 were also described. This chapter also reviewed various femtosecond laser sources used for comb generation and their performance reported to date. The advantages and disadvantages of each one were highlighted allowing selection of the most suitable type of comb for the particular application.

Finally, optical clocks as one of the applications of frequency combs were reviewed. Initially the concept of an atomic frequency standard was given including a description of potential atomic references and means of their implementation as well as the techniques used for detection of the generated frequency. Secondly, methods of characterising clock performance were described, which allow parameters such as repro-

ducibility, accuracy and stability to be established. Various atomic references studied as potential candidates for optical clocks were described and their advantages and disadvantages were compared. The best performance of optical clocks based on each of these references reported to date was summarised. Lastly, tests of frequency comb performance were discussed. These show that the relative uncertainty of a femtosecond laser based frequency comb used for optical-to-optical synthesis can be as low as 8×10^{-20} , so the performance of the optical clock is not limited by the comb performance.

Chapter 3

Introduction to the NPL combs

This chapter is dedicated to the two NPL frequency combs I worked with during my project: the fibre-laser-based comb (fibre comb) and the low-repetition-rate Ti:Sapphire-laser-based comb (LRR comb). A frequency measurement of the 436 nm clock transition in $^{171}\text{Yb}^+$ ion performed using the fibre comb is detailed in Chapter 6. The work involving the LRR comb is described in Chapter 4. Whilst the fibre comb is based on a Menlo Systems FC1500 optical frequency synthesiser and therefore only minor changes from the original design have been made, the LRR comb was constructed at NPL and has gone through a number of improvements during the last few years. This chapter describes the design of both combs as they were at the beginning of my project.

3.1 Fibre-laser-based-comb

The NPL transportable fibre-laser-based frequency comb is based on a Menlo Systems FC1500 optical frequency synthesiser [112] and is shown in Fig. 3.1. It consists of a mode-locked femtosecond fibre laser operating at a centre wavelength of about 1550 nm with a repetition rate of 100 MHz. There is a small free-space section in the

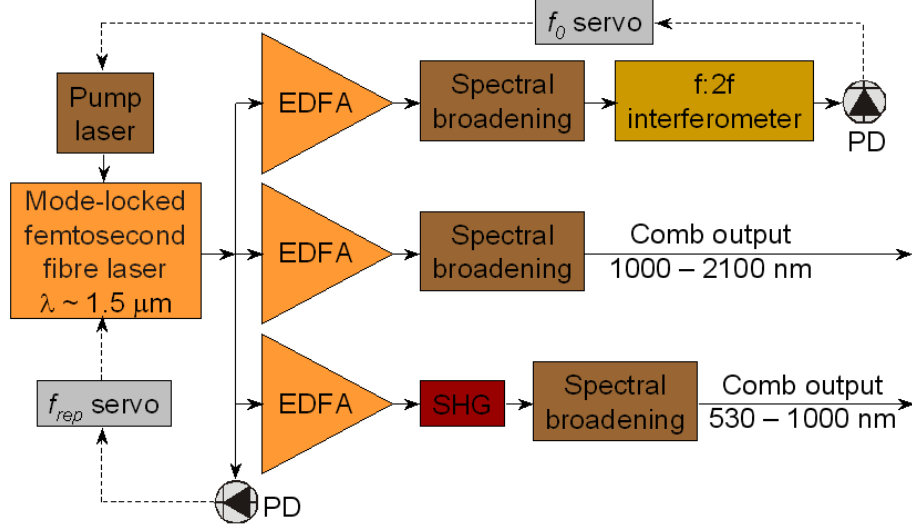


Figure 3.1: Schematic of the NPL fibre-based frequency comb

laser, which is used for the repetition frequency adjustment. The repetition rate can be tuned over approximately 400 kHz by moving the end mirror, which is mounted on a translation stage with fine adjustment possible using a PZT. The repetition frequency is measured using a PIN photodiode in the laser head which detects up to the 10th harmonic of f_{rep} . The output power of the mode-locked laser is split between three independent branches, where it is amplified by erbium doped fibre amplifiers (EDFAs) and used to generate three phase coherent optical frequency combs.

The first comb is used for the carrier-envelope offset frequency stabilisation. As explained in Section 2.3.1.1, in order to implement the f -to- $2f$ self-referencing technique the spectrum should span at least an octave. The amplified signal is therefore coupled into a non-linear fibre, which broadens the spectrum to cover the range from approximately 1000 nm to 2100 nm. The f -to- $2f$ interferometer is set up in a collinear single-arm configuration. A PPLN crystal is used to double the comb modes at 2100 nm and after that an interference filter selects a narrow band around 1050 nm. The beat frequency between doubled and fundamental light has a typical signal-to-noise ratio (SNR) of 40-45 dB in a 250 kHz resolution bandwidth. The offset frequency is stabilised by feedback to the pump laser diode current providing the re-

quired power change.

The other two branches are used for frequency measurements in different spectral regions. In one of them the output of the EDFA is connected to a second non-linear fibre to generate an infrared comb extending from 1000 nm to 2100 nm. In the third branch the laser light is amplified by an EDFA and frequency doubled using a PPLN crystal. The resulting narrow band frequency comb centred at about 780 nm is spectrally broadened in microstructure fibre to cover the wavelength range of 530 – 1000 nm. It is possible to expand the spectral range down to 500 nm by changing the microstructure fibre.

A computer controls the operation of the fibre-laser-based optical frequency comb. This includes driving the stepper motor for the laser repetition rate control, adjustment of the voltages applied to the fibre squeezers that are used to change the polarisation in the laser cavity and the EDFAs in order to maximise the intensity of the beat signals, as well as monitoring the output voltages of the locking circuits and the RF power in the beat signals. Such computer control of the fibre-based comb operation makes it possible to maintain stable locking for many hours or even days.

The fibre comb is mounted on a wheeled aluminium frame with dimensions 0.95×1.72 m and the maximum height of the system is 1.21 m as shown in Fig. 3.2. The opto-mechanics support breadboards are separated from the aluminium frame by a 5 mm rubber sheet for vibration isolation. This arrangement allows transportable operation, which was tested by moving the comb between two laboratories, including travel out of doors [113]. This test showed that the only adjustments to the frequency comb necessary in order to perform measurements of a laser frequency were adjustments to the EDFA squeezers to set up the beat with the laser.

In order to trace the optical frequency back to the SI second, the frequency comb is referenced to a stable source of microwave frequency during the measurements, which in turn can be calibrated using a Cs atomic clock. Therefore, all the synthesisers and frequency counters used with the frequency combs are referenced to the same

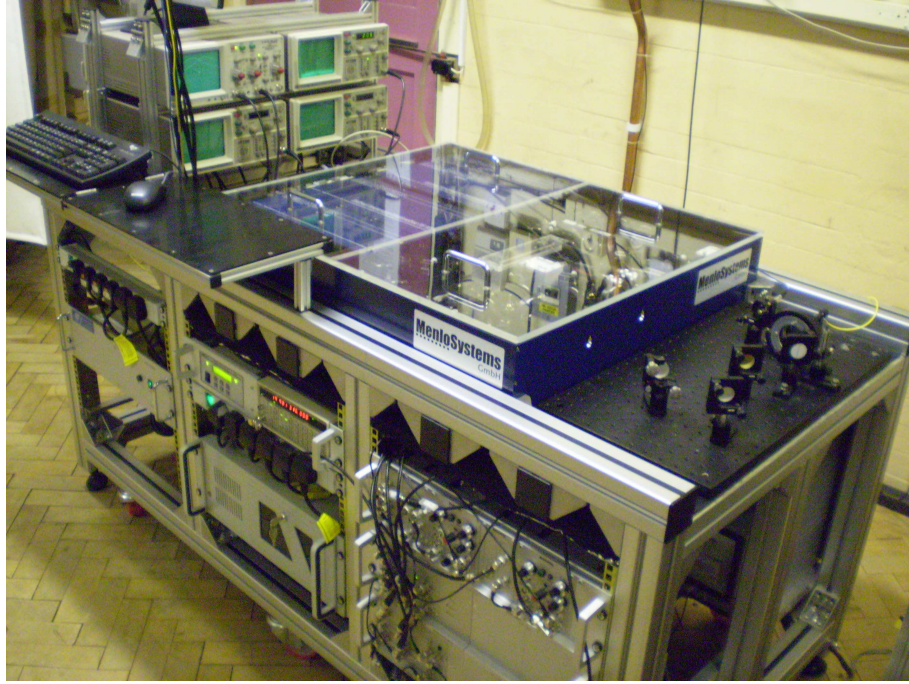


Figure 3.2: The layout of NPL fibre-based transportable frequency comb

frequency source. In transportable mode the fibre comb is referenced to the 10 MHz output signal from a GPS-referenced quartz oscillator providing a reference signal stable to a few parts in 10^{12} as described in Section 5.1.3. If a higher degree of accuracy is required for the frequency measurements, the comb can be referenced to the 10 MHz signal from a hydrogen maser forming part of the clock ensemble generating the timescale UTC(NPL) as described in Section 5.1.2. This reference provides traceability to the SI second with a relative standard uncertainty of better than 1×10^{-14} . An example of a frequency measurement performed using the maser-referenced fibre comb is detailed in Chapter 6.

3.2 Low-repetition-rate Ti:Sapphire comb

The LRR comb is the oldest NPL comb and, naturally, progress in the field during the last decade, to which NPL has made significant contributions, led to a number

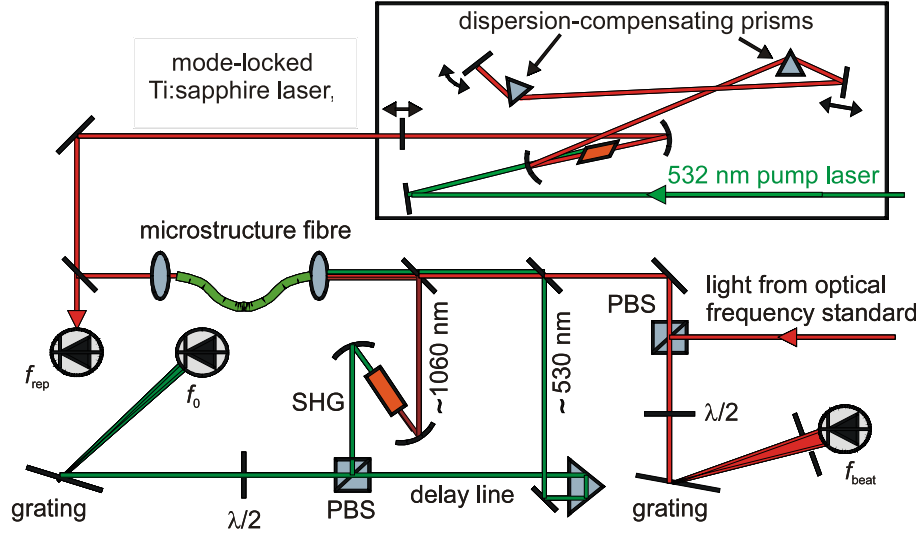


Figure 3.3: Schematic of the original optical design of the NPL low repetition rate Ti:Sapphire frequency comb [picture courtesy of Dr. Margolis].

of improvements from the original design. Although the basic concept of this comb remains the same, some of the functional building blocks have been redesigned as described in Chapter 4. The state of the LRR comb before the implementation of these improvements is described in this section.

3.2.1 Optical arrangement

The low repetition rate Ti:Sapphire frequency comb [114], [115] is shown in Fig. 3.3.

This octave-spanning comb is based on a Kerr-lens mode-locked Ti:sapphire laser with spectral broadening in photonic crystal fibre. The laser has a linear cavity design with dispersion compensation provided by a pair of intracavity prisms and is pumped with 4.5 W of single frequency light at 532 nm. The pulse repetition rate f_{rep} , determined by the laser cavity length, is around 87 MHz and is fine controlled with a piezo element mounted cavity fold mirror. The laser produces 10–15 fs pulses with a spectral full width at half maximum (FWHM) of typically 30–35 nm centred about 810 nm and the average output power is 600 mW. In order to broaden the comb spectrum up to

the full octave approximately 20 cm of microstructure fibre is used. A small portion of the laser output is split off for the repetition frequency detection. The intermode beat at the ninth harmonic of f_{rep} is detected with an avalanche photodiode (APD) and used for counting and stabilisation of f_{rep} .

The carrier envelope offset frequency f_0 is determined by the f -to- $2f$ self-referencing technique [49]. A short-wavelength-pass dichroic beam splitter separates comb lines at wavelengths longer than approximately 950 nm and light in a bandwidth of a few nanometers around 1060 nm is frequency doubled in a single pass through a KTP crystal. After that comb lines in an equivalent bandwidth around 530 nm are recombined with the frequency-doubled light using a polarizing beam splitter (PBS). To ensure temporal coincidence of the frequency doubled and short-wavelength pulses a variable delay line is used in the short-wavelength beam path. The beat frequency between modes centred at 530 nm and frequency-doubled modes is detected using an APD after spectral filtering by a diffraction grating, providing a signal at the offset frequency f_0 .

The set-up for detection of the beat frequency f_b between the optical standard being measured and the nearest comb mode is similar to the arrangement for f_0 detection. A PBS superimposes the signal from the optical standard with the comb light, a half-wave plate is used for the beat signal optimisation and f_b is detected by an APD after spectral filtering by a diffraction grating.

3.2.2 Frequency counting and comb stabilisation

To use the frequency comb for absolute frequency measurements the repetition rate f_{rep} , the offset frequency f_0 and the beat frequency f_b have to be measured simultaneously. Also, the repetition rate f_{rep} and the offset frequency f_0 need to be stabilised to the radio frequency (RF) reference frequency using a feedback loop.

3.2.2.1 Repetition rate

Firstly the beat at the ninth harmonic of f_{rep} is down-converted by mixing with the output of an IRF 2023A RF synthesiser at 820 MHz to generate a signal at 9.8 MHz. Next this signal is mixed with a 9.8 MHz signal from an IFR 2023A RF synthesiser in an analogue phase comparator to provide a DC error signal, which is used for driving the piezo element supporting the cavity fold mirror thereby controlling the cavity length and therefore the comb repetition rate. To measure f_{rep} with a precision greater than can be achieved by direct counting the 9.8 MHz signal is mixed with a 10 MHz signal from a hydrogen maser to obtain a difference signal at 200 kHz. This signal is used to phase-lock a 200 MHz voltage-controlled oscillator (VCO) using a GEC Plessey SP8400 frequency divider with a division ratio of 1000. The VCO output is counted using an Agilent 53132A frequency counter. The repetition frequency f_{rep} is determined from the counted frequency f_c and the synthesiser frequency f_s as:

$$f_{\text{rep}} = \frac{1}{9} \left(f_s - 10 \text{ MHz} + \frac{f_c}{1000} \right). \quad (3.1)$$

The precision of this measurement technique is more than three orders of magnitude higher compared to direct counting.

3.2.2.2 Offset and beat frequencies

The SNR measured in the f_0 and f_b beats is typically about 20–25 dB in 100 kHz bandwidth, which is insufficient for direct counting. A 200 MHz analogue tracking oscillator for the f_b beat and a 30 MHz tracking oscillator for the f_0 beat are used to filter and amplify the beats to provide a countable signal. To set the beat frequency f_b into the tracking oscillator range the pulse repetition rate is adjusted slightly by changing the synthesiser frequency f_s .

To stabilise the offset frequency the signal from the 30 MHz tracking oscillator is

mixed with a 30 MHz signal from a Stanford Research Systems DS345 synthesiser in an analogue phase comparator to provide a DC error signal, which is used for driving the piezoelectric stack adjusting the tilt of the cavity end mirror.

The frequencies f_0 , f_c and f_b are counted by Agilent 53132A frequency counters, which are synchronously gated and read by PC-based software via a GPIB interface. As for the fibre comb, all the synthesisers and frequency counters are referenced to the 10 MHz signal from a hydrogen maser. If accuracy better than 1×10^{-14} is required then the hydrogen maser can be referenced to the NPL caesium fountain primary frequency standard [116].

3.3 Summary

In this chapter the designs of the NPL fibre-laser-based comb and the low-repetition-rate Ti:Sapphire-laser-based comb as they were at the beginning of my project have been described.

Firstly, a schematic diagram of the fibre comb was given and the purpose and design of the three independent branches derived from the mode-locked fibre laser were described. Next, the arrangement of the comb allowing for transportable operation was introduced, and the possibility of using different reference signals, either a signal from a GPS-referenced quartz oscillator or a signal from a hydrogen maser, which provide different degrees of accuracy as detailed in Chapter 5, was discussed.

Secondly, the optical arrangement of the KLM Ti:Sapphire laser including the detection schemes for the f_{rep} , f_0 and f_b frequencies was described. The methods used for counting and stabilisation of these frequencies were also outlined. The main limitation of the original design was the degradation of SNR in the f_0 and f_b beat signals with time, which made it difficult to keep these beats locked for longer than about an hour. One of the reasons for this SNR degradation was the design of the LRR

comb, which was based on a single microstructure fibre for spectral broadening, and so to obtain the f_0 and f_b beats, the generated supercontinuum had to be optimised in three spectral regions simultaneously. Consequently, the highest obtained SNR in both beats was limited to about 20–25 dB in a 100 kHz bandwidth. Another contribution to the low SNR in the f_0 beat was the low intensity of the second harmonic signal generated in the non-linear crystal. To address these limitations, several improvements were made to the design of the LRR comb, which are described in following chapter.

Chapter 4

Improvements to the Ti:Sapphire low repetition rate comb

The previous chapter describes the design of the low repetition rate (LRR) Ti:Sapphire comb at the beginning of my project. The main limitation of this design for long frequency measurements was the necessity of making frequent adjustments to the f_0 and f_b beat signals as the degradation of signal to noise ratio (SNR) in these beats with time made it difficult to keep these beats locked for longer than about an hour. The novel self-referencing scheme described in this chapter improved the SNR in the f_0 beat as well as the long-term stability of the beat signal, which resulted in extension of the time of continuous operation without any adjustments from less than one hour to several days.

This chapter gives the details of improvements to the LRR comb design. Firstly, changes to the spectral broadening and the f_0 beat signal stabilisation system implemented by the other members of the group at the beginning of my project are described. Next, the enhancement of the intensity of the second harmonic signal generated in non-linear crystals as a result of using different mechanisms of second harmonic generation is theoretically evaluated. After that, the group velocity disper-

sion in the self-referencing system is assessed and various methods of compensation are reviewed. Finally, a novel self-referencing scheme based on Wollaston prisms is described in detail and the results of the evaluation of the phase-noise performance of this system reported in [10, 117] are presented.

4.1 Modifications to the spectral broadening scheme

One of the drawbacks of the original Ti:Sapphire comb setup (Fig. 3.3) was the difficulty of obtaining high SNR in both the f_0 and the f_b beats at the same time. This was because the octave-spanning comb generated in a single microstructure fibre must be optimised in three spectral regions simultaneously: around f and $2f$ to obtain the f_0 beat, and in the region of the measured frequency to get the f_b beat. To ease this constraint, the setup was modified so that the light from the Ti:Sapphire laser was now split between two branches, each of which contained a microstructure fibre for spectral broadening as shown in figure 4.1. The first branch was used to create the octave spanning spectrum for f -to- $2f$ self-referencing, while the second was used for the beat with the optical standard. This enabled the SNRs of the two beat signals f_0 and f_b to be optimised independently.

A further improvement to the stability of the f_0 and f_b beats was made by changing the type of microstructure fibres used. In the original system the most frequently required adjustment was the alignment of the laser light into the bare cleaved microstructure fibre, which had a $1.8\ \mu\text{m}$ core diameter. The alignment typically had to be optimised every hour. The original microstructure fibre was therefore replaced by connectorised fibre made by Crystal Fibre, consisting of 20 cm of NL-PM-750 fibre with collapsed holes at the output end and about $100\ \mu\text{m}$ of single mode fibre (SMF) spliced to the input end. The $6\ \mu\text{m}$ diameter core of the SMF offers much better tolerance to misalignment and enables the f_0 beat signal to be counted reliably for many hours as reported in [118]. The new fibre not only reduced the need for read-

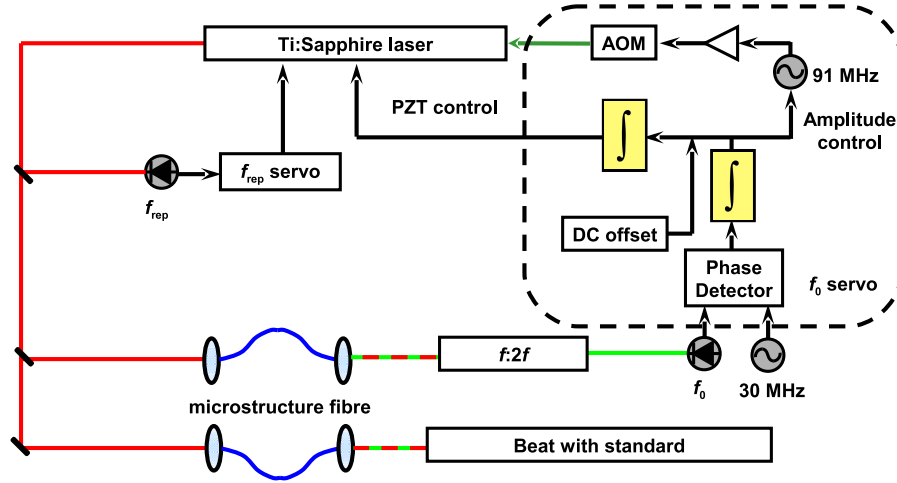


Figure 4.1: Schematic diagram of the LRR comb layout employing two microstructure fibres and a combination of fast and slow servo loops for f_0 stabilisation.

justment, it also reduced the risk of damaging the fibre by high intensity laser light; furthermore, it made cleaning of the fibre ends possible, eliminating the need for it to be periodically re-cleaved.

4.2 Carrier envelope offset frequency stabilisation

In the original setup the f_0 beat was stabilised by adjusting the tilt of the cavity end mirror in the Ti:Sapphire laser using a split tubular piezoelectric transducer (PZT). This had the advantage of being able to compensate for large changes in f_0 , but because of the low bandwidth of the actuator (a few kHz), the servo system was unable to remove high frequency noise. To improve the stabilisation, a fast servo loop was added (figure 4.1). The fast loop was realised using an acousto-optic modulator (AOM) inserted into the pump laser beam to control its power [119]. The resulting modification to the non-linear refractive index of the Ti:Sapphire crystal provided a means for fast control of f_0 . Although either of the loops could be used separately, the combination of the AOM and the PZT enabled both a tight lock and a wide frequency range to be achieved. Furthermore, cascading two servo loops provided higher gain at

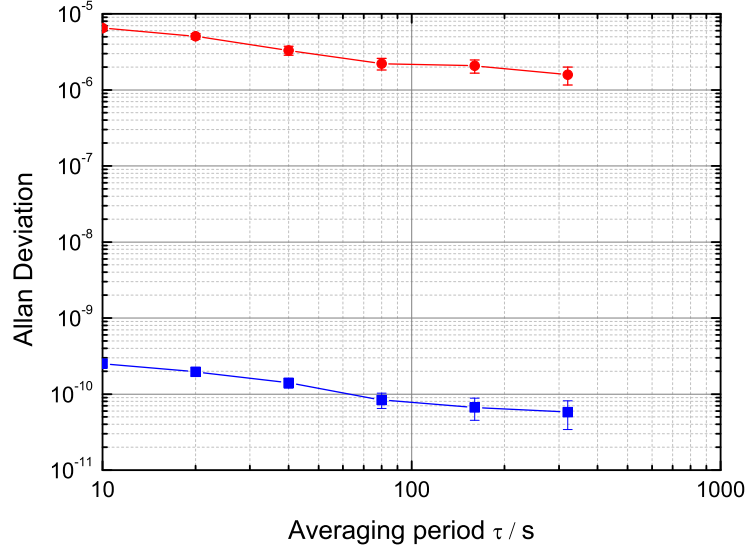


Figure 4.2: Fractional frequency instability of the stabilized f_0 beat at 30 MHz for the original servo system using only a piezo actuator (red circles) and for the new servo system, which also uses an AOM (blue squares).

low frequencies. Figure 4.2 shows the resulting improvement of more than four orders of magnitude in the stability of the f_0 beat.

4.3 Improvement to the frequency doubling efficiency in non-linear crystals

As described in Section 2.3.1.1, the f -to- $2f$ self-referencing technique is based on the measurement of a beat between a fundamental wavelength from the high frequency end of the comb and the second harmonic of light from the low frequency end. Therefore, efficient frequency doubling is crucial for the realisation of an f -to- $2f$ self-referencing interferometer. The original system was built around a 6 mm long KTP crystal designed for type II phase matching at a fundamental wavelength of 1047 nm.

This section explains the mechanism of second harmonic generation in non-linear crystals and demonstrates that the power of the second harmonic can be increased by replacing the original KTP crystal with a PPKTP crystal, leading to higher SNR in the f_0 beat. The increase of SNR in the f_0 beat was calculated and experimentally verified as shown in Section 4.3.4.

4.3.1 Second harmonic generation in KTP

In this section the key parameters of the second harmonic generation (SHG) for the original KTP crystal used in the self-referencing setup are presented.

4.3.1.1 Phase-matching

As the fundamental wave propagates through a non-linear crystal, second harmonic radiation is generated at each point within the crystal [120]. For a useful frequency doubled output beam it is essential that the light generated at each point interferes constructively with the existing wave. This means that the phase velocity of the fundamental and second harmonic waves must be equal, a requirement known as phase matching. The natural birefringence of anisotropic crystals is used to compensate dispersion and therefore satisfy the phase matching requirement.

There are two types of phase matching. Type I involves two fundamental waves of parallel polarisation and the relation between the refractive indices of the fundamental wave ($n_{\omega,1}$ and $n_{\omega,2}$) and the second harmonic ($n_{2\omega,1}$ and $n_{2\omega,2}$) is given by

$$n_{2\omega,1} = n_{\omega,2}, \quad (4.1)$$

where 1 and 2 indicates the two possible values of the refractive index in a given direction of propagation. Type II phase matching involves two orthogonally polarised fundamental waves and the relation between the refractive indices is

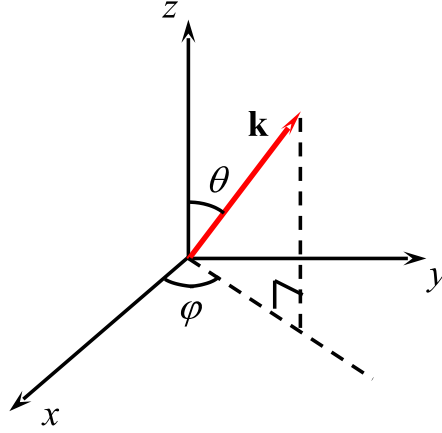


Figure 4.3: Relation of the polar angles θ and φ describing the propagation direction with respect to orthogonal x , y , z axes.

$$n_{2\omega,1} = \frac{1}{2} (n_{\omega,1} + n_{\omega,2}), \quad (4.2)$$

where $n_{\omega,1} \leq n_{\omega,2}$.

Since the effective nonlinear coefficient d_{eff} of KTP is much bigger for Type II phase matching than for Type I [121], for efficient interactions Type II SHG was considered.

The refractive indices $n_{\omega,i}$ and $n_{2\omega,i}$ ($i = 1, 2$) of the fundamental and harmonic frequencies for an arbitrary incident direction must satisfy the following equations [122]:

$$\frac{\sin^2\theta \cos^2\varphi}{n_{\omega,i}^{-2} - n_{x,\omega}^{-2}} + \frac{\sin^2\theta \sin^2\varphi}{n_{\omega,i}^{-2} - n_{y,\omega}^{-2}} + \frac{\cos^2\theta}{n_{\omega,i}^{-2} - n_{z,\omega}^{-2}} = 0 \quad (4.3)$$

$$\frac{\sin^2\theta \cos^2\varphi}{n_{2\omega,i}^{-2} - n_{x,2\omega}^{-2}} + \frac{\sin^2\theta \sin^2\varphi}{n_{2\omega,i}^{-2} - n_{y,2\omega}^{-2}} + \frac{\cos^2\theta}{n_{2\omega,i}^{-2} - n_{z,2\omega}^{-2}} = 0 \quad (4.4)$$

where $n_{x,\omega}$, $n_{y,\omega}$, $n_{z,\omega}$, and $n_{x,2\omega}$, $n_{y,2\omega}$, $n_{z,2\omega}$ are the principal indices of refraction at a given temperature. The phase matching directions for type II SHG are the result

	A	B	$C/\mu\text{m}^2$	$D/\mu\text{m}^{-2}$
n_x	2.16747	0.83733	0.04611	0.01713
n_y	2.19229	0.83547	0.04970	0.01621
n_z	2.25411	1.06543	0.05486	0.02140

Table 4.1: Sellmeier equation coefficients for KTP, taken from reference [121].

of numerical solution for θ and φ , satisfying equations 4.2 – 4.4.

The refractive indices at the desired wavelength were calculated using the Sellmeier equation

$$n^2 = A + \frac{B}{1 - \frac{C}{\lambda^2}} - D\lambda^2, \quad (4.5)$$

where λ is expressed in microns and the coefficients are given in table 4.1.

The refractive indices calculated for KTP at the fundamental wavelength of 1047 nm and its second harmonic are shown in table 4.2. The corresponding phase matching curve is shown in figure 4.4. This plot shows all possible phase matching directions in one quadrant for Type II SHG. In order to minimise Poynting vector walk-off it was logical to choose propagation along a principal crystal axis, where one of the angles θ or φ is either 0° or 90° , so $\theta = 90^\circ$ was chosen for our crystal.

	Fundamental	Second Harmonic
n_x	1.73862	1.78031
n_y	1.74633	1.79120
n_z	1.83090	1.89218

Table 4.2: Refractive indices along the x , y and z axes of a KTP crystal at 1047 nm and 523.5 nm.

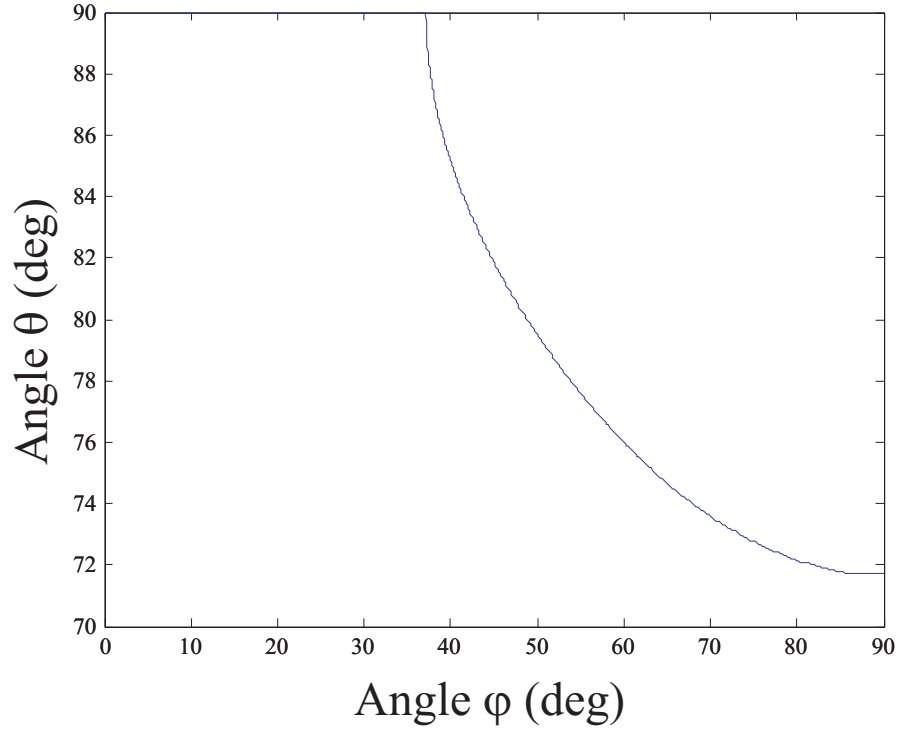


Figure 4.4: Phase matching angles for Type II phase matching in KTP at 1047 nm.

4.3.1.2 Non-linear susceptibility and effective nonlinear coefficient

The non-linear polarisation $P(t)$ is related to the applied electric field $E(t)$ by the three-dimensional non-linear susceptibility tensor \mathbf{d}_{ijk} such that,

$$P_i(t) = \sum_{ijk} 2d_{ijk}\epsilon_0 E_j(t)E_k(t). \quad (4.6)$$

The conversion efficiency of SHG depends on the value of the effective nonlinear coefficient d_{eff} , which is a function of the material nonlinear coefficients d_{ijk} and the E -field polarisation directions. The interaction of two applied fields E_j and E_k induces a second order polarisation field P_i given by

$$P_i = \sum_{ijk} 2\epsilon_0 \hat{a}_i d_{ijk} \hat{a}_j \hat{a}_k E_j E_k \quad (4.7)$$

where $\hat{\mathbf{a}}_j$ and $\hat{\mathbf{a}}_k$ are the unit vectors of \mathbf{E}_j and \mathbf{E}_k . The effective non-linear coefficient is given by the projection of the polarisation field onto the phasematched SHG polarisation eigenvector $\hat{\mathbf{a}}_i$,

$$d_{\text{eff}} = \sum_{ijk} \hat{a}_i d_{ijk} \hat{a}_j \hat{a}_k. \quad (4.8)$$

Since exchange of E_j and E_k has no physical meaning, it follows that $d_{ijk} = d_{ikj}$, so jk can be replaced by a single symbol l according to the piezoelectric contraction and the tensor \mathbf{d}_{ijk} can be simplified to a two-dimensional 3×6 matrix \mathbf{d}_{il} , unique to each material.

Furthermore, according to Kleinman's conjecture an additional symmetry condition for SHG may be operative in materials transparent to the fundamental and second-harmonic frequencies. If the polarisation is a single-valued function of electric field, then no physical significance can be attached to the order of the field components \mathbf{E}_j and \mathbf{E}_k , \mathbf{E}_l . This condition reduces the number of independent elements of the tensor \mathbf{d}_{ijk} , and in some cases requires null values for particular elements.

The effective nonlinear coefficient d_{eff} is much smaller for Type I SHG than for Type II [121], so for efficient interactions Type II SHG is considered; non-zero values of non-linear coefficients $d_{15} = 3.7$ pm/V and $d_{24} = 1.9$ pm/V were taken from [123] for these calculations. For the phase matching angles used in the KTP crystal under investigation ($\theta = 90^\circ$, $\varphi = 37^\circ$), the value of d_{eff} at a wavelength of 1047 nm is 2.56 pm/V.

4.3.1.3 Walk-off mechanism

The propagation directions of the fundamental and the second harmonic differ by the walk-off angle ρ , which is given by [124]

$\theta(^{\circ})$	$\varphi(^{\circ})$	$\rho(^{\circ})$	$d_{\text{eff}}(\text{II})$ (pm/V)
90	37	0.425	2.56
73	90	1.6	3.53

Table 4.3: Phase matching parameters for a KTP crystal at a fundamental wavelength 1047 nm.

$$\rho = \tan^{-1} \left(\frac{n_2^2(2\omega)}{n_1^2(2\omega)} \tan \theta \right) - \theta. \quad (4.9)$$

The second harmonic walk-off reduces the second harmonic conversion efficiency, so the preferred phase matching direction should have the smallest walk-off provided that the values of d_{eff} are comparable. As shown in figure 4.4, there are two potential phase matching directions providing propagation along a principal crystal axis; key parameters are outlined in table 4.3.

Although, d_{eff} for the first phase matching direction is smaller than for the second by a factor of 1.4, the walk-off angle is reduced by almost a factor of 4 making the first direction more efficient for second harmonic generation.

4.3.1.4 Second harmonic generation bandwidth

Another important parameter for SHG is the optical bandwidth for which the frequency doubling is efficient. The intensity I of the second harmonic light is given by

$$I \propto \text{sinc}^2 \left(\frac{\Delta k L}{2} \right) \quad (4.10)$$

where L is the length of the crystal and the phase-mismatch Δk for Type II phase matching is given by

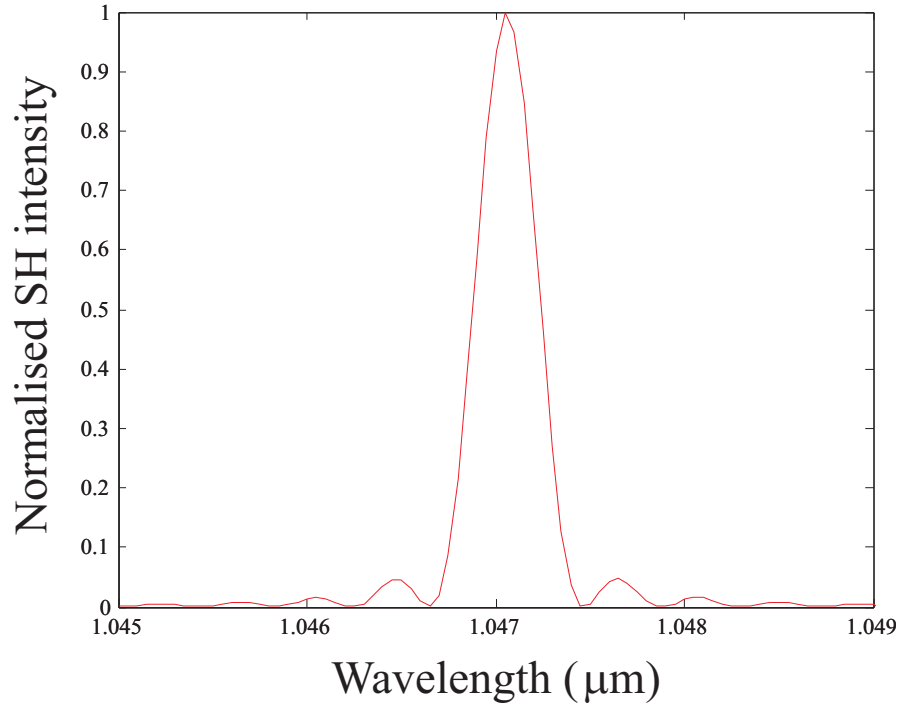


Figure 4.5: Second harmonic (SH) intensity versus wavelength for a KTP crystal of length 6 mm.

$$\Delta k = \frac{2\pi}{\lambda} (2 n_{2\omega,1} - n_{\omega,1} - n_{\omega,2}) \quad (4.11)$$

where λ is the wavelength of the fundamental light.

The normalised second harmonic intensity calculated as a function of fundamental wavelength for the original KTP crystal ($L = 6$ mm) is shown in figure 4.5. These calculations show that the full width at half maximum (FWHM) of the acceptance bandwidth is 0.4 nm for this crystal.

4.3.1.5 Calculations of second harmonic conversion efficiency

In order to calculate the second harmonic power generated when a Gaussian beam propagates through a non-linear crystal it is necessary to take into account the beam

divergence and the walk-off. The second harmonic conversion coefficient γ_{SH} is given by [125]

$$\gamma_{\text{SH}} = \frac{2\omega^2 d_{\text{eff}}^2 k_{\omega} L}{\pi n_{\omega,2}^3 \epsilon_0 c} h(B, \zeta) \quad (4.12)$$

where ω and k_{ω} are the angular frequency and wave vector of the fundamental, $n_{\omega,2}$ is the ordinary refractive index at the fundamental wavelength, ϵ_0 is the permittivity of free space, and c is the speed of light in vacuum. The Boyd-Kleinman focusing factor $h(B, \zeta)$ is a function of the walk-off parameter B defined by

$$B = \frac{1}{2} \rho \sqrt{L k_{\omega}} \quad (4.13)$$

and the focusing parameter ζ defined by

$$\zeta = \frac{L}{b}. \quad (4.14)$$

Here

$$b = k_{\omega} w_x w_y \quad (4.15)$$

is the confocal parameter of a beam with $1/e^2$ spot radii at the beam waist of w_x and w_y in the horizontal and vertical planes respectively. The function $h(B, \zeta)$ is determined numerically and plotted as a function of the focusing parameter for several values of the walk-off parameter (Fig. 2 in Ref. [126]). For the given KTP crystal with walk-off $\rho = 0.425^\circ$, the walk-off parameter is $B = 0.9$. In the case of optimal focusing ($\zeta = 1.9$) the value of the function is $h(B, \zeta) = 0.7$ (Fig. 2 in Ref. [126]) and the second harmonic conversion coefficient, defined by Eq. 4.12, is $\gamma_{\text{SH}} = 4 \times 10^{-4} \text{ W}^{-1}$.

4.3.2 Second harmonic generation in periodically poled KTP

Section 4.3.1 described birefringent phase matching in KTP and gave calculations of a number of parameters of the generated second harmonic light. In this type of phase matching the refractive indices are matched using the birefringence of an anisotropic material and in the case of optimum Gaussian focusing the second harmonic intensity grows linearly with distance in the medium. Another method of enabling continuous growth of the second harmonic wave along the device, called quasi phase matching, involves repeated inversion of the relative phase between two waves after an odd number (normally 1) of coherence lengths. This section gives the basic theory of SHG in periodically poled crystals and calculations of the main parameters of the second harmonic light generated in periodically poled KTP (PPKTP).

4.3.2.1 Quasi phase matching and poling period

The phase velocity of the wave travelling through a dispersive medium is determined by the index of refraction at the specific wavelength, which leads to a difference in phase velocities between the fundamental and second harmonic waves. Since the sign of the power flow from one wave to another is determined by the relative phase between the waves, the continuous phase slip between these waves leads to an alteration in the direction of the power flow. The distance over which the relative phase of the two waves changes by π is called the coherence length l_c , which is also the half period of the second harmonic growth and decay cycle given by [127]

$$l_c = \frac{\lambda}{4(n_{2\omega} - n_\omega)}, \quad (4.16)$$

where n_ω and $n_{2\omega}$ are the indices of refraction of the fundamental and second harmonic waves respectively, and λ is the fundamental wavelength. In a PPKTP crystal, repeated inversion of the relative phase between two waves after an odd number of coherence lengths is achieved by electric-field poling, which forms regions of

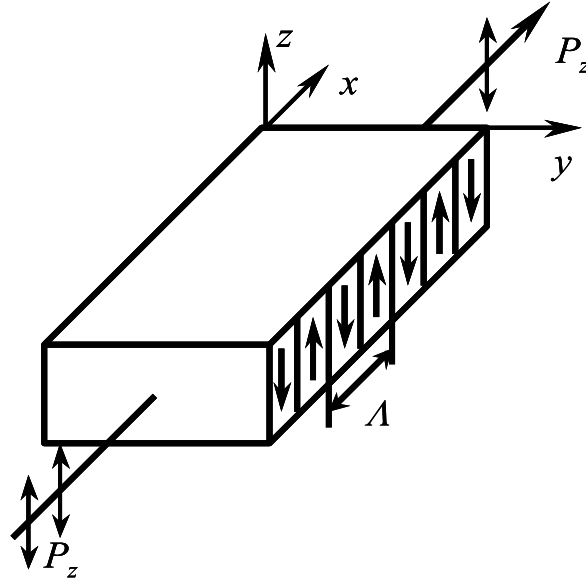


Figure 4.6: Type 0 phase matching geometry for SHG in PPKTP.

periodically-reversed polarisation domains. The greatest conversion efficiency is obtained by changing the sign of the domain every coherence length, which is called first-order quasi phase matching. The most effective SHG is obtained with Type 0 phase matching (figure 4.6) where the fundamental and the second harmonic light are both polarised along the z -axis; this configuration uses the largest non-linear coefficient $d_{33} = 14.9 \text{ pm/V}$ [128].

The poling period for first-order quasi phase matching is given by

$$\Lambda = 2l_c = \frac{\lambda}{2(n_{2\omega} - n_{\omega})}. \quad (4.17)$$

The refractive indices n_{ω} and $n_{2\omega}$ were calculated using Sellmeier equation 4.5 at $\lambda = 1.064 \text{ }\mu\text{m}$, giving a poling period of $9 \text{ }\mu\text{m}$.

4.3.2.2 Second harmonic generation bandwidth

The intensity of the second harmonic light is given by

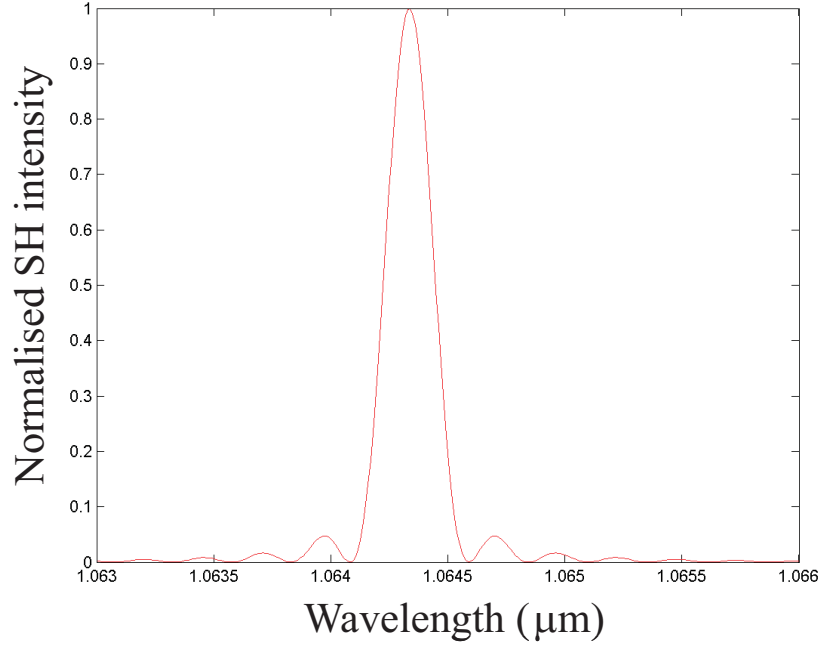


Figure 4.7: Second harmonic (SH) intensity versus wavelength for a PPKTP crystal of length 5 mm.

$$I \propto \text{sinc}^2 \left(\frac{\Delta k_Q L}{2} \right) \quad (4.18)$$

where L is the length of the crystal and Δk_Q is given by

$$\Delta k_Q = k_{2\omega} - 2k_\omega - \frac{2\pi}{\Lambda} \quad (4.19)$$

where k_ω and $k_{2\omega}$ are the wave vectors of the fundamental and second harmonic waves respectively. The wavelength dependence of the second harmonic intensity was calculated for a 5 mm long PPKTP crystal with a poling period of 9 μm . The normalised second harmonic intensity as a function of fundamental wavelength is shown in figure 4.7. This calculation shows that the FWHM of the acceptance bandwidth is 0.2 nm.

4.3.2.3 Second harmonic conversion efficiency calculations

To calculate the conversion efficiency of the PPKTP crystal, the second harmonic conversion coefficient γ_{SH} given by equation 4.12 can be used. In this case there is non-critical phase matching and so the walk-off parameter $B = 0$. For the optimum focusing ($\zeta = 2.84$) the Boyd-Kleinman focusing factor $h(B, \zeta)$ reaches its maximum value of 1.

The effective nonlinear coefficient for first order quasi phase matching doubling is given by [127]

$$d_{\text{eff}} = \frac{2}{\pi} d_{33}. \quad (4.20)$$

For the given PPKTP crystal $d_{\text{eff}} = 9.49 \text{ pm/V}$ and the second harmonic conversion coefficient is $\gamma_{\text{SH}} = 7 \times 10^{-3} \text{ W}^{-1}$.

4.3.3 Comparison of the KTP and PPKTP crystals

Sections 4.3.1 and 4.3.2 described calculations of a number of parameters for the KTP and the PPKTP crystals used in the experiments reported in this chapter. The 6 mm long KTP crystal designed for type II phase matching at a fundamental wavelength of 1047 nm was compared to the 5-mm long uncoated PPKTP crystal phase matched for Type 0 [$e + e \rightarrow e$] frequency doubling at 1064 nm (a poling period of $9 \mu\text{m}$). These calculations are summarised in table 4.4. One can see the advantage of the quasi phase matching mechanism used in the PPKTP crystal over the birefringent phase matching in the KTP crystal. The larger effective nonlinear coefficient and zero walk-off of the PPKTP crystal result in 18 times higher conversion efficiency; however the acceptance bandwidth of the PPKTP crystal is 2 times smaller than for the KTP crystal.

	$\rho, ^\circ$	$d_{\text{eff}}(\text{II}), \text{ pm/V}$	FWHM, nm	γ_{SH}
KTP	0.425	2.56	0.4	7×10^{-3}
PPKTP	0	9.49	0.2	4×10^{-4}

Table 4.4: Comparison between parameters of the KTP and PPKTP crystals used for second harmonic generation.

4.3.4 Signal to noise ratio calculations

The signal to noise ratio of a beat signal is defined as the ratio of the average electrical signal power to the total noise power (σ^2) in a given bandwidth

$$\text{SNR} = \frac{\text{average signal power}}{\text{noise power}} = \frac{I_p^2}{\sigma^2} \quad (4.21)$$

considering the fact that electrical power varies as the square of the electrical current I_p [129].

A photodetector converts incident optical power P_{in} into electrical current I_p as

$$I_p = RP_{\text{in}} \quad (4.22)$$

where R is the responsivity of the photodetector.

The average optical signal power in the beat between the fundamental and frequency doubled green pulses can be calculated as

$$P_{\text{signal}} = \sum_m \sqrt{P_{\text{SH}}^m P_{\text{F}}^m}, \quad (4.23)$$

where P_{SH}^m and P_{F}^m are the power per comb mode in the second harmonic and the fundamental green light respectively given by

$$P_F^m = \frac{P_F^{\text{total}}}{N_F} \quad (4.24)$$

and

$$P_{\text{SH}}^m = \frac{P_{\text{SH}}^{\text{total}}}{N_{\text{SH}}} \quad (4.25)$$

where P_F^{total} and $P_{\text{SH}}^{\text{total}}$ are the total power and N_F and N_{SH} are the number of contributing modes in the fundamental green light and the second harmonic respectively. In both cases the number of contributing modes is given by

$$N = \frac{|\Delta f|}{f_{\text{rep}}} = c \frac{|\Delta \lambda|}{\lambda^2} \frac{1}{f_{\text{rep}}}, \quad (4.26)$$

where Δf and $\Delta \lambda$ are the signal bandwidths, defined by the FWHM of the interference filter ($\Delta \lambda = 3$ nm) used for the power measurements in case of the fundamental light and the acceptance bandwidth of the non-linear crystal ($\Delta \lambda_{\text{PPKTP}} = 0.2$ nm) in the case of the second harmonic; λ is the central wavelength ($\lambda = 532$ nm). For these calculations it was assumed that the power per comb mode was uniform throughout the signal bandwidth for both the fundamental light and the second harmonic.

Since $N_{\text{SH}} < N_F$

$$P_{\text{signal}} = \sum_{N_{\text{SH}}} \sqrt{P_{\text{SH}}^m P_F^m} = N_{\text{SH}} \sqrt{\frac{P_{\text{SH}}^{\text{total}}}{N_{\text{SH}}} \frac{P_F^{\text{total}}}{N_F}}, \quad (4.27)$$

or combined with Eq. 4.26

$$P_{\text{signal}} = \sqrt{\frac{|\Delta \lambda|_{\text{SH}}}{|\Delta \lambda|_F} P_{\text{SH}}^{\text{total}} P_F^{\text{total}}}, \quad (4.28)$$

Equation 4.22 assumes that the optical-electrical conversion is noise free, but this is not true even for a perfect photodetector and a constant power of the incident optical

signal. Two fundamental noise mechanisms, thermal noise and shot noise, produce fluctuations of the photodetector current.

Thermal noise is generated by random thermal movements of electrons in a resistor generating fluctuating current even in the absence of an applied voltage [129]. Thermal noise is independent of the incident optical power and therefore can be neglected in case of a strong optical signal.

Shot noise has its origins in the time-dependent fluctuations in electrical current caused by the quantisation of the electron charge and cannot be eliminated by lowering the temperature. In addition, all photodiodes generate some current, called the dark current, even in the absence of an optical signal. Therefore the total shot noise is given by

$$\sigma_s^2 = 2e(I_0 + I_d)\Delta f_{\text{det}}, \quad (4.29)$$

where e is the electron charge, I_0 is the signal photocurrent, I_d is the dark current and Δf_{det} is the detection bandwidth. The quantity σ_s is the root mean square value of the noise current induced by shot noise.

In the case of an avalanche photodiode (APD) the primary photocurrent I_0 is amplified by the avalanche effect, and so the observed signal photocurrent I_p instead of Eq. 4.22 is given by

$$I_p = M I_0 = M R P_{\text{in}} = R_{\text{APD}} P_{\text{in}}, \quad (4.30)$$

where M is the avalanche gain and R_{APD} is the APD responsivity. The primary noise is also amplified by the avalanche effect (the power gain is M^2), so neglecting the dark current I_d , the observed APD noise is

$$\sigma_s^2 = 2e\Delta f_{\text{det}} M^2 I_0 = 2e\Delta f_{\text{det}} M I_p. \quad (4.31)$$

The optical noise power is given by

$$P_{\text{noise}} = P_{\text{SH}}^{\text{total}} + P_{\text{F}}^{\text{total}} \quad (4.32)$$

so the APD shot noise is given by

$$\sigma_s^2 = 2eR_{\text{APD}}\Delta f_{\text{det}}M(P_{\text{SH}}^{\text{total}} + P_{\text{F}}^{\text{total}}) \quad (4.33)$$

and the SNR in the f_0 beat can be calculated as

$$\text{SNR} = \frac{I_p^2}{\sigma_s^2} = \frac{R_{\text{APD}}}{2e\Delta f_{\text{det}}M} \frac{\Delta\lambda_{\text{SH}}}{\Delta\lambda_{\text{F}}} \frac{P_{\text{SH}}^{\text{total}} P_{\text{F}}^{\text{total}}}{P_{\text{SH}}^{\text{total}} + P_{\text{F}}^{\text{total}}}. \quad (4.34)$$

For the given silicon APD detector used (PerkinElmer C30902E [130]) $R_{\text{APD}} = 30 \text{ A/W}$ at 532 nm and $M = 150$, while $\Delta f_{\text{det}} = 250 \text{ kHz}$ is given by the resolution bandwidth of the spectrum analyser used in this experiment. The total power of the fundamental green light ($P_{\text{F}} = 0.7 \text{ }\mu\text{W}$) and the second harmonic generated using the PPKTP crystal ($P_{\text{SH}}^{\text{PPKTP}} = 3 \text{ }\mu\text{W}$) were measured immediately in front of the detector, where the two beams have the same polarisation, and the SNR calculated using Eq. 4.34 was 49.7 dB. Note that the power measurements for these calculations were made for the current f -to- $2f$ self referencing setup described later in this chapter (Fig. 4.22); the measured SNR in this configuration was 50 dB in 250 kHz bandwidth. An experimental comparison of the SNR values in the f_0 beat was also performed for the original f -to- $2f$ self referencing setup based on a Mach-Zehnder interferometer. In the case where a KTP crystal was used for frequency doubling the measured SNR was 30 dB in 250 kHz bandwidth. After the non-linear crystal was replaced by PPKTP the SNR was increased to 40 dB. This improvement allowed the tracking oscillator previously used on the f_0 beat to be eliminated.

4.4 Group velocity dispersion assessment

One of the requirements for detection of the carrier envelope offset frequency beat f_0 is temporal overlap of the fundamental and frequency doubled green pulses at the detector. There are several sources of group velocity dispersion in the self-referencing system resulting in a delay between the infrared and green parts of the supercontinuum which in turn introduces a delay between the fundamental and frequency doubled green pulses.

One of the contributing elements is lenses, providing a delay to the green spectral component relative to the infrared. Calculations using manufacturer's data for BK7 glass [131] give a delay of 0.9 ps per 1 cm of glass. The other sources of group velocity dispersion are the microstructure fibre and the frequency doubling crystal, which are described in detail in sections 4.4.1 and 4.4.2 respectively.

4.4.1 Microstructure fibre

To estimate the group delay difference between laser pulses centred at 532 nm and 1064 nm at the output of the microstructure fibre the dispersion curve shown in figure 4.8 was used. Although the input light has to travel some distance through the microstructure fibre before the generated supercontinuum contains both 532 nm and 1064 nm wavelength components, in order to estimate the maximum delay between these wavelengths at the fibre output, it was assumed that both wavelengths were present at the fibre input. This assumption gives a good estimate as the measurements of the group delay for this type of fibre reported in [132] suggest that the spectrum is broadened within the first 1.5 cm of the fibre.

The dispersion curve shown in figure 4.8 was approximated with a cubic function $D(\lambda)$

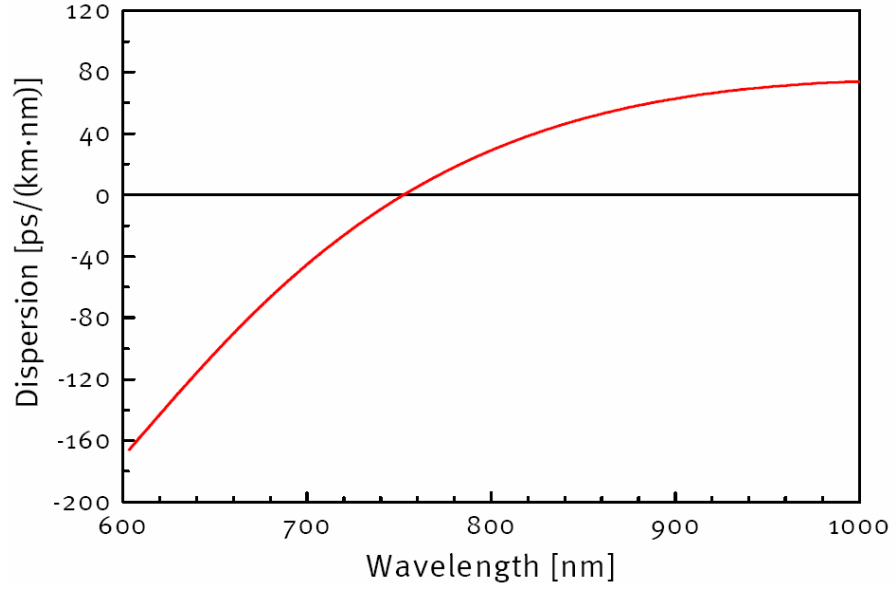


Figure 4.8: Typical measured dispersion of NL-PM-750 nonlinear photonic crystal fibre [Picture taken from Crystal Fibre data sheet].

$$D(\lambda) = B_0 + B_1\lambda + B_2\lambda^2 + B_3\lambda^3 \quad (4.35)$$

where the coefficients B_i are given in Table 4.5.

The delay Δt between laser pulses centred at 1064 nm and 532 nm at the fibre output is given by

$$\Delta t = L \int_{532}^{1064} D(\lambda) d\lambda \quad (4.36)$$

where L is the length of the microstructure fibre. For the 20 cm long microstructure

B_0	B_1	B_2	B_3
-3.11×10^3	9.17	-8.83×10^{-3}	2.85×10^{-6}

Table 4.5: Coefficients for the polynomial curve fit $D(\lambda)$ of the dispersion map shown in figure 4.8.

fibre $\Delta t = -2.4$ ps, therefore the pulses centred at 1064 nm appear at the fibre output 2.4 ps sooner than pulses centred at 532 nm. This number represents the maximum possible relative delay between the infrared and the green parts of the supercontinuum introduced by the microstructure fibre and is in good agreement with the range of delays from 0.5 to 2.5 ps reported in [132].

4.4.2 Non-linear crystal

For calculations of the maximum relative delay between the infrared and the green parts of the spectrum introduced by the frequency doubling crystal it was assumed that the frequency doubling takes place in the middle of the crystal.

The group velocity of the light inside the PPKTP crystal is given by

$$v_g = \frac{c}{n - \lambda_0 \frac{dn}{d\lambda_0}}, \quad (4.37)$$

where the refractive index n is calculated using the Sellmeier equation 4.5 and

$$\frac{dn}{d\lambda_0} = -\frac{\lambda_0}{n} \left(\frac{B}{(\lambda_0^2 - C)^2} + D \right). \quad (4.38)$$

The relative delay between the infrared and the green parts of the spectrum can be calculated as

$$\Delta t = \frac{L}{v_g^{1064}} - \frac{L}{v_g^{532}}, \quad (4.39)$$

where L is the length traveled by the infrared light before it has been frequency doubled and v_g^{1064} and v_g^{532} are the group velocities of light at wavelengths of 1064 nm and 532 nm respectively.

Assuming that the frequency doubling occurs in the middle of the crystal, in the case of the 5 mm long crystal used in the NPL frequency comb, infrared light travels a distance $L = 2.5$ mm before frequency doubling, leading to a relative delay between the fundamental and frequency doubled green light of $\Delta t = 1.3$ ps. Therefore, the estimate of the total group delay between the light at wavelengths of 1064 nm and 532 nm after passing through approximately 1.5 cm of BK7 glass, microstructure fibre and the PPKTP crystal is 5 ps.

4.5 Dispersion compensation methods used in self-referencing schemes

Section 4.4 has given an estimate of the relative delay between the short-wavelength and the long wavelength parts of the spectrum produced by the different components of the system. In order to obtain a beat between two pulses they need to be spatially and temporally overlapped, therefore the delay between the fundamental and the frequency doubled green pulses needs to be compensated before detection. The measurements of the peak power in the f_0 beat as a function of the relative delay showed that 3 dB power reduction corresponds to a delay of 0.3 ps in one direction and 0.8 ps in the opposite direction. Similar measurements reported in [132] showed that detuning of the delay by 0.2 ps resulted in a decrease of the SNR by 3 dB.

This section describes different dispersion compensation methods that have previously been used in self-referencing schemes and discusses their limitations.

4.5.1 Methods based on spectral separation

The most commonly used arrangement for dispersion compensation in self-referencing schemes employs a Mach-Zehnder (MZ) interferometer with an adjustable delay line in one of the arms [49] as shown in figure 4.9a. In this configuration a dichroic beam

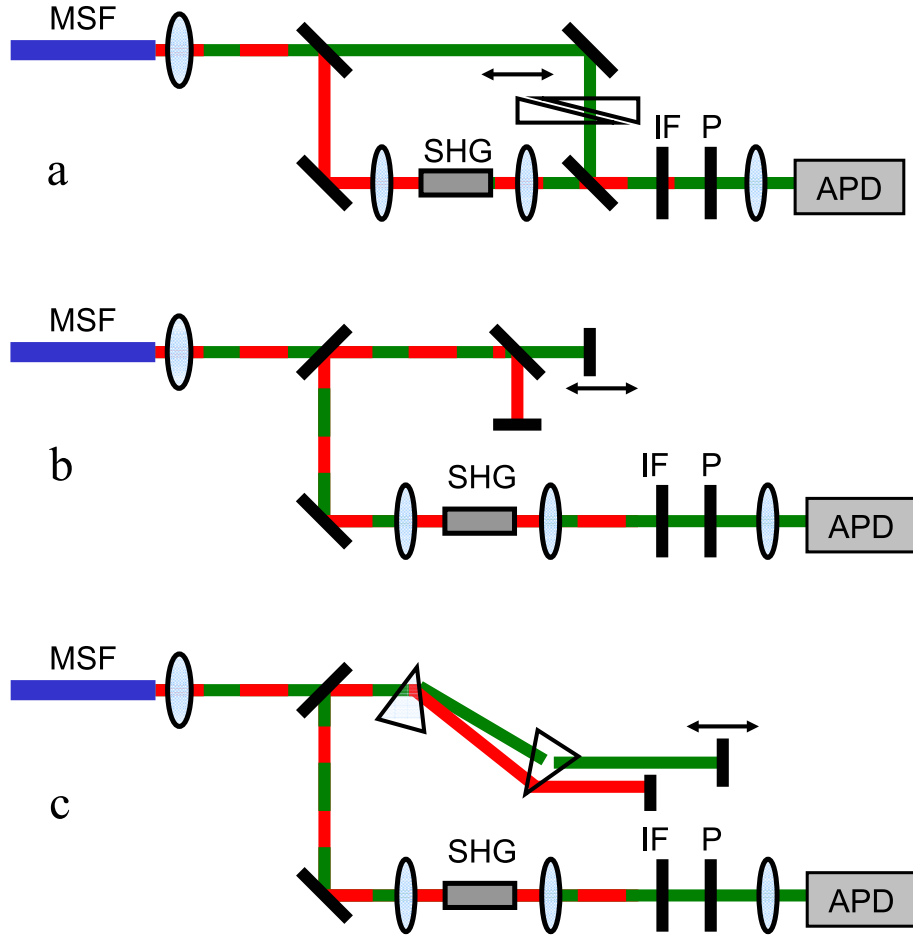


Figure 4.9: Schematic diagram of self-referencing setups based on (a) a Mach-Zehnder interferometer (b) a Michelson interferometer (c) a prism-based interferometer for dispersion compensation (MSF – microstructured fibre; SHG – second harmonic generation; IF – interference filter; P – polariser; APD – avalanche photodiode).

splitter spectrally separates the comb between the two arms of the interferometer. The long-wavelength part of the spectrum is frequency doubled in a single pass through a non-linear crystal and recombined with the short-wavelength part. To ensure temporal coincidence of the frequency doubled and short-wavelength pulses a variable delay line is fitted in the short-wavelength beam path. The main disadvantage of this topology is the long non-common optical path travelled by each beam, as acoustic noise, air currents and thermal drift induce a random phase shift between the interfering beams and the phase error of the interferometer is transferred through the stabilization loop to a change of the carrier envelope phase of the pulses produced by the laser [133].

These problems can be reduced to some extent by using a Michelson interferometer [56] (figure 4.9b). In this case the group delay between the short-wavelength and the long-wavelength pulses is compensated at the output of the microstructure fibre. The output light is launched into the interferometer with one fixed and one variable length arm. When the light is recombined at the output of the interferometer all spectral components propagate together through the non-linear crystal, where the long-wavelength part gets frequency doubled while the rest of the spectrum emerges unchanged. The length of the variable arm of the interferometer is adjusted to achieve zero delay between the short-wavelength and the frequency doubled long-wavelength pulses at the output of the crystal. This configuration provides considerably shorter non-common paths compared to the MZ arrangement, and therefore provides increased immunity to laboratory noise.

Another way of compensating for the group delay dispersion introduced by the microstructure fibre and other components as discussed in the previous section, is to use a prism-based interferometer (figure 4.9c). This scheme uses a pair of prisms to spatially separate the different spectral components, and the infrared and visible parts of the supercontinuum are separately retroreflected using a split mirror. This configuration was first reported in [134, 135]. A detailed comparison of the noise performance of a prism-based interferometer and a MZ interferometer was presented by Grebing et al [136]. The results proved that the system with the shorter non-common path ex-

hibits increased immunity to acoustic noise and air currents; however the fundamental problem of noise originating from non-common optics in systems based on separation of different spectral components of the supercontinuum remains. The solution to this problem is to use a common-path interferometer.

4.5.2 Dispersion compensation with a common-path interferometer

The advantage of a common-path interferometer is that the difference in optical path lengths for different spectral components is achieved using the wavelength dependence of the group velocity whilst keeping the physical path the same. This is easy to realise in 1.5 μm fibre-laser based combs [137], where both positive and negative group-delay dispersion occurs at the wavelengths of interest in different types of fibre. Therefore the group-delay between the high-frequency and the low-frequency components of the octave-spanning spectrum can be compensated by selection of appropriate fibre types and lengths.

This solution is harder to realise for Ti:Sapphire-based combs since such fibres are not commercially available for non-telecommunication wavelengths. There are several examples of group velocity dispersion compensation in Ti:sapphire laser based combs having been realised without spectral separation. A pair of ultrabroadband chirped mirrors with tailored dispersion was used in a monolithic f_0 stabilization scheme as described in [138, 139]. The Ti:Sapphire lasers used in these works produce an octave-spanning spectrum without spectral broadening in a microstructure fibre, so a delay line based on chirped mirrors is sufficient to compensate the group velocity delay produced by the laser. Furthermore, the delay produced by a pair of chirped mirrors is not variable.

A polarisation-dependent delay between the fundamental and frequency-doubled green pulses propagating in a PPKTP crystal with Type I phase matching $[\text{o} + \text{o} \rightarrow \text{e}]$ was

used for delay compensation in [140]. However, no explanation as to how the arbitrary delay introduced by a microstructure fibre was compensated is offered in the publication.

A method described in [132] made use of the difference in the group velocities of orthogonally polarised light in birefringent materials. This scheme was based on a common-path interferometer with a calcite Babinet-Soleil compensator designed specially to provide a variable delay between the fundamental and the second harmonic of the infrared parts of the supercontinuum.

The above method was based on the same idea of using birefringent material as the NPL all-common-path self-referencing scheme described below and reported in [10]. The two systems were developed independently and in parallel; however the system constructed at NPL has the advantage that it is made from off-the-shelf optical components.

4.6 Wollaston prism-based self referencing setup

This section describes the geometry and principle of operation of a Wollaston prism together with calculations and the experimental characterisation of the delay between two output beams used in the novel self-referencing scheme. Finally, a detailed description of the optical arrangement for the self-referencing scheme is presented.

4.6.1 Wollaston prism principles of operation

A schematic diagram of a Wollaston prism is shown in figure 4.10. A Wollaston prism consists of two triangular calcite prisms cemented together, with their optical axes perpendicular to each other and to the direction of propagation of the incident light. Once the light enters the prism it is refracted into two orthogonally polarised co-directional rays: the ordinary ray (o-ray) and the extraordinary ray (e-ray). At the

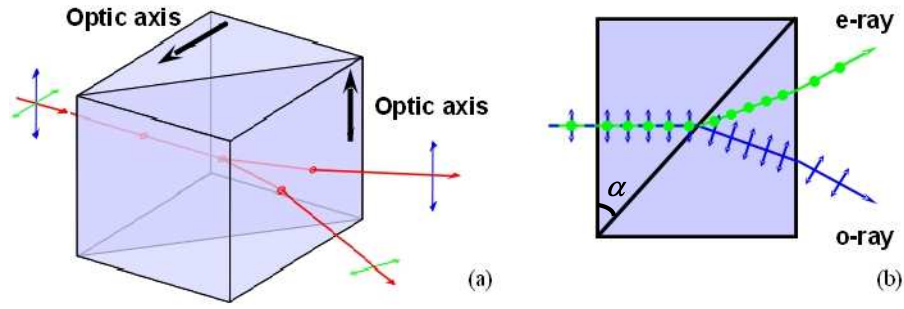


Figure 4.10: Schematic diagram of a Wollaston prism and direction of the input and output beams (a); schematic of polarisations and the propagation direction of ordinary and extraordinary rays inside a Wollaston prism (b).

boundary surface the extraordinary ray in the first prism becomes an ordinary ray in the second prism and the ordinary ray becomes an extraordinary ray. In addition, as a result of the change of the effective refractive index both rays are bent away from the normal in opposite directions. The beams diverge from the prism with the angle of divergence determined by the wedge angle (angle α in Fig. 4.10) of the prism and the wavelength of the light. The relative delay between the two orthogonally polarised beams, achieved as a consequence of their different optical path lengths within the prism, depends on the position of the input beam across the aperture of the prism [141].

4.6.2 Relative delay between the two output beams

A schematic diagram of dispersion compensation using a pair of Wollaston prisms is shown in figure 4.11. Two orthogonally polarised beams are separated at the point S1 and recombined at the point S2.

The relative delay between the two orthogonally polarised output beams was calculated as a function of the distance between the input beam and the prism centre. Figure 4.12 shows a schematic diagram of the light propagation through the Wollaston prism for the ordinary ray (a) and the extraordinary ray (b) in the first prism.

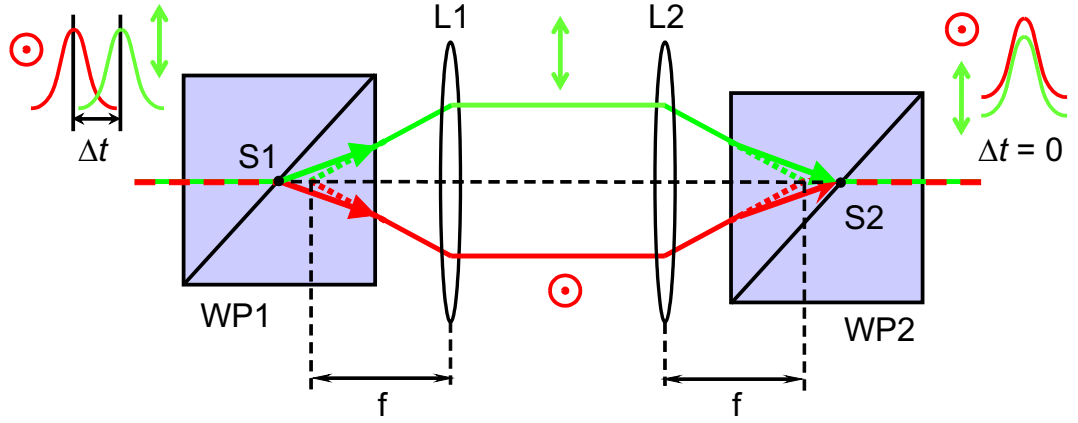


Figure 4.11: Schematic diagram of dispersion compensation using a pair of Wollaston prisms. WP1 and WP2 – Wollaston prisms, L1 and L2 – lenses with the focal length f , S1 – point of separation of the beams, S2 – point of recombination of the beams.

The total path inside the prism is a sum of the paths in the first prism (L_1) and the second prism (L_2) calculated using the prism geometry as

$$L_1 = A \left(\frac{1}{2} - \frac{O}{B} \right) \quad (4.40)$$

and

$$L_2 = \frac{A}{\cos \gamma} \left(\frac{O}{B} + \frac{1}{2} \right). \quad (4.41)$$

Angle γ was calculated as the sum or difference between angles α and β as shown in figure 4.13, where

$$\alpha = \sin^{-1} \left(\frac{A}{\sqrt{A^2 + B^2}} \right) \quad (4.42)$$

and angle β was calculated using Snell's law:

$$n_1 \sin \alpha = n_2 \sin \beta \quad (4.43)$$

where $n_1 = n_o$ and $n_2 = n_e$ for the ordinary ray in the first prism (fig. 4.13a) and

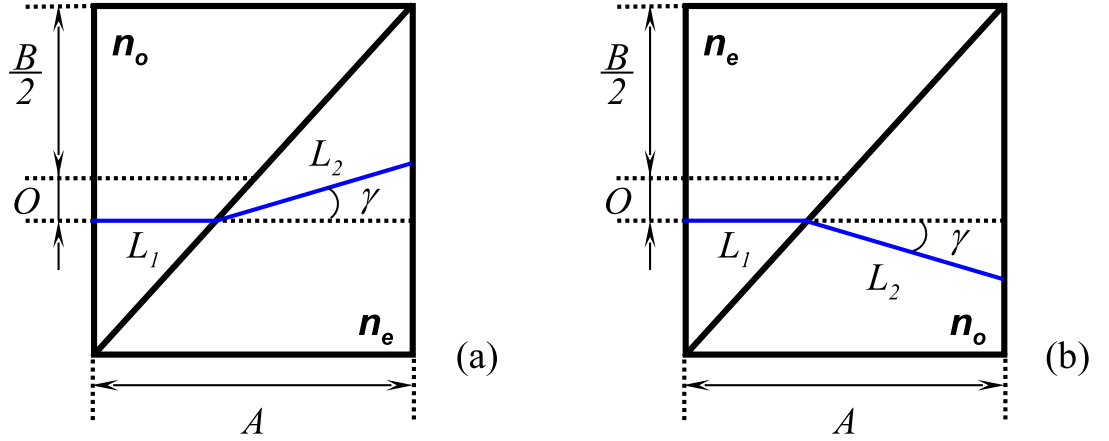


Figure 4.12: Schematic diagram of the light propagation through a Wollaston prism. The ordinary ray in the first prism becomes an extraordinary ray in the second at the boundary surface (a) and the extraordinary ray in the first prism becomes an ordinary ray in the second prism (b); A , B and O are the length, the width and the offset from the centre of the prism respectively.

$n_1 = n_e$ and $n_2 = n_o$ for the extraordinary ray in the first prism (fig. 4.13b).

The refractive indices were calculated using the Sellmeier equation for calcite

$$n^2 = A + \frac{B}{\lambda_0^2 - C} - D\lambda_0^2. \quad (4.44)$$

The indexes A , B , C , and D are given in table 4.6 for both ordinary and extraordinary rays [142]; λ_0 is the wavelength in microns.

The light propagates through the Wollaston prism with group velocity (v_g) given by

	A	B	$C/\mu\text{m}^2$	$D/\mu\text{m}^{-2}$
n_o	2.69705	0.0192064	0.0182	0.0151624
n_e	2.18438	0.0087309	0.01018	0.0024411

Table 4.6: Sellmeier equation coefficients for calcite.

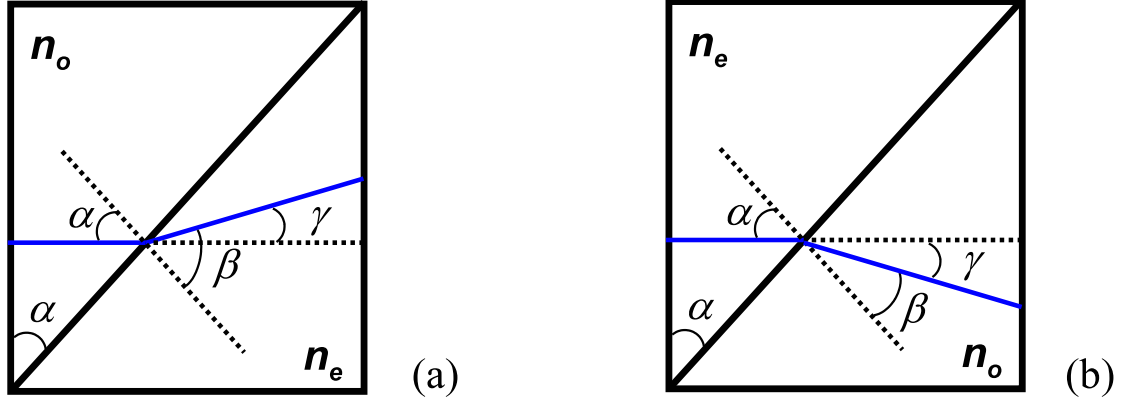


Figure 4.13: Refraction of the light at the boundary surface of the Wollaston prism for the ordinary ray in the first prism (a) and the extraordinary ray in the first prism (b).

$$v_g = \frac{c}{n - \lambda_0 \frac{dn}{d\lambda_0}}, \quad (4.45)$$

where

$$\frac{dn}{d\lambda_0} = -\frac{\lambda_0}{n} \left(\frac{B}{(\lambda_0^2 - C)^2} + D \right). \quad (4.46)$$

The group velocity inside the Wollaston prism was calculated for ordinary (v_g^o) and extraordinary (v_g^e) rays separately and the values obtained were then used to calculate the time taken by the first ray to propagate through the Wollaston prism as

$$t_1 = \frac{L_1(O)}{v_g^o} + \frac{L_2(O)}{v_g^e}, \quad (4.47)$$

and the time taken by the second ray to propagate through the Wollaston prism as

$$t_2 = \frac{L_1(O)}{v_g^e} + \frac{L_2(O)}{v_g^o}. \quad (4.48)$$

Finally, the relative delay between two output beams was calculated as

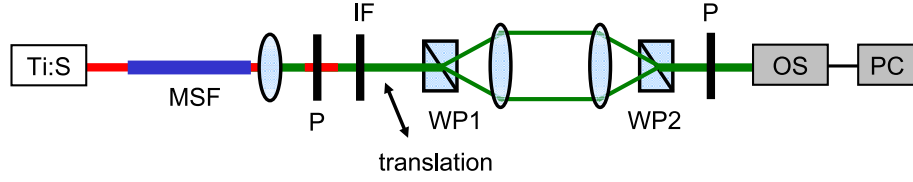


Figure 4.14: Schematic diagram of the setup used to measure the relative delay between orthogonally polarised pulses introduced by the pair of Wollaston prisms as a function of the position of the first prism. (Ti:S – Ti:Sapphire laser, MSF – microstructure fibre, P – polariser, IF – interference filter, WP1 and WP2 – Wollaston prisms, OS – optical spectrometer, PC – computer).

$$\Delta t(O) = t_1(O) - t_2(O). \quad (4.49)$$

Experimental characterisation of the delay introduced by the pair of Wollaston prisms was performed using coherent spectral interferometry [143]. Figure 4.14 shows the setup used for this experiment.

The output of the mode-locked Ti:Sapphire laser was coupled into a 20-cm long microstructure fibre to obtain a green spectral component which was selected from the generated super-continuum using a 10 nm bandwidth interference filter (IF) centred at 532 nm. The polariser P set to 45° from vertical ensured that both vertical and horizontal polarisation components were present at the input of the first Wollaston prism. The input light was separated into two orthogonally polarised beams by the first Wollaston prism and these were recombined by the second. The position of the first Wollaston prism relative to the input beam was controlled using a micrometer-driven translation stage. The optical spectrum at the output of the second polariser P was measured using an Ocean Optics HR 4000 spectrometer and the interference fringes were recorded using a PC. The fringe spacing corresponding to different positions of the first Wollaston prism was used to calculate the relative delay between the two orthogonally polarised output beams (Δt) as

$$\Delta t = \frac{\lambda^2}{cD}, \quad (4.50)$$

where λ is the wavelength, c is the speed of light and D is the fringe spacing.

Figure 4.15 shows examples of interference spectra with fringe spacings of 1 nm (a) and 0.5 nm (b) corresponding to delays of 0.9 ps and 1.9 ps respectively.

The theoretical values of the relative delay between the two beams obtained from equation 4.49 and values calculated from the results of the coherent spectral interferometry using equation 4.50 are plotted in figure 4.16 as a function of the offset from the centre of the prism along the boundary surface. The estimate of the group-delay between fundamental and second harmonic green pulses calculated in Section 4.4 was 5 ps, therefore the measured range of delays is sufficient to compensate the expected delay in our system.

4.6.3 Self-referencing setup description

The optical design of the Wollaston prism based self-referencing setup is shown in figure 4.17. A polariser at the output of the microstructure fibre ensured a horizontal polarisation at all wavelengths in the spectrum. A half-wave plate at 1064 nm rotated the polarisation of the infrared light by 90° to meet the phase-matching conditions of the PPKTP frequency-doubling crystal. An interference filter centred at 532 nm and with a 3 nm bandwidth was used for spectral filtering. The PPKTP phase matching geometry was such that the fundamental and frequency doubled light have the same polarisation, thus the fundamental and frequency-doubled green pulses at the output of the crystal propagated collinearly but were orthogonally polarised. By adjusting the positions of the Wollaston prisms WP1 and WP2, the orthogonally-polarised fundamental and frequency-doubled 532 nm pulses separated by WP1 and recombined by WP2 can be temporally overlapped at the detector. Note that since the effective optical point of recombination lies within the first triangular part of the

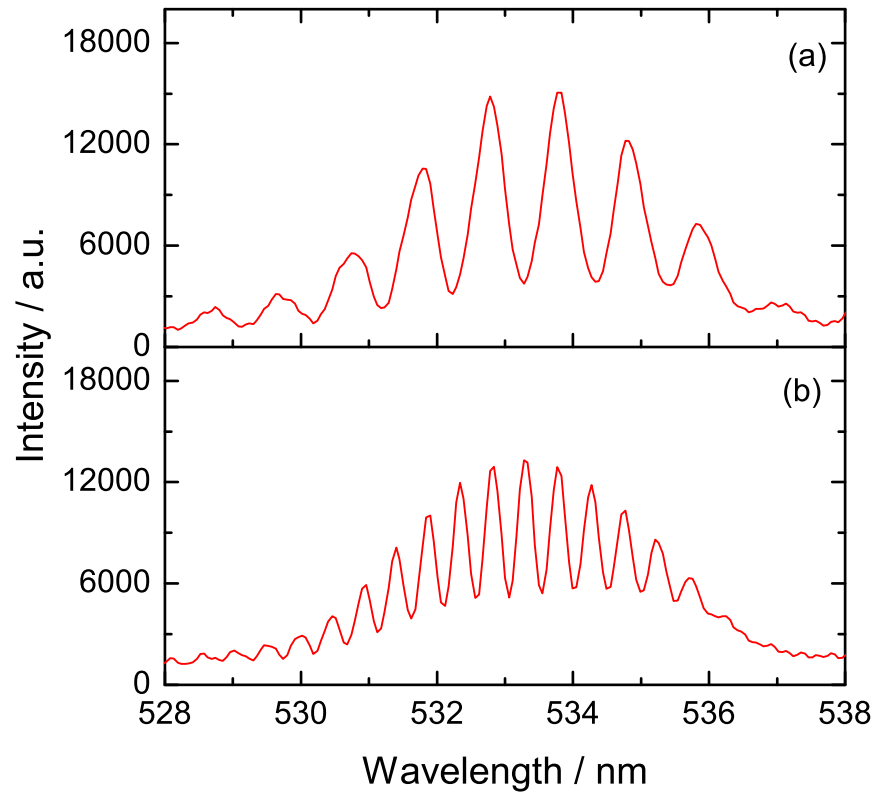


Figure 4.15: Examples of optical spectrum of the interference between two polarisation states corresponding to fringe spacings of 1 nm (a) and 0.5 nm (b).

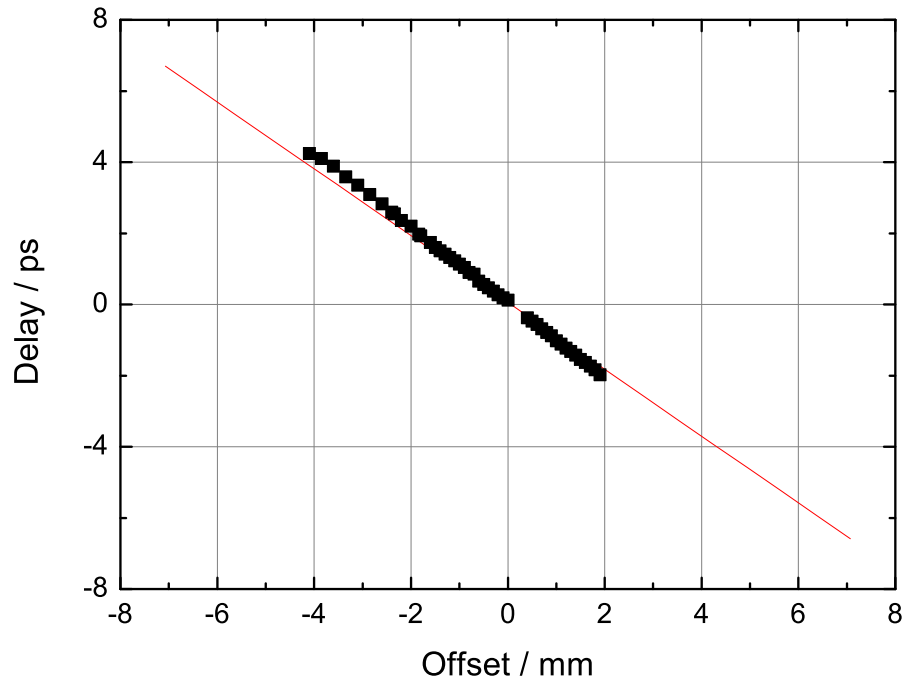


Figure 4.16: Relative delay between the two orthogonally polarised beams at the output of the Wollaston prism. The red line shows the theoretical calculations and the black squares represent values calculated from the coherent spectral interferometry measurements.

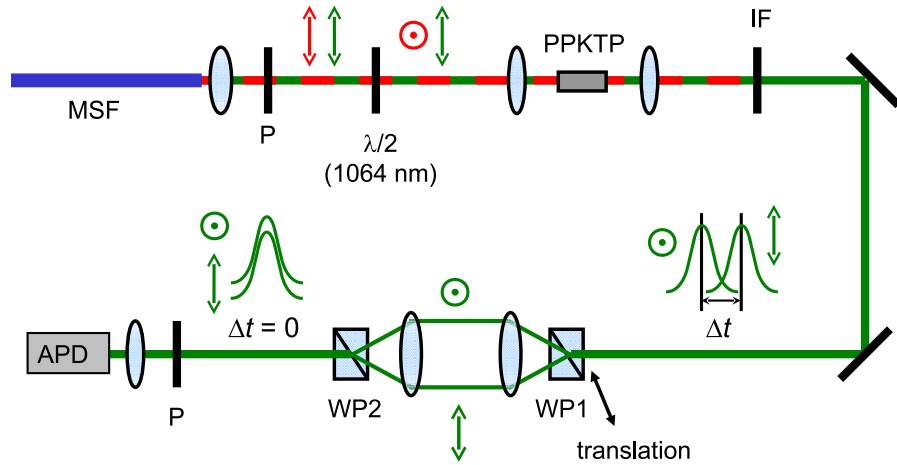


Figure 4.17: Schematic of the self-referencing interferometer using a pair of Wollaston prisms for dispersion compensation. (MSF – microstructure fibre emitting an octave-spanning super-continuum; P – polariser; $\lambda/2$ – 1064 nm half wave plate; IF – 532 nm interference filter (FWHM = 3 nm); WP1, WP2 – Wollaston prisms; APD – avalanche photodiode).

Wollaston prism, the translation axis does not coincide with the boundary surface. The f_0 beat frequency was detected using an avalanche photodiode (APD), with a rotatable polariser in front of the detector being used to optimize the SNR in the beat.

4.7 Experimental characterisation of novel self-referencing scheme

In order to assess the noise performance of the new self-referencing system, it was compared to the performance of a Michelson interferometer based self-referencing scheme. For an objective evaluation of the phase noise performance, an out-of-loop measurement scheme consisting of two independent f -to- $2f$ self-referencing systems, one for generating the signal for the feedback loop and the second for making independent

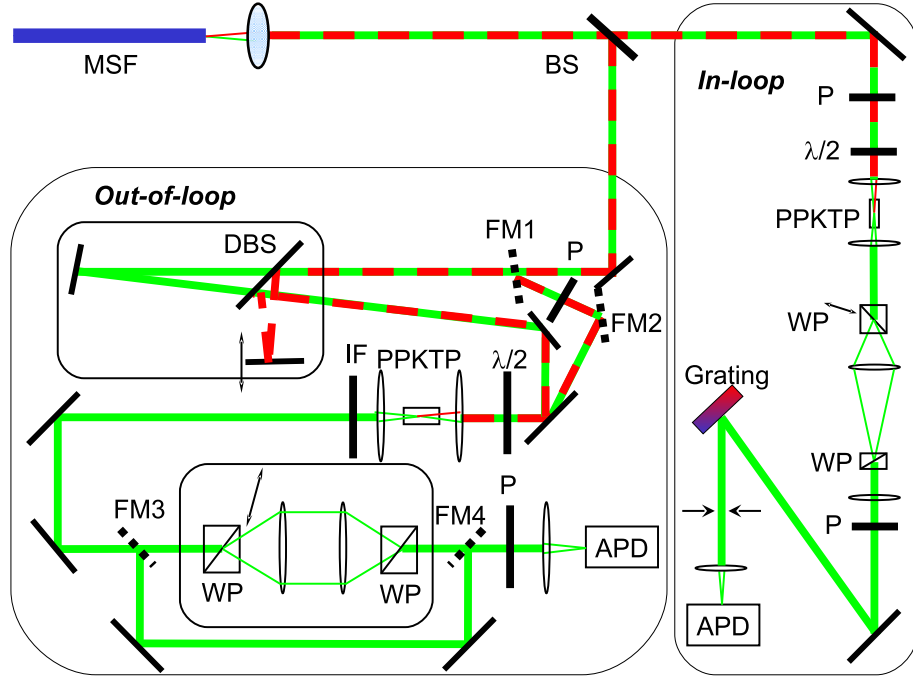


Figure 4.18: Optical arrangement for comparison of the noise performance of Wollaston prism based and Michelson interferometer based f -to- $2f$ self-referencing setups. (MSF – microstructure fibre; BS – beam splitter; DBS – dichroic BS; $\lambda/2$ – half wave plate at 1064 nm; P – polariser; IF – interference filter ($\lambda = 532$ nm; FWHM = 3 nm); WP – Wollaston prism; FM – flipper mirror; APD – avalanche photodiode).

phase-noise measurements, was used.

4.7.1 Comparison of Wollaston prisms and Michelson interferometer based schemes

The optical arrangement of the setup used for the characterisation of the phase-noise performance of the new self-referencing system is shown in figure 4.18. Since the noise performance of the Wollaston prism based self-referencing scheme was expected to be superior to that of a Michelson interferometer based system, the setup generating the error signal used to stabilize f_0 (the in-loop interferometer) was based on Wollaston prisms. The second f -to- $2f$ self-referencing system (the out-of-loop inter-

ferometer) was specifically built for independent phase-noise measurements. In this interferometer the group-delay dispersion compensation could be switched between a Wollaston prism arrangement and a Michelson interferometer using two pairs of flipper mirrors, while keeping the frequency-doubling and detection parts of the apparatus common. The non-common path length in the Michelson interferometer was approximately 10 cm. To eliminate noise contributions from the MSF the beams for the in-loop and out-of-loop interferometers were derived after the MSF by splitting the super-continuum output using a pellicle beam splitter (BS). Furthermore, in order to ensure that the air current contributions to the noise of the in-loop and the out-of-loop systems are not common-mode, they were arranged orthogonally. The measured SNR in the f_0 beat was 40 dB in the out-of-loop signal for both methods of dispersion compensation, while the in-loop setup demonstrated a SNR of 48 dB. In all measurements a 250-kHz resolution bandwidth was used and f_0 was stabilised to 30 MHz by a combination of fast and slow feedback loops as described in Section 4.2. The difference in SNR between the f_0 signals in the two interferometers is attributed to the non 50:50 BS and the difference in spectral filtering before the APD: a diffraction grating followed by an adjustable slit was employed in the in-loop setup and provided 2 dB higher SNR compared to an interference filter used in the out-of-loop setup.

Figure 4.19 shows the setup used for the noise sensitivity characterisation. The two f_0 signals generated by the APDs of the in-loop and the out-of-loop interferometers were each filtered and amplified to a power of 7 dBm and sent to a phase detector providing an output signal for the measurement system. Two separate sets of noise measurements were performed: in the time domain the phase error was recorded as a function of observation time, and in the frequency domain the power spectral density of the phase fluctuations S_ϕ was measured.

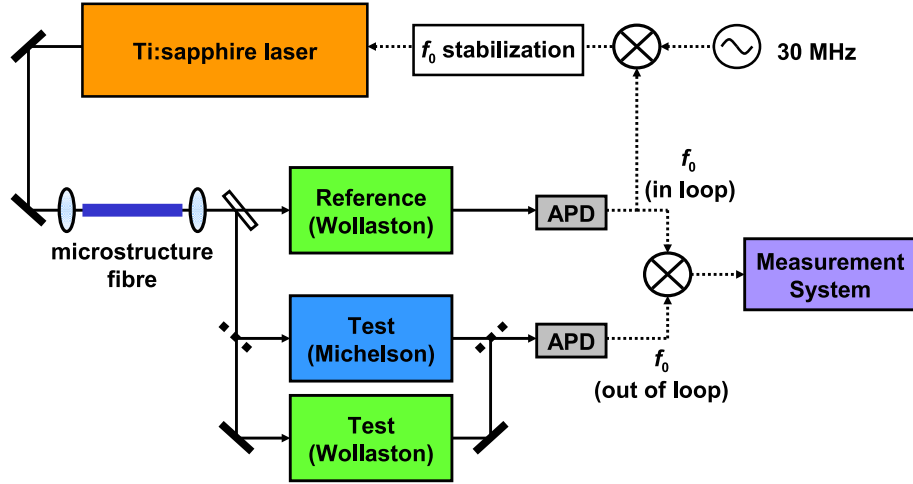


Figure 4.19: Schematic diagram of the system used to compare the noise sensitivity of the two different f -to- $2f$ self-referencing schemes.

4.7.1.1 Phase error measurements

In a first set of measurements the voltage fluctuations at the output of the phase detector were recorded in the time domain using a precision digital voltmeter and the corresponding phase error was calculated as a function of observation time. The voltmeter sampling rate was 100 Hz and a first order low-pass filter at 10 Hz was used to minimise aliasing. The results of these measurements are shown in figure 4.20.

The Wollaston prism based interferometer demonstrated significantly better short-term performance, with a root mean square (rms) phase error of 37 mrad measured for a 5 s observation time, compared with 130 mrad measured for the Michelson interferometer based scheme. The long-term performance was measured over a total observation time of 30 minutes, during which a rms phase error of 51 mrad was demonstrated by the Wollaston prism based interferometer, compared with 207 mrad error from the Michelson interferometer-based system.

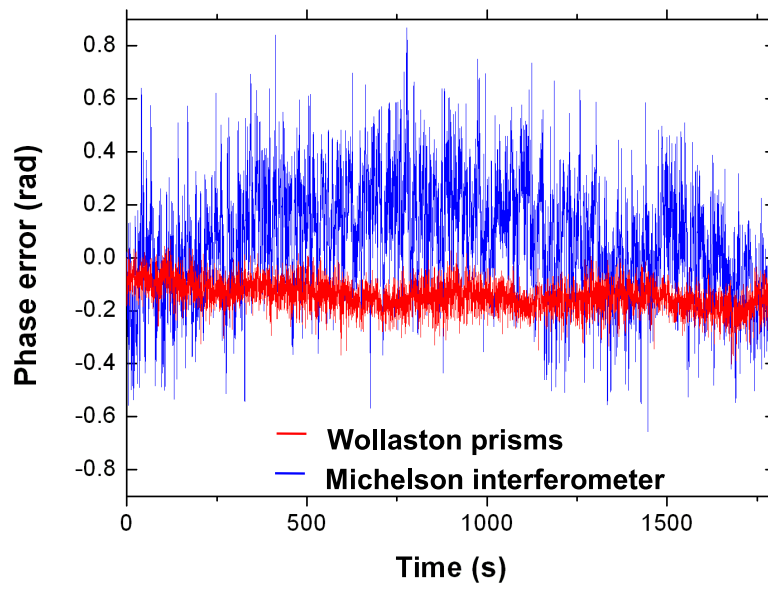


Figure 4.20: Phase error between the f_0 beat signals from the in-loop and out-of-loop interferometers as a function of observation time. The in-loop system was a Wollaston prism based interferometer in both cases while the out-of-loop system was switched between Wollaston prism and Michelson based interferometers.

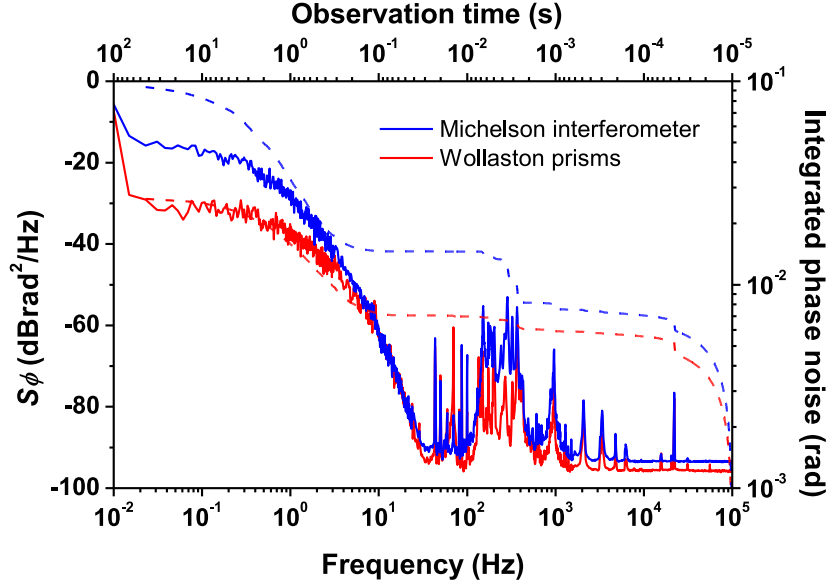


Figure 4.21: Comparison of the out-of-loop phase noise S_ϕ (solid lines) and integrated phase noise as a function of observation time (dashed lines) measured for the f_0 signals from the Wollaston prism based interferometer and Michelson interferometer.

4.7.1.2 Phase noise measurements

In a second set of measurements the power spectral density of the phase fluctuations S_ϕ was derived from the voltage fluctuations at the output of the phase detector using a Fast Fourier Transform (FFT) analyser. The accumulated phase noise was obtained by integration of S_ϕ from the inverse of the observation time to the upper limit of the FFT analyzer, which was 100 kHz. These results are presented in figure 4.21.

The noise peaks in the region from 40 to 1000 Hz can be attributed to vibrations of the optics due to acoustic noise in the laboratory. As expected, the common optical path provided by the Wollaston prism based system achieved substantial common-mode acoustic noise rejection, which was observed as a phase noise reduction of up to 15 dB compared with the Michelson interferometer-based system. The difference in the white phase noise level observed at high frequencies for the two interferometers can be explained by the different optical power levels incident on the APDs in the two

cases, which led to different shot noise levels. The sensitivity of the two interferometers to air currents can be inferred from the phase noise observed at frequencies lower than a few hertz. In this region, the Wollaston prism based scheme again demonstrated up to 15 dB improvement over the Michelson interferometer based system.

The enhanced immunity of the Wollaston prism based interferometer to acoustic noise is also apparent when comparing the integrated phase noise, where the contribution of each of the noise peaks in the phase noise spectrum can be seen as clear steps. The rms phase error accumulated in the frequency region 40 to 1000 Hz was only about 1 mrad for the Wollaston prism-based system compared to about 7 mrad for the Michelson interferometer-based system. The Michelson interferometer-based system also showed a much more pronounced increase in integrated phase noise at long observation times, reflecting its poorer immunity to air currents and thermal drift.

These measurements were obtained on an open optical table with no shielding around the interferometers. The insensitivity of the Wollaston prism based scheme to air currents was confirmed by repeating the measurements after fully shielding the apparatus, which for the Michelson interferometer based scheme reduced the phase noise at low frequencies to a level similar to that observed for the unshielded Wollaston prism scheme, but which had negligible effect on the Wollaston prism scheme.

4.7.2 Single Wollaston prism compact setup

The symmetry of the two Wollaston prism arrangement shown in figure 4.17 allowed a further simplification to be made, providing a more compact scheme. The final design of f -to- $2f$ self-referencing setup implemented on the LRR comb is shown in figure 4.22. In this arrangement the two beams exiting the Wollaston prism were directed onto a concave mirror and retro-reflected back through the Wollaston prism. The concave mirror was tilted so that the recombined output beam emerged slightly below the incident beam and was then directed onto the APD using a D-shaped mirror. The

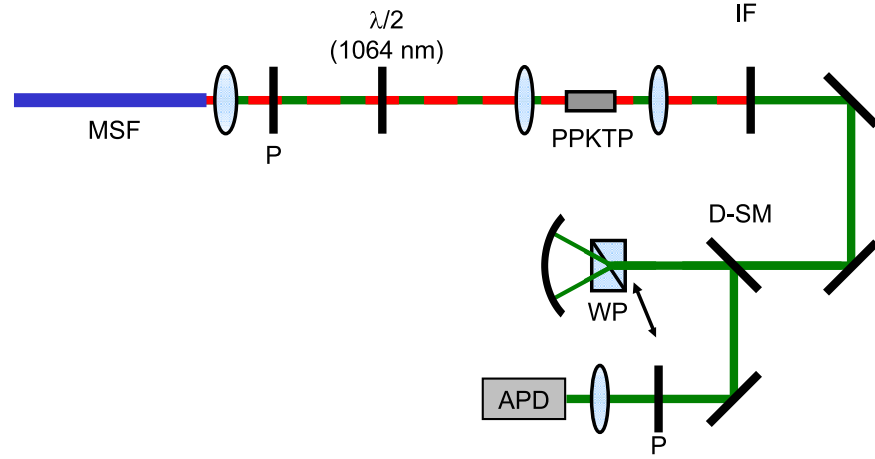


Figure 4.22: Schematic of the compact self-referencing setup based on a Wollaston prism for dispersion compensation. MSF – microstructured fibre; $\lambda/2$ – half wave plate at 1064 nm; P – polariser; IF – interference filter ($\lambda = 532$ nm; FWHM=3 nm); D-SM – D-shaped mirror.

SNR in the f_0 beat obtained in this configuration was 50 dB in a 250 kHz resolution bandwidth, 2 dB better than in the system based on a pair of Wollaston prisms.

4.8 Summary

In this chapter improvements to the original design of the LRR Ti:Sapphire laser based frequency comb have been described. The generation of both f_0 and f_b beat signals was improved by using two separate microstructure fibres for spectral broadening instead of one. This allowed supercontinuum generation conditions to be improved in different spectral regions independently and hence the SNR in both beats to be improved. The stability of the beats was further improved by replacing the cleaved microstructure fibre by connectorised fibre in both branches. An additional improvement to the stability of the f_0 beat was gained by the use of a two branch feedback loop consisting of a fast servo loop acting on an AOM in the pump laser beam in addition to the previously used slow loop acting on the cavity end mirror in the Ti:Sapphire

laser.

In section 4.3 the theory of second harmonic generation in two types of non-linear crystal was reviewed. A number of SHG parameters such as phase matching angles, effective nonlinear coefficient, walk-off angle, acceptance bandwidth and second harmonic conversion efficiency were presented for the KTP crystal used in the original self-referencing scheme. An overview of the principles of quasi phase matching was given and the acceptance bandwidth and second harmonic conversion efficiency of a PPKTP crystal calculated. After that the two crystals (KTP and PPKTP) were compared. It is also shown in this section that the use of a PPKTP crystal instead of KTP for second harmonic generation improves the measured SNR in the f_0 beat by 10 dB due to the higher conversion efficiency.

In section 4.4 group velocity dispersion was assessed separately for the microstructure fibre, the non-linear crystal and the lenses used in the self-referencing interferometer. The resulting estimate of the total delay between fundamental and frequency doubled green pulses was 5 ps. After that various methods of dispersion compensation used in self-referencing systems, including their advantages and disadvantages, were reviewed. Finally, a new f -to- $2f$ self-referencing scheme based on Wollaston prisms was described. The relative delay between two beams at the output of a Wollaston prism was assessed theoretically and experimentally, proving that this is sufficient for group velocity dispersion compensation. The main advantage of the Wollaston prism interferometer over commonly used interferometers such as Mach-Zehnder or Michelson interferometers is that it provides the same optical path for all spectral components resulting in common-mode acoustic noise rejection. It was experimentally demonstrated that the use of a Wollaston prism based interferometer results in up to 15 dB lower phase noise compared to a Michelson interferometer. Furthermore, a compact setup based on a single Wollaston prism and a concave mirror was developed, reducing the size of the self-referencing system.

Chapter 5

Sources of systematic uncertainty and instability of frequency combs

In this chapter the sources of systematic uncertainty and instability of frequency combs originating from the reference signal used for frequency measurements are investigated. Firstly, the various sources of microwave frequency producing the reference signal for the frequency combs are described. Next, the stability and accuracy of the signal produced by three frequency sources, a GPS-disciplined oscillator, a hydrogen maser and a Cs primary frequency standard, used as a reference for frequency combs are evaluated. The impact of the frequency distribution system on the stability of the most commonly used reference source, a hydrogen maser, is also investigated. Finally, the impact of temperature variations on the accuracy of the frequency signal produced by maser-referenced synthesisers is analysed.

5.1 Microwave frequency reference sources

A measured optical frequency should be related to the frequency of a caesium primary frequency standard used to realise the SI second as defined in Section 2.1.1. In order

to achieve this, the NPL frequency combs are referenced to a 10-MHz signal from a hydrogen maser frequency standard, which in turn can be calibrated using the local caesium fountain primary frequency standard NPL-CsF2 for the highest accuracy measurements. Alternatively, if lower accuracy can be tolerated, the hydrogen maser frequency can be calibrated against the international timescale UTC using data from the BIPM publication “Circular T”. An example of this second approach is detailed in Section 6.2.3.

5.1.1 Caesium primary frequency standards

Due to the definition of the SI unit of time, caesium atomic clocks are very important. These clocks use the transition between the two hyperfine levels $F = 4, m_F = 0$ and $F = 3, m_F = 0$ of the ground state of the ^{133}Cs atom as a frequency reference. The first caesium atomic clock was developed at NPL in the 1950s [144], and since then a number of different designs with improved stability and accuracy have been developed. At present, the most accurate caesium standards are realised using laser-cooled atoms in a fountain configuration (see for example [145, 146, 116]).

5.1.1.1 Principles of operation

A schematic diagram of the NPL-CsF2 caesium fountain is shown in Fig. 5.1. The setup consists of three main sections: a preparation zone, an interaction zone and a detection zone. In the preparation zone caesium atoms are collected and laser cooled to typically about $2\ \mu\text{K}$, after which they are launched vertically through an interaction region, slow down due to gravity and fall back. The interaction zone contains two microwave cavity resonators and a zone for the ballistic flight of the atoms. The first microwave resonator cavity is used to prepare the population in the desired hyperfine states in order to avoid frequency shifts caused by effects related to population in the states other than the two involved in the transition. When

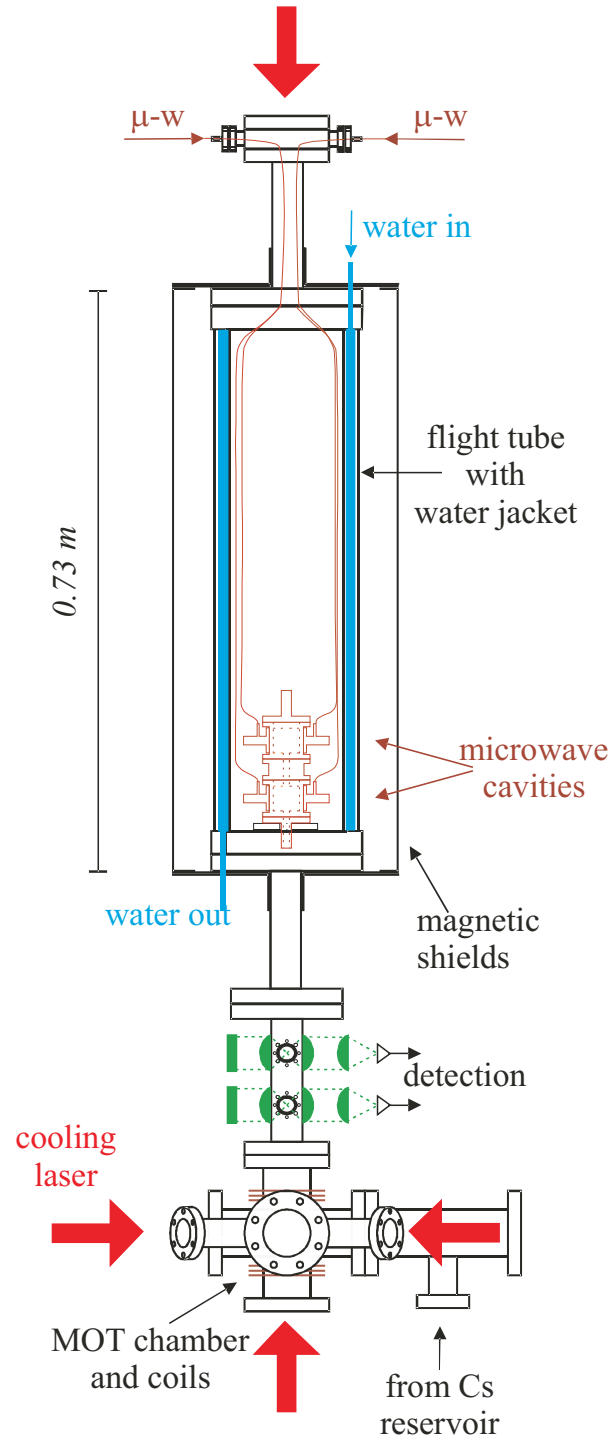


Figure 5.1: Schematic diagram of the NPL-CsF2 caesium fountain primary frequency standard described in [116] [picture courtesy of Dr Krzysztof Szymaniec].

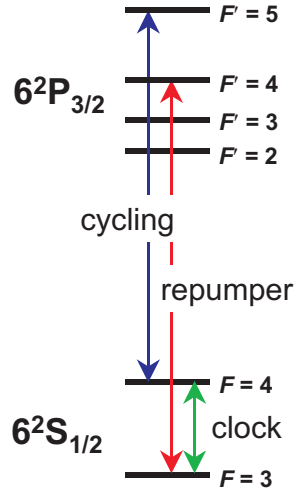


Figure 5.2: Simplified caesium energy level diagram showing the clock transition (green), and the cycling (blue) and repumper (red) transitions used in the detection process.

atoms pass through the second microwave resonator on their way up and down they experience Ramsey excitation where transitions are induced.

Ramsey interrogation or the method of separated oscillatory fields [147] is based on interrogation of the atomic transition with two phase-coherent microwave pulses of the same duration separated in time rather than by a single microwave pulse. The duration of these pulses is much smaller than the interval between them. The resulting probability of transition function is an interference pattern, called Ramsey fringes, with the linewidth of the central fringe being inversely proportional to the duration of the interval between the two microwave pulses. In atomic fountains the microwave pulses are generated in the second microwave resonator and the ballistic flight up and down the interaction zone provides the interval between the two microwave pulses experienced by the atoms.

Atoms in the $F = 4$ and $F = 3$ states are detected separately. Figure 5.2 shows a simplified caesium energy level diagram illustrating the detection process. First, the falling atoms pass through a standing-wave laser field tuned to the $F = 4 \rightarrow F' = 5$

cycling transition and fluorescence from this transition is detected in the upper detection chamber. The time-integrated detected signal is proportional to the number of atoms in the $F = 4$ state. After this the $F = 4$ atoms are pushed away by radiation pressure preventing them from entering the lower detection zone; hence only the $F = 3$ atoms remain. The laser beam tuned to the $F = 3 \rightarrow F' = 4$ repumper transition is used to pump these atoms to the $F = 4$ state and fluorescence induced by a laser tuned to the $F = 4 \rightarrow F' = 5$ cycling transition is detected in the lower detection chamber giving the number of atoms in the $F = 3$ state.

The 9.2 GHz microwave signal for interrogation of the atomic clock transition is synthesized by multiplication and mixing of the frequency produced by a dielectric resonant oscillator (DRO) with the frequency of an RF synthesiser. The DRO is frequency referenced to a high-stability radio-frequency source (a BVA quartz-crystal oscillator or a cryogenic sapphire oscillator), which in turn is locked to a hydrogen maser.

To measure the difference between the frequency of the atomic transition and the 9.2 GHz oscillator, the atoms are probed on either side of the central Ramsey fringe and the two transition probabilities are subsequently compared. The frequency difference is calculated from the imbalance of the signals and the values are fed back to the RF synthesiser in the 9.2 GHz oscillator, which tracks the position of the fringe centre.

5.1.1.2 Uncertainty budget

The fundamental limit to the accuracy with which frequency measurements can be made is the accuracy of the frequency standard used as a reference. Both the statistical (type A) and the systematic (type B) uncertainties must be considered. A good description of the statistical uncertainty obtained after a measurement time τ is given by the Allan deviation $\sigma_y(\tau)$ described in Section 2.4.2.2.

In a caesium fountain primary frequency standard, four noise contributions have to be taken into account. The Allan deviation can be written as [148]:

$$\sigma_y(\tau) = \frac{1}{\pi Q_{\text{at}}} \sqrt{\frac{T_c}{\tau}} \left(\frac{1}{N_{\text{at}}} + \frac{1}{N_{\text{at}} \epsilon_c n_{\text{ph}}} + \frac{2\sigma_{\delta N}^2}{N_{\text{at}}^2} + \gamma \right)^{1/2}, \quad (5.1)$$

where the terms in brackets represent, in order, the contributions from quantum projection noise, photon shot noise, electronic detection noise and local oscillator noise. Here Q_{at} is the atomic quality factor defined as

$$Q_{\text{at}} = \frac{\nu_0}{\Delta\nu} \quad (5.2)$$

where ν_0 is the caesium hyperfine frequency and $\Delta\nu$ the width of the Ramsey fringe. T_c is the fountain cycle duration, τ the measurement time and $\tau > T_c$ for the expression to be valid. N_{at} is the number of detected atoms, n_{ph} is the average number of photons scattered per atom during detection, ϵ_c is the photon collection efficiency, $\sigma_{\delta N}^2$ is the uncorrelated root mean square fluctuation of the atom number per detection channel and γ is the contribution of the frequency noise of the local oscillator. From Eq. (5.1) one can see that a high number of atoms used in the fountain can reduce the frequency instability to the local oscillator noise limit γ . For a typical fountain employing a local oscillator locked to the best commercially available quartz oscillator, the relative frequency instability is of order $10^{-13}(\tau)^{-1/2}$ [149]. By using a low noise cryogenic sapphire oscillator as the local oscillator a frequency instability of $4 \times 10^{-14}(\tau)^{-1/2}$ has been achieved [148].

Several physical phenomena related to atomic interactions with external fields, collisions between atoms, and technical details of the construction of the standard subsystems such as the microwave cavity [149] lead to systematic shifts of the frequency of the clock transition. The influence of each effect has to be quantified for a particular device, after which the frequency of the clock transition can be corrected for the associated shifts. However, the uncertainty associated with the correction procedure

limits the accuracy of this correction. As the individual systematic uncertainties are independent, the resulting total systematic uncertainty is the square root of the sum of squares of the individual contributions. The overall uncertainty is given by the sum in quadrature of the statistical uncertainty (u_A), which can be reduced by increasing averaging time, and the systematic uncertainty (u_B) specific for the particular clock.

Although the magnitudes of the systematic shifts have to be evaluated for each particular apparatus, their types are common for all caesium fountain primary frequency standards. The major sources of systematic uncertainty, and the nature and scale of these effects are shown in Table 5.1 for the example of the NPL-CsF2 caesium fountain complete accuracy evaluation reported in [116] with further improvements reported in [150]. The overall type B uncertainty for this caesium fountain is currently 2.3×10^{-16} .

5.1.2 Hydrogen maser

The NPL frequency combs are not referenced directly to the caesium fountain frequency standard. Instead, they are referenced to a hydrogen maser because this is available all the time. The two hyperfine levels of the ground state of the hydrogen atom are separated by 1.42 GHz and in a hydrogen maser this frequency is used to generate a 10-MHz reference signal. There are four hydrogen masers at NPL; HM2 is the one used as the source of the reference signal for the combs. Figure 5.3 shows the typical stability of hydrogen maser HM2 measured relative to another NPL hydrogen maser. Since the noise of each maser contributes to the measured instability, this result suggests that the stability of maser HM2 is lower than 4×10^{-15} at a timescale of 10^3 s.

At present, maser HM2 is the clock used for the UK realization of Coordinated Universal Time, UTC(NPL), and so, unlike the others, its frequency is periodically steered. UTC(NPL) is compared with UTC by satellite time and frequency transfer techniques and the difference is published in “Circular T” (see for example [151]). Thus an op-

Effect	Nature	$u_B/10^{-16}$
Second-order Zeeman	Applied magnetic field	0.8
Blackbody radiation	Blackbody radiation surrounding the atomic absorbers	1.1
Ac Stark (lasers)	Leaking resonant laser light during the Ramsey interaction	0.1
Microwave spectrum	Spurious spectral components in the vicinity of the clock resonant frequency	0.1
Gravity	Change of the frequency of any clock with gravitational potential	0.5
Cold collisions (Cs-Cs)	Collisions among the cold atoms in the cloud	0.4
Background gas collisions	Collisions with residual gas atoms	1.0
Rabi, Ramsey pulling	Possible transitions to and between states of $m_F \neq 0$	0.1
Cavity phase (distributed)	Phase variation pattern of the microwave field in the Ramsey cavity	1.1
Cavity phase (dynamic)	Temporal phase changes due to temperature changes of the cavity	0.1
Cavity pulling	Maser oscillation of the atoms in the cavity (radiation damping)	0.2
Microwave leakage	Microwaves resonant with the atomic transition leaking into the flight tube	0.6
Microwave recoil	Change in the atom's kinetic energy due to the absorption of a microwave photon	0.3
Second-order Doppler	Frequency shift due to the second-order Doppler effect	0.1
<i>Total</i> (1σ)		2.3

Table 5.1: Systematic effects and their uncertainties (u_B) forming the uncertainty budget for NPL-CsF2 [150].

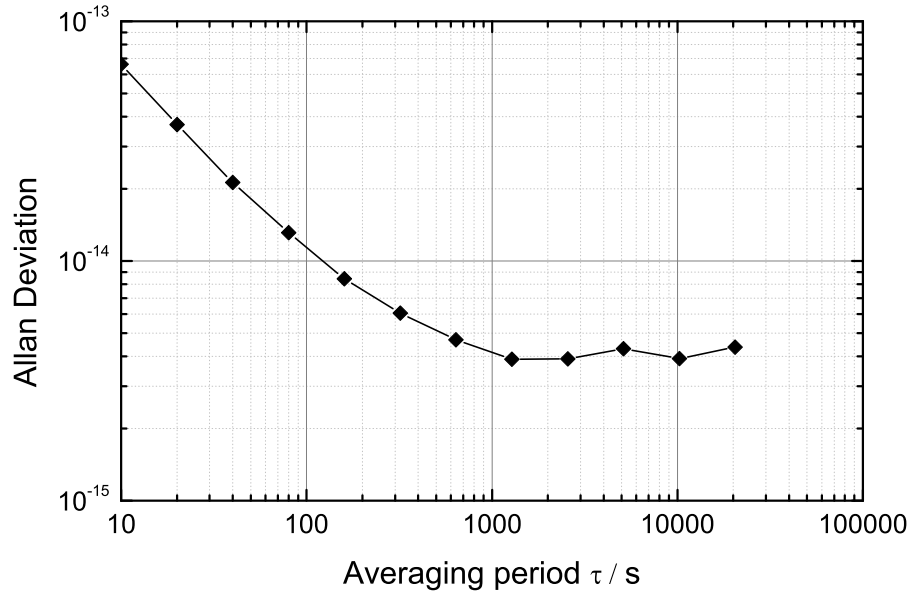


Figure 5.3: The typical stability of the HM2 hydrogen maser measured relative to another NPL hydrogen maser using a phase comparator.

tical frequency measured relative to the frequency of HM2 can be traced back to the SI second. The details of this procedure are described in Section 6.2.3, and typically lead to a relative uncertainty of the maser frequency of 1×10^{-14} . Therefore, absolute optical frequency measurements referenced to UTC in this way are sufficiently accurate if the systematic uncertainty of the frequency standard is greater than this, for example the measurements reported in [11] and described in Chapter 6. When higher accuracy is desired, the frequency combs are referenced to a 10-MHz signal from a hydrogen maser, which is simultaneously calibrated using the local caesium fountain primary frequency standard, as in the case of the absolute frequency measurement of the $^{171}\text{Yb}^+$ trapped ion frequency standard reported in [152].

5.1.3 GPS-disciplined oscillator

Although a hydrogen maser produces a reference signal stable to parts in 10^{13} at 1s, this level of stability is not always necessary. In cases where the instability and

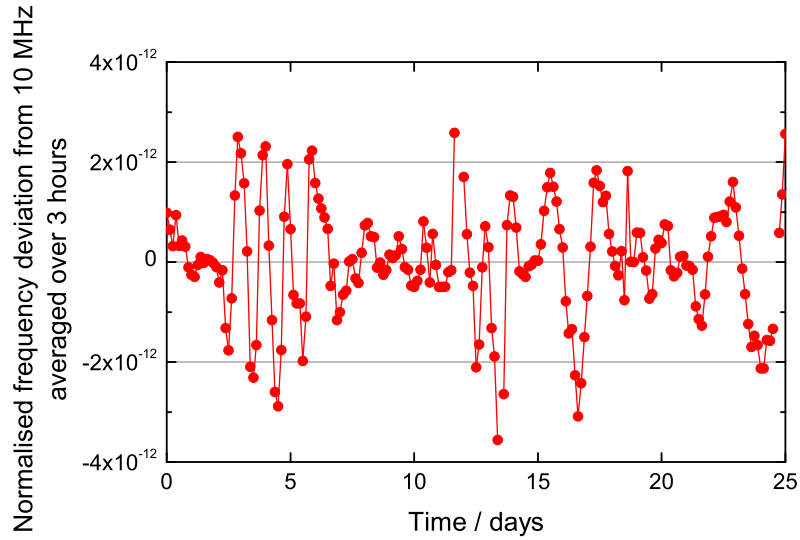


Figure 5.4: The normalized frequency deviation of the GPS-disciplined quartz oscillator from the HM2 hydrogen maser. Each data point is an average over 3 hours.

accuracy of the frequency to be measured are orders of magnitude higher than the instability and accuracy of the reference signal, an alternative source of 10 MHz signal can be used. For example, the NPL transportable frequency comb described in Section 3.1 [113] can be referenced to the 10-MHz output signal from a GPS-referenced quartz oscillator. The reference system comprises three parts: a Rapco 803M quartz oscillator steered by a Rapco 2804AR unit containing a rubidium reference oscillator which is disciplined via a single-frequency antenna link to the GPS network. This reference source has the obvious advantage that the signal may be obtained at almost any location, and so it is ideal for a transportable system.

Figure 5.4 shows the normalized frequency deviation of the GPS-disciplined quartz oscillator from the frequency of the hydrogen maser used to generate the UTC(NPL) timescale, averaged over 3 hour periods. The measurements were performed over a period of 25 days using a phase comparator with the hydrogen maser as a reference. It can be seen that the maximum fractional frequency deviation does not exceed 4×10^{-12} . This measurement therefore gives an estimate of the accuracy of the GPS-disciplined oscillator.

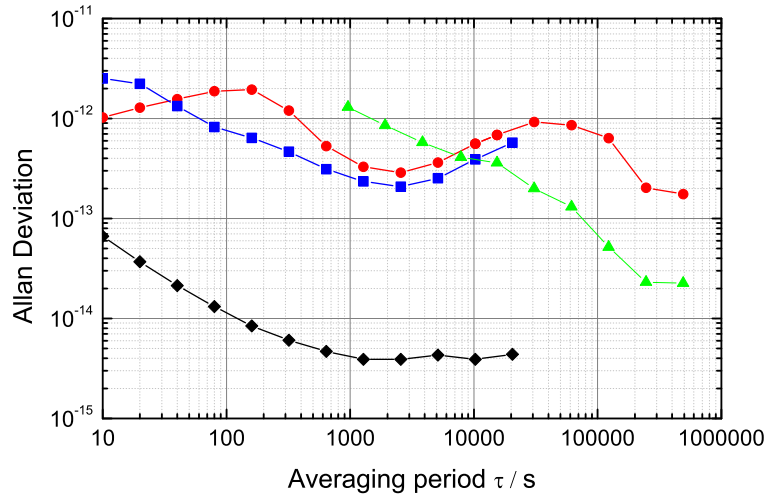


Figure 5.5: The Allan deviation of the GPS-disciplined rubidium oscillator (blue squares), the quartz oscillator locked to the GPS-disciplined rubidium oscillator (red circles) a GPS-disciplined oscillator from Time and Frequency Solutions (green triangles) and the HM2 hydrogen maser (black diamonds). These values are calculated from 20 days of measurements.

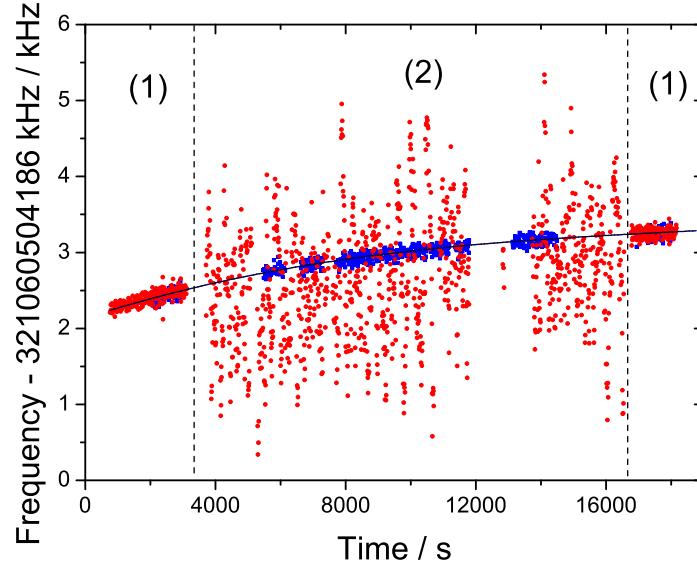


Figure 5.6: Frequency measurements of a high-finesse cavity-stabilised Ti:sapphire laser using a Ti:sapphire laser-based comb (blue squares) and transportable comb (red circles); the black line shows the drift of the Fabry-Perot cavity. During the periods marked (1) the transportable comb was referenced to a hydrogen maser; in the period (2), it was referenced using the GPS-disciplined oscillator.

Figure 5.5 shows the stability of the outputs from the quartz oscillator and the rubidium oscillator measured with the same maser-referenced phase comparator. It can be seen that the introduction of the quartz oscillator gives an improvement in the measured stability at the shortest timescales compared to the signal from the rubidium oscillator. However, the signal from the quartz oscillator is less stable when averaged over a few minutes than the signal obtained directly from the rubidium oscillator, even though it is steered by the rubidium oscillator. Also shown is the stability of a Time and Frequency Solutions 8-channel GPS-disciplined oscillator, which gives superior stability to the Rapco unit at long time-scales, but inferior stability when averaged over less than a few hours. These measurements indicate that adjustments to the time constants of the servos between the Rapco units could potentially lead to improved stability of the oscillator system.

Figure 5.6 illustrates the difference in the accuracy of a frequency comb system when referenced to a hydrogen maser or to the GPS-disciplined oscillator system. Frequency measurements of a laser stabilised to a high-finesse Fabry - Perot cavity were performed simultaneously using two combs. While the Ti:sapphire comb was referenced to a hydrogen maser all the time, the transportable comb was referenced to the maser at the beginning and end of the measurement period and to the GPS-disciplined unit the rest of the time. The frequency measured with each comb agreed to within the uncertainty of the GPS-disciplined oscillator.

5.2 Stability and accuracy of the 10-MHz reference signal in the combs laboratory

Since the maser is not located in the same laboratory as the combs, the signal passes through a distribution system consisting of cables and a number of distribution amplifiers. Potential degradation of the stability of the maser signal during the transfer to the combs laboratory as well as possible systematic frequency shifts introduced by the distribution amplifiers were therefore investigated.

Figure 5.7 shows the distribution of the 10-MHz maser signal between different laboratories within NPL. The signal from the active hydrogen maser HM2 located in Lab2 is transferred to a first distribution amplifier situated in Lab1. One of the output signals from this distribution amplifier is used as a reference signal for a Phase and Frequency Comparator (PFC) situated in the same room, while another is transmitted back into Lab2 where it is amplified by a second distribution amplifier and then sent to a third distribution amplifier (DS-100) located in the frequency combs laboratory (Lab3). In the frequency combs laboratory the signal is further amplified by a FDA-1050 distribution amplifier, which produces reference signals for the counters and synthesisers used with the frequency combs. The combs laboratory also has a direct connection to the phase comparator in Lab1, which can be used to send

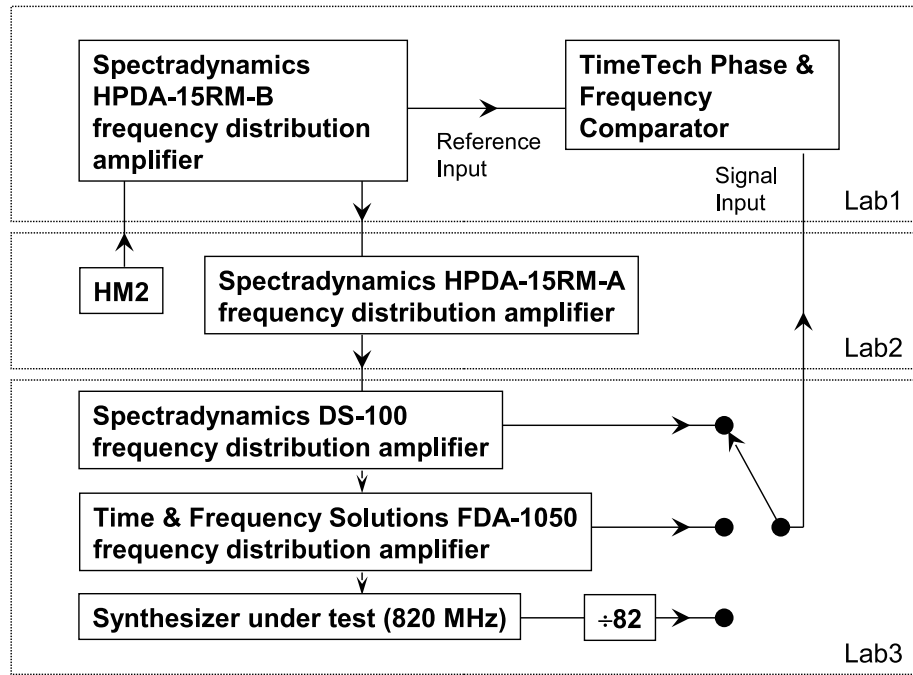


Figure 5.7: Distribution of the 10 MHz reference signal from an active hydrogen maser Datum MHM-2010 (HM2) located in the hydrogen maser laboratory (Lab2) to the TimeTech Phase and Frequency Comparator (PFC) situated in the Time scale laboratory (Lab1) and to the combs laboratory (Lab3). The combs laboratory also has a direct connection to the phase comparator in Lab1.

back signals from the distribution amplifiers or a synthesiser producing a 10-MHz signal for comparison against the original 10-MHz signal sent from the maser. To minimize temperature-dependent phase shifts in the link, coaxial cables (RG-58 and FSJ1-50A) with low thermal coefficients were used. Measurements on RG-58 type cable show a net electrical delay variation of about $-0.42 \text{ ps K}^{-1}\text{m}^{-1}$ between temperatures of -20°C to $+40^\circ\text{C}$ [153], while the thermal coefficient of FSJ1-50A cable is $0.03 \text{ ps K}^{-1}\text{m}^{-1}$ [154]. The corresponding phase shift of the 10-MHz frequency signal is $2.6 \times 10^{-5} \text{ rad K}^{-1}\text{m}^{-1}$ and $1.9 \times 10^{-6} \text{ rad K}^{-1}\text{m}^{-1}$ for RG-58 and FSJ1-50A cables respectively.

In this section the results of frequency stability tests as well as an investigation of possible systematic frequency shifts of the 10-MHz maser reference signal supplied to the combs laboratory are described.

5.2.1 Influence of distribution system on the 10-MHz signal stability

In order to measure the excess instability of the 10-MHz signal introduced by the distribution system the output signal from the DS-100 distribution amplifier was sent to the phase comparator and compared to the original 10-MHz reference signal from HM2 for a total of 31 days.

Figure 5.8 shows the calculated Allan deviation as function of averaging time. The red curve represents the typical behaviour of the Allan deviation which was found to be independent of the day of the week, suggesting that daytime activities within the building do not degrade the stability of the distributed maser signal significantly. The $1/\tau$ dependency for short averaging times τ is consistent with the dominant noise process being white phase noise as expected for a hydrogen maser. The black curve represents the average Allan deviation over the 31 day period, with the error bars showing the spread of values obtained for each averaging time on different days. The

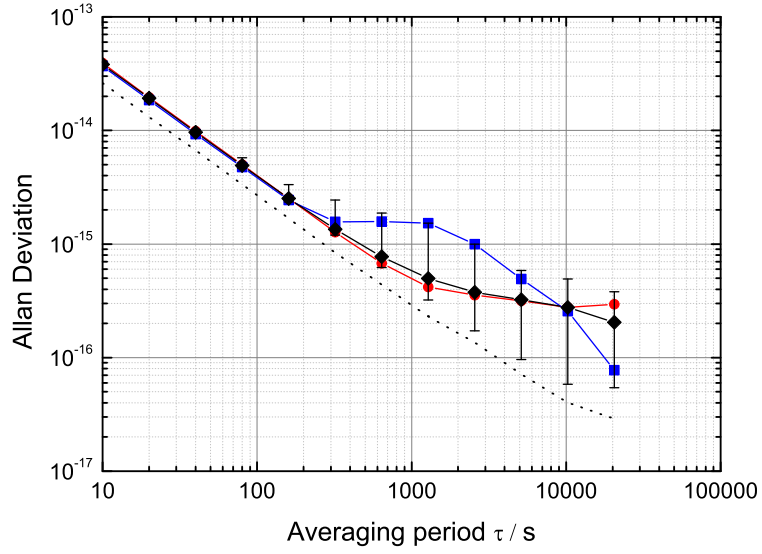


Figure 5.8: Allan deviation of the 10-MHz signal after the DS-100 distribution amplifier compared to the signal from hydrogen maser HM2: average over 31 day period (black diamonds) with spread shown by the error bars, typical day (red circles) and a day with anomalously high medium term instability (blue squares). The dashed line shows the phase comparator measurement noise floor derived from the measurements of the 10-MHz signal from maser HM2 against itself in Lab1.

blue curve shows the Allan deviation for a day when the stability of the signal from the distribution amplifier was worse than normal. The anomalous behaviour of the blue curve at $\tau > 320$ s was traced to large frequency excursions in the time interval between 70000 s and 80000 s on this day of measurements. If these data points are removed the stability demonstrates the typical behaviour.

These results show that the noise introduced by the distribution system (the link from the Lab1 to the comb laboratory and the DS-100 distribution amplifier) and the link from the comb laboratory back to the phase comparator in Lab1 produces an excess instability of the 10-MHz signal from the hydrogen maser. This effect is illustrated in Fig. 5.8 where the Allan deviation of the signal after the DS-100 distribution amplifier compared to the original signal from hydrogen maser HM2 is 1.5 times bigger than the Allan deviation of the 10-MHz signal from maser HM2 measured against itself.

The second distribution amplifier in the combs laboratory (FDA-1050) in Fig. 5.7 produces the 10-MHz reference maser signal used for the synthesisers and frequency counters in the combs laboratory as well as other optical frequency standards laboratories. The excess instability introduced by the FDA-1050 distribution amplifier was measured in the same way as for the DS-100 distribution amplifier. Figure 5.9 shows examples of typical, average and bad Allan deviation as a function of averaging time. Since in practice the comb data obtained on the day when the stability of the reference signal were lower than average would be rejected, only typical data were used for further analysis.

A comparison between the results for the DS-100 and FDA-1050 distribution amplifiers shown in Fig. 5.8 and Fig. 5.9 respectively shows that for short averaging times the FDA-1050 distribution amplifier degrades the stability slightly. For example, the Allan deviation values for 10 s averaging time are 3.8×10^{-14} and 4.5×10^{-14} for the DS-100 and FDA-1050 distribution amplifiers respectively, which corresponds to a degradation of the stability of the maser signal by a factor of 1.1. However, for longer averaging times no significant difference between the excess instability of the two distribu-

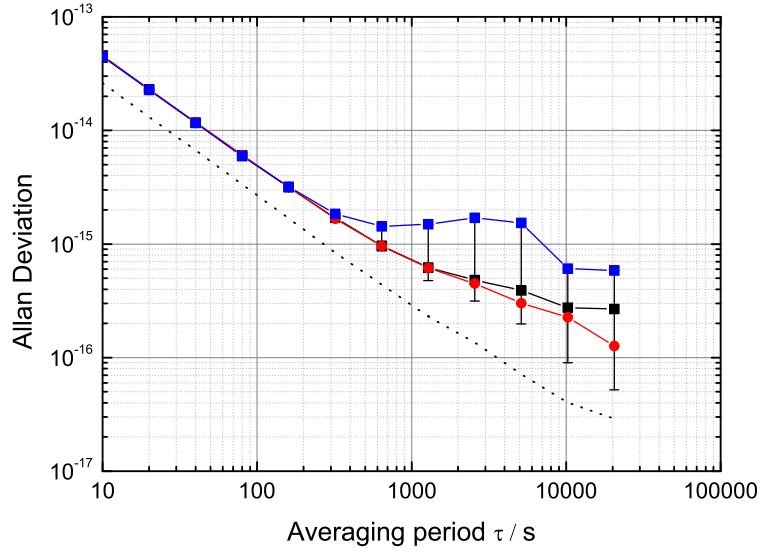


Figure 5.9: Allan deviation of the 10-MHz signal after the FDA-1050 distribution amplifier compared to the original reference signal from hydrogen maser HM2: average over 20 days (black squares) with spread shown by error bars; typical day (red circles) and one day which showed higher than average medium term instability (blue squares). The dashed line shows the phase comparator measurement noise floor derived from the measurements of the 10-MHz signal from maser HM2 against itself.

tion amplifiers was observed, suggesting that the noise of the FDA-1050 distribution amplifier does not further degrade the maser signal stability at long timescales.

5.2.2 Accuracy of the 10-MHz signal delivered to the combs laboratory

In order to investigate possible systematic frequency shifts of the 10-MHz maser reference signal supplied to the combs laboratory and frequency shifts introduced by the second distribution amplifier (FDA-1050), the phase comparator data collected using the setup shown in Fig. 5.7 were analysed. As shown in Section 5.2.1, the Allan deviations of both the DS-100 and the FDA-1050 distribution amplifiers start to flatten out for averaging times greater than 5120 seconds, so this averaging time was used to investigate the systematic variations of the reference signal delivered to the combs laboratory during the day.

Figure 5.10 shows the normalised frequency deviation of the 10-MHz signal from the DS-100 distribution amplifier from the original reference signal from hydrogen maser HM2 averaged over 5120 seconds as a function of the time of the day. Different points corresponding to the same time correspond to data taken on separate days and the error bars show the instability observed on that particular day for the given averaging time. The day-to-day variations of the normalised frequency deviation result in the spread of values $\pm 1.5 \times 10^{-15}$. One can see that apart from the day-to-day spread of values, there is a pattern of frequency variation during the day with a period of half a day. Although the reason for these variations is not known, it can potentially lead to errors in frequency measurements made using the femtosecond combs if the reference signal is not monitored.

Similar analysis was performed for the FDA-1050 distribution amplifier. Figure 5.11 shows the normalised frequency deviation of the 10-MHz signal from the FDA-1050 distribution amplifier from the original signal from the hydrogen maser HM2 obtained

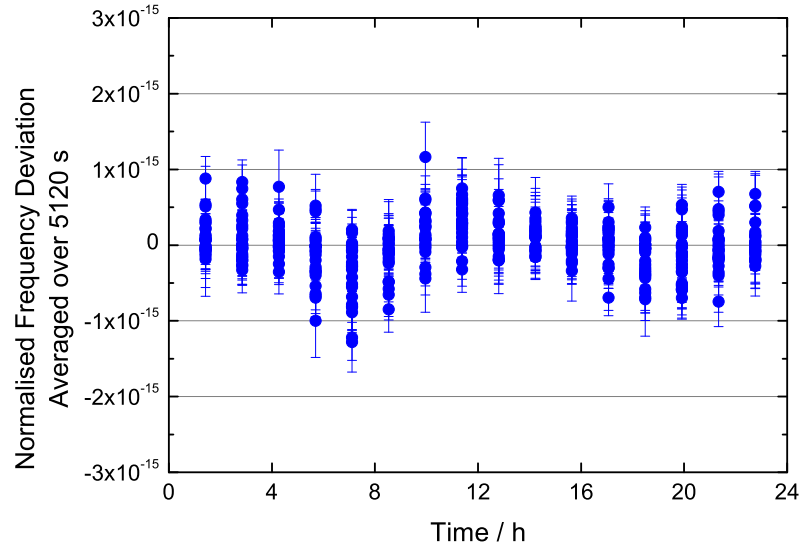


Figure 5.10: Normalised frequency deviation of the 10-MHz signal after the DS-100 distribution amplifier from the original reference signal from hydrogen maser HM2, averaged over 5120 second periods as a function of the time of day, where $t = 0$ is midnight. The data were taken over a period of 25 days and the error bars correspond to the statistical uncertainty on the individual 5120 s points as determined from the Allan deviation curve.

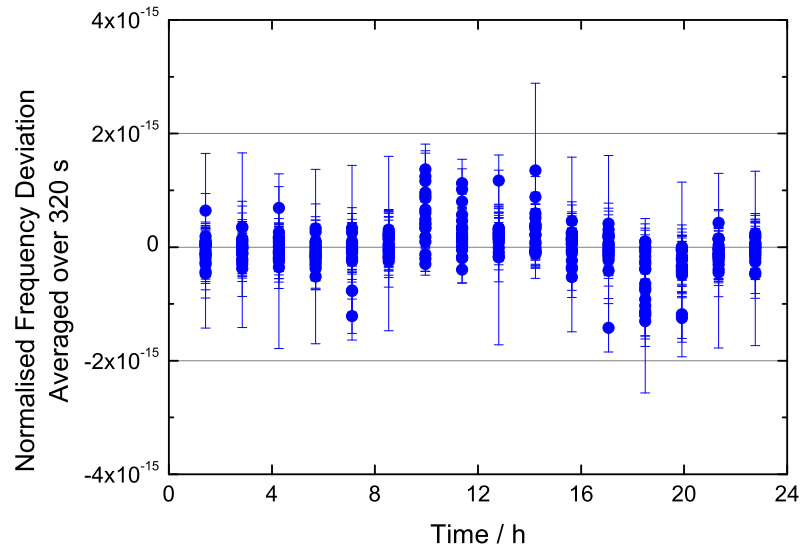


Figure 5.11: Normalised frequency deviation of the 10-MHz signal from the FDA-1050 distribution amplifier from the original signal from the hydrogen maser HM2 averaged over 5120 second periods as a function of the time of day, where $t = 0$ is midnight. The data were taken over a period of 19 days and the error bars correspond to the statistical uncertainty on the individual 5120s points as determined from the Allan deviation curve.

by averaging 19 days of data over 5120 second periods. It can be seen that the spread of values $\pm 1.5 \times 10^{-15}$ is similar to that measured at the output of the DS-100 distribution amplifier. These results prove that the FDA-1050 distribution amplifier does not further degrade the accuracy of the maser signal obtained from the DS distribution amplifier.

In summary, the noise introduced by the distribution system including the link from the combs laboratory back to the phase comparator typically leads to a 1.5 times increase of the Allan deviation of the signal after the DS-100 distribution amplifier measured against the original maser signal compared to the Allan deviation of the maser signal measured against itself. The frequency of the HM2 maser reference signal delivered to the combs laboratory fluctuates during the day as well as day-to-day with the spread of the normalised frequency deviation of the DS-100 signal from the original maser signal being $\pm 1.5 \times 10^{-15}$. The noise of the second distribution amplifier (FDA-1050) neither affects the maser signal stability, providing that the averaging time is longer than 640 seconds, nor introduces systematic frequency shifts of the 10-MHz maser signal.

5.3 Stability and accuracy of maser-referenced synthesisers

Since the frequency used to lock the repetition rate of the Ti:Sapphire comb is derived from a maser-referenced synthesiser, the synthesiser itself can be a source of potential systematic frequency shifts and degradation of the frequency stability. Additionally, temperature variations in the laboratory might potentially degrade the accuracy of the synthesiser signal; therefore the temperature dependency of the synthesiser frequency was tested. This section describes tests of two different synthesisers (IFR 2023A and HP 8662A) that could be used for optical frequency measurements.

5.3.1 Stability

The stability of the reference signal sets a lower limit to the fractional frequency stability of the signal generated by a synthesiser. The IFR 2023A (IFR) and the HP 8662A (HP) synthesisers were tested to check whether these were capable of providing signals with a fractional frequency stability comparable with the stability of the maser signal. The synthesiser frequency for the stability test was set to 820 MHz, since this frequency was close to the one used to lock the repetition rate of the Ti:Sapphire laser based frequency comb. To obtain a 10-MHz signal of sufficient amplitude for the phase comparator, the synthesiser signal was frequency divided by 82, as shown in Fig. 5.7, amplified and filtered.

Figure 5.12 shows the average Allan deviation calculated from the measurement data for the IFR synthesiser (red), HP synthesiser (blue) and the DS-100 distribution amplifier (black) compared to the original reference signal from hydrogen maser HM2. One can see that even for short averaging times the Allan deviation curve calculated for the HP synthesiser does not have a $1/\tau$ dependency on the averaging time, suggesting that white phase noise is not the dominant noise process. As a result, the decrease of the excess instability introduced by the HP synthesiser with averaging time is slower than that calculated for the DS-100 distribution amplifier, and it can become a limiting factor for frequency measurements.

In contrast, the IFR synthesiser shows $1/\tau$ behaviour up to 20480 s averaging time. At shorter averaging times the the excess instability of the IFR synthesiser results in an Allan deviation of 8.3×10^{-14} at a 10 second averaging time compared to 3.8×10^{-14} calculated for the DS-100 distribution amplifier. However, for averaging times longer than 640 seconds the excess instability of the IFR synthesiser is within the spread of Allan deviation values obtained for the DS-100 distribution amplifier on different days, so the IFR synthesiser noise does not further affect the stability of the maser signal delivered to the combs laboratory at these timescales.

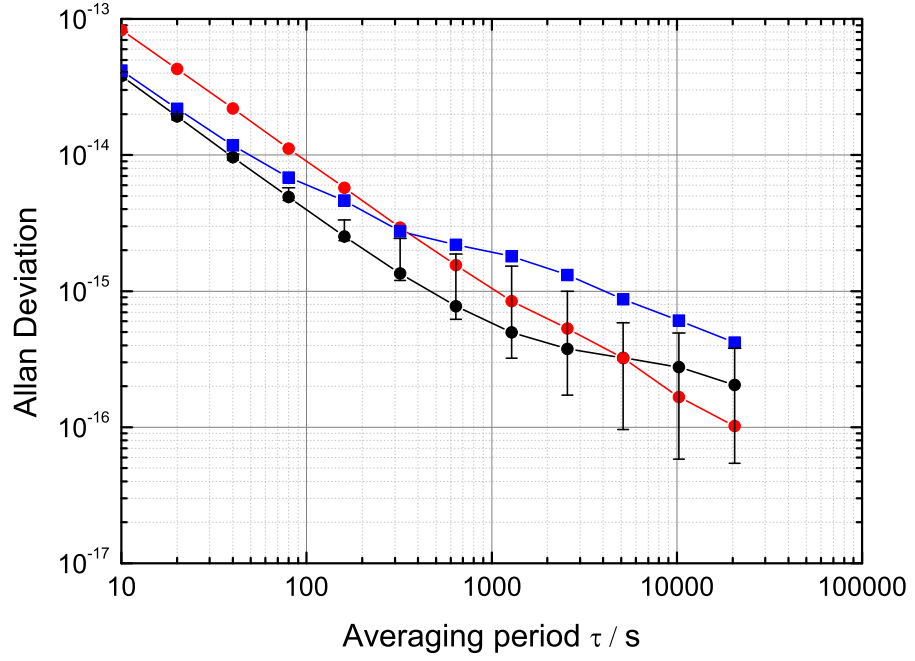


Figure 5.12: Averaged Allan deviation of the 10-MHz signal after the IFR 2023A synthesiser (red) and the HP 8662A synthesiser (blue) compared to the original reference signal from hydrogen maser HM2. For comparison, the black curve shows the Allan deviation of the 10-MHz signal after the DS-100 distribution amplifier averaged over 31 days, the error bars showing the spread of the values obtained for each averaging time.

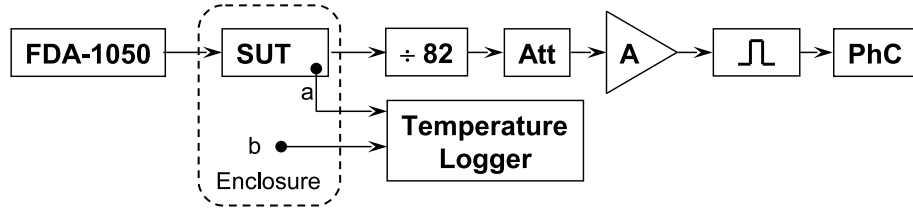


Figure 5.13: Schematic diagram of the setup used for synthesiser temperature sensitivity measurements. FDA-1050 – distribution amplifier; SUT – synthesiser under test located inside enclosure; temperature sensors: a – attached to the synthesiser case, b – measuring air temperature, data collected by Temperature Logger; $\div 82$ – SP8402 frequency divider; Att – 13 dB attenuator; A – MAN-1LN Mini-Circuits amplifier; PhC – phase comparator. The band pass filter consisted of two Mini-Circuits BPF-10.7 filters in series.

5.3.2 Temperature sensitivity

Figure 5.13 shows a schematic of the setup used for the synthesiser temperature sensitivity tests. To generate a 10-MHz signal a setup similar to the one described in Section 5.3.1 was used; however in this case the synthesiser was placed in an enclosure and its temperature was varied from 22 to 35 degrees Celsius with both positive and negative rates of change. The temperatures of the synthesiser case and the air temperature inside the enclosure were simultaneously logged to a computer. Since the main aim of this test was to establish how the output frequency of the synthesiser depended on the temperature variations in the laboratory, the air temperature was used for the analysis.

In the case of the IFR synthesiser the temperature change was realized with a heater placed inside the enclosure. The heating and cooling cycles were alternated several times during the day. The HP synthesiser heated up the enclosure significantly itself, therefore there was no need for a separate heater. The downside was that cooling was only possible in this case by opening the enclosure, making it difficult to obtain small negative rates of change of temperature.

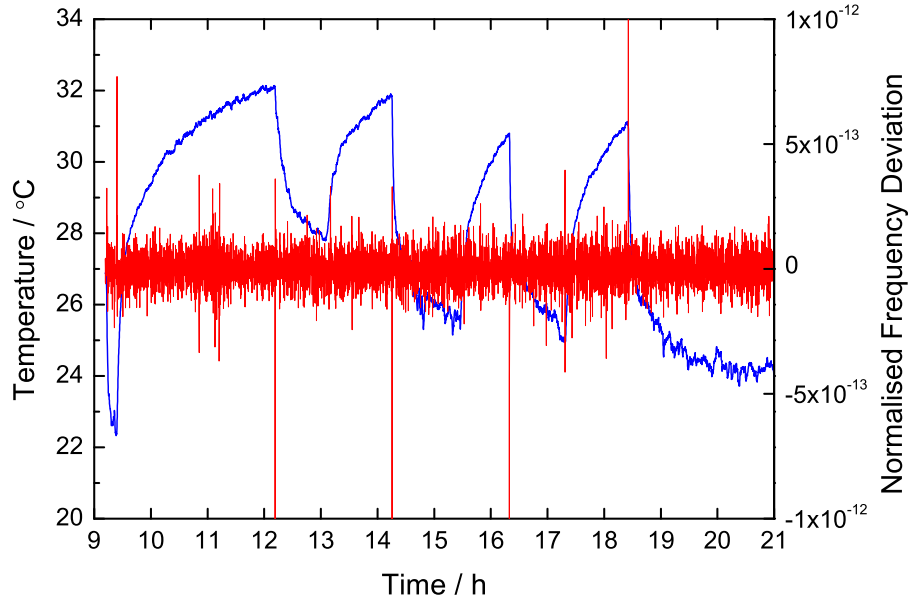


Figure 5.14: IFR synthesiser temperature sensitivity test. Air temperature inside the enclosure (blue) and normalised frequency deviation of the 10-MHz signal produced by the IFR synthesiser from the reference signal from hydrogen maser HM2 obtained from the phase comparator (red) as a function of time.

5.3.2.1 IFR 2023A synthesiser

Figure 5.14 shows the typical temperature variation inside the enclosure and the normalised frequency deviation of the frequency-divided signal generated by the IFR synthesiser from the HM2 hydrogen maser obtained from the phase comparator as a function of time. One can see large spikes in the frequency deviation plot at times when the sign of the rate of change of temperature was altered. However there is no visible correlation between continuous temperature changes and the normalised frequency deviation of the synthesiser signal (i.e. it is less than the noise). These results suggest that the synthesiser has a built in system for compensation of the temperature-dependent frequency shifts. The quality of this system can be assessed via the dependence of the synthesiser output frequency on the rate of temperature change.

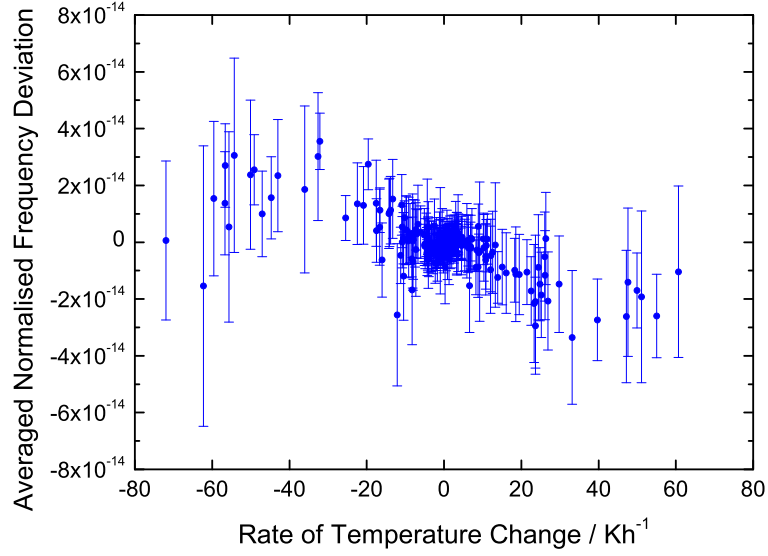


Figure 5.15: Averaged normalised frequency deviation of the 10-MHz output signal produced by the IFR synthesiser from the reference signal from the hydrogen maser HM2 as a function of the rate of temperature change.

In order to calculate the dependence of the synthesiser frequency on the rate of temperature change the temperature data were divided into short periods where the temperature dependence on time could be approximated with a straight line. This approximation was used to calculate the rate of temperature change for each period. The normalised frequency deviation of the synthesiser output signal from the HM2 signal for each time period was analysed to obtain mean values with corresponding standard errors. The results of this analysis are shown in Fig.5.15.

It can be seen that the dependence of the synthesiser output frequency on the rate of temperature change in the range -80 K/h to 80 K/h is not linear, however, in practice, such extreme rates of change of temperature do not occur under normal laboratory conditions. The temperature in the combs laboratory is typically stable to within $\pm 0.1^\circ\text{C}$, although there were several occasions when the temperature monitoring showed oscillations with a period of several hundred seconds and a maximum rate

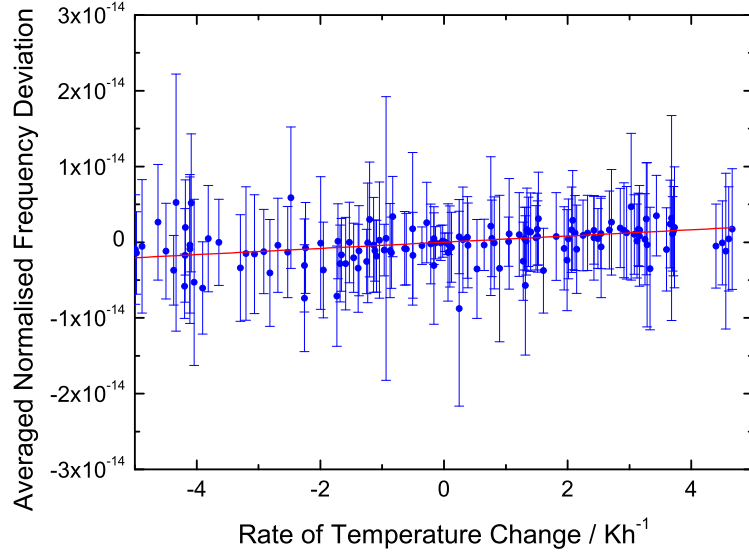


Figure 5.16: A linear fit to the averaged normalised frequency deviation of the 10-MHz signal produced by the IFR synthesiser from the reference signal from hydrogen maser HM2 for rates of temperature change from -5 Kh^{-1} to 5 Kh^{-1} .

of temperature change of 3.5 Kh^{-1} ; hence only the central part of the data is taken into account during the analysis (Fig. 5.16). A linear fit to this part of the data gives a fractional frequency change of $4.1(0.7) \times 10^{-16} (\text{K/h})^{-1}$, which corresponds to a fractional frequency error of $1.4(0.5) \times 10^{-15}$ for the rate of temperature change of 3.5 Kh^{-1} . However, as this rate of temperature change was observed for short periods of temperature oscillations, it will average to zero over longer timescales.

5.3.2.2 HP 8662A synthesiser

Figure 5.17 shows the typical temperature variation inside the enclosure and the normalised frequency deviation of the frequency signal obtained from the HP synthesiser from the HM2 hydrogen maser acquired from the phase comparator as a function of time. Unlike the case of the IFR synthesiser, the change of the normalised frequency deviation of the HP synthesiser signal with temperature can be observed. However,

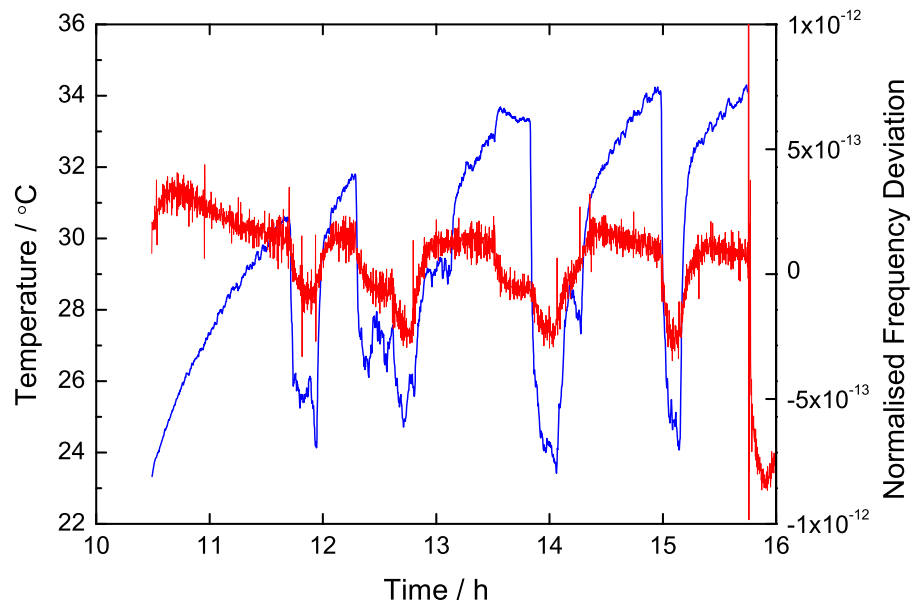


Figure 5.17: HP synthesiser temperature sensitivity test. Air temperature inside the enclosure (blue) and normalised frequency deviation of the 10-MHz signal produced by the HP synthesiser from the reference signal from hydrogen maser HM2 obtained from the phase comparator (red) as a function of time.

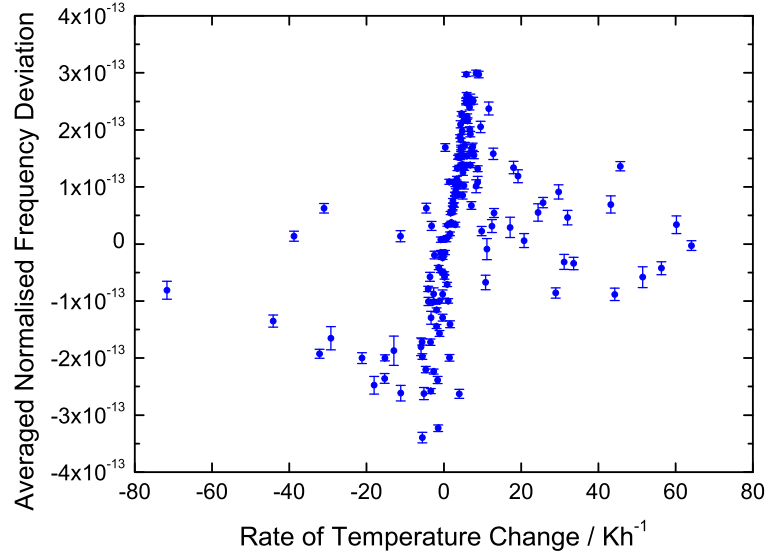


Figure 5.18: Averaged normalised frequency deviation of the 10-MHz signal produced by the HP synthesiser from the reference signal from hydrogen maser HM2 as a function of the rate of temperature change.

more detailed analysis of the data shows that higher air temperatures can lead to either an increase or decrease of the normalised frequency deviation depending on the rate of temperature change. Once again these results indicate the presence of internal compensation of the temperature-dependent frequency shifts. To assess the quality of this compensation, the frequency dependence on the rate of temperature change was investigated.

To find out whether the synthesiser frequencies were correlated with the rate of temperature change, the data were analysed in the same way as for the IFR synthesiser (Fig. 5.18). Nonlinear behaviour was also observed for the HP synthesiser, but was much more pronounced than for the IFR synthesiser. Hence only the data corresponding to rates of temperature change from -5 Kh^{-1} to 5 Kh^{-1} were once again taken into account during the analysis (Fig. 5.19). The observed trend was similar to the one demonstrated by the IFR synthesiser, showing the increase of the averaged

normalised frequency deviation with the increase of the rate of temperature change, however the spread of the mean values of the averaged normalised frequency deviation was more than order of magnitude bigger than the corresponding standard errors.

This effect could be explained by the lack of control over the temperature change inside the enclosure. Instead of using a separate heater like in the case of the IFR synthesiser, the HP synthesiser heated up the enclosure itself, hence the only way of controlling the temperature was by opening the enclosure. As the result, small rates of change of temperature as well as the intermediate negative rates were difficult to obtain. Consequently only short sequences of data were available for calculations of the mean values of the averaged normalised frequency deviation at these rates of temperature change. This effect is clearly seen in Fig. 5.19, comparing the spread of values of the averaged normalised frequency deviation for rates of temperature change from -5 Kh^{-1} to 2 Kh^{-1} and from 2 Kh^{-1} to 5 Kh^{-1} . In order to estimate a fractional frequency change in the same way as it was done for the IFR synthesiser, the length of the experiment should be increased significantly to obtain sufficient amount of data for averaging. Another option would be to redesign the enclosure in the way that the temperature can be controlled.

5.3.3 Accuracy

To assess the performance of the synthesisers under normal laboratory conditions, the possible systematic frequency shifts introduced by the maser-referenced synthesiser were investigated in the same way as in case of the distribution amplifiers described in Section 5.2.2.

Both synthesisers produced a signal at 820-MHz, which was divided to obtain a 10-MHz signal for the phase comparator using the setup shown in Fig. 5.7. The accuracy of the signal produced by the IFR and HP synthesisers was analysed in the same way as the accuracy of the maser signal after the distribution amplifiers.

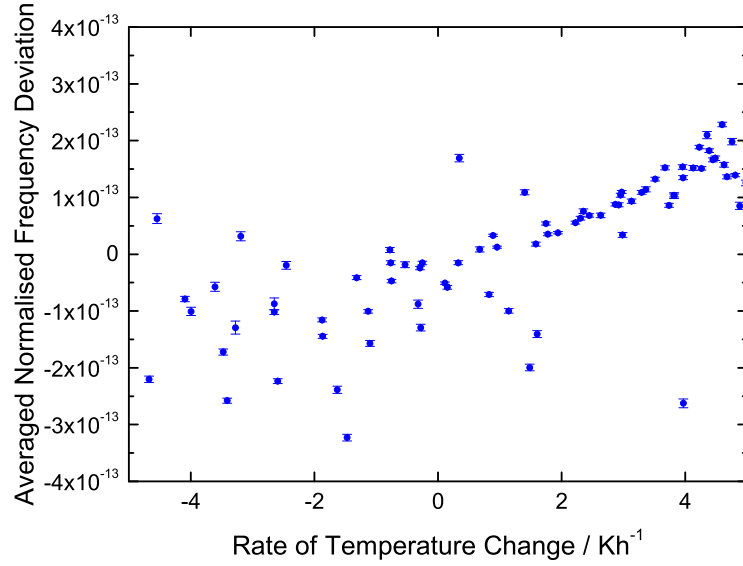


Figure 5.19: Averaged normalised frequency deviation of the 10-MHz signal produced by the HP synthesiser from the reference signal from hydrogen maser HM2 for rates of temperature change from from -5 Kh^{-1} to 5 Kh^{-1} .

Figure 5.20 shows the normalised frequency deviation of the 10-MHz signal produced by the IFR and HP synthesisers from the original reference signal produced by the hydrogen maser HM2 averaged over 5120 seconds as a function of time. Both synthesisers were tested over a period of 7 days. One can see that the normalised frequency deviation of the IFR synthesiser is spread within $\pm 1 \times 10^{-15}$ while the HP synthesiser gives a spread of $\pm 2 \times 10^{-15}$.

In summary, each type of test performed demonstrated that the IFR synthesiser was more suitable for accurate frequency measurements than the HP synthesiser. For averaging times longer than 640 seconds the IFR synthesiser noise did not affect the stability of the maser signal delivered to the combs laboratory, while the excess instability of the HP synthesiser was higher than that calculated for the DS-100 distribution amplifier for averaging times up to 20480 s. The temperature-dependent frequency shift of the IFR synthesiser demonstrated a fractional frequency

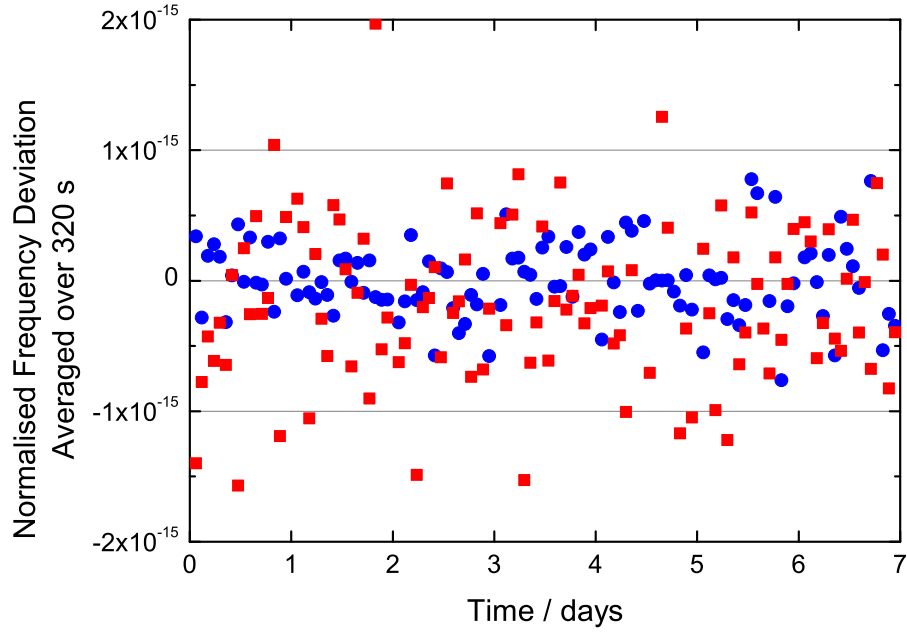


Figure 5.20: Normalised frequency deviation of the 10 MHz signal from the IFR synthesiser (blue) and the HP synthesiser (red) from the reference signal produced by hydrogen maser HM2 averaged over 5120 seconds as a function of time.

change of $4.1(0.7) \times 10^{-16} \text{ (K/h)}^{-1}$ corresponding to a fractional frequency error of $1.4(0.5) \times 10^{-15}$ for a rate of temperature change of 3.5 Kh^{-1} compared to $3.3(0.2) \times 10^{-14} \text{ (K/h)}^{-1}$ and $1.16(0.14) \times 10^{-13}$ for the same rate of temperature change in the case of the HP synthesiser. Finally, the spread of the normalised frequency deviation of synthesiser signal from the original maser signal measured under normal laboratory conditions was $\pm 1 \times 10^{-15}$ for the IFR synthesiser compared to $\pm 2 \times 10^{-15}$ for the HP synthesiser.

These results show that when an optical frequency is measured relative to a hydrogen maser calibrated using UTC, as in the case of the measurements reported in [11] and described in Chapter 6, the fractional frequency error introduced by the temperature-dependent frequency shift of the IFR synthesiser is lower than the accuracy of the measurements, therefore there is no need for synthesiser frequency corrections. However, when a hydrogen maser frequency is calibrated using the caesium fountain as

in the case of the $^{171}\text{Yb}^+$ trapped ion frequency measurements reported in [152], the accuracy of the measurements (1.0×10^{-15}) is of the same order as the temperature-dependent frequency error; hence the synthesiser signal should be monitored for corrections to the systematic frequency shift and consequently the measured repetition rate of the comb.

5.4 Conclusions

In this chapter sources of systematic uncertainty and potential errors in absolute frequency measurements were described. The uncertainty budget of the NPL-CsF2 caesium fountain was detailed. The systematic uncertainty of 2.3×10^{-16} sets a limit to the accuracy of absolute optical frequency measurements performed using a frequency comb referenced to a hydrogen maser that is simultaneously calibrated using the Cs fountain.

Limitations to the accuracy of frequency measurements made relative to a reference signal generated by a GPS-disciplined oscillator system were analysed, showing that the NPL GPS-referenced frequency comb is capable of measuring optical frequencies to a relative accuracy of 4×10^{-12} .

The stability and accuracy of the 10-MHz reference signal from a hydrogen maser delivered into the combs laboratory was analysed. It was shown that the noise in the maser signal distribution system and the link from the combs laboratory back to the phase comparator led to excess instability of the maser signal. Since no significant difference between the excess instability of the signal after the DS-100 distribution amplifier measured on week-days and during weekends was observed, as one would expect in the case of environmental noise, the excess noise was attributed to the inherent noise of the DS-100 distribution amplifier. The measured Allan deviation of the signal after the DS-100 distribution amplifier from the original maser signal was about 1.5 times higher than the Allan deviation of the maser signal measured

against itself for all averaging times. The fluctuations of the signal frequency observed during the day were within the spread of the normalised frequency deviation of the signal after the DS-100 distribution amplifier from the original maser signal. A spread of $\pm 1.5 \times 10^{-15}$ was measured for an observation period of 25 days. The tests of the FDA-1050 distribution amplifier showed that for averaging times longer than 640 seconds the excess noise of the FDA-1050 distribution amplifier neither contributed to the fractional frequency instability of the 10-MHz maser signal delivered in the combs laboratory nor introduced additional systematic frequency shifts.

Finally, the performance of two synthesisers, the IFR 2023A and the HP 8662A, used for the stabilisation of the frequency comb repetition rate was tested. The results showed superior performance of the IFR synthesiser for each type of test carried out. The excess instability of the signal generated by the HP synthesiser was higher than the excess instability of the maser signal delivered to the combs laboratory, while the stability of the IFR synthesiser signal was within the day-to-day spread of the maser signal stability. A fractional frequency change of $4.1(0.7) \times 10^{-16} (\text{K/h})^{-1}$ and $3.3(0.2) \times 10^{-14} (\text{K/h})^{-1}$ was measured for the IFR and the HP synthesisers respectively. The synthesiser accuracy tests under normal laboratory conditions showed the spread of the normalised frequency deviation of the IFR synthesiser signal from the original maser signal measured over a period of 7 days to be $\pm 1 \times 10^{-15}$, suggesting that this period was not long enough to observe the spread of $\pm 1.5 \times 10^{-15}$ measured for the distribution amplifiers. In contrast, for the HP synthesiser a spread of $\pm 2 \times 10^{-15}$ was measured indicating that the increase of the observation time might result in an even higher value.

These results show that the fractional frequency error introduced by the temperature-dependent frequency shift of the IFR synthesiser is lower than the accuracy of the measurements in the case of measurement relative to a hydrogen maser calibrated using UTC, as for the case of the measurements reported in [11] and described in Chapter 6, therefore there is no need for synthesiser frequency corrections. However, when a hydrogen maser frequency is calibrated using the caesium fountain as in the

case of the $^{171}\text{Yb}^+$ trapped ion frequency measurements reported in [152], the accuracy of the measurements (1.0×10^{-15}) is of the same order as the temperature-dependent frequency error; hence the synthesiser signal should be monitored for corrections to the systematic frequency shift and consequently the measured repetition rate of the comb.

Chapter 6

Absolute frequency measurement of the 436 nm clock transition in a single $^{171}\text{Yb}^+$ ion

In this chapter an absolute frequency measurement of the electric quadrupole clock transition at 436 nm in a frequency standard based on a single $^{171}\text{Yb}^+$ trapped ion is described. The emphasis of this chapter is on the measurements of the transition frequency and the methods used to correct for errors in the reference signal used during the measurements. These are the parts of the experiment I was involved with. The running of the ion trap and analysis of the collected data, including the estimates of the systematic shifts affecting the frequency of the clock transition, were performed by other members of the group. The full details of this part of the experiment are reported in [11] and only a brief description necessary for understanding the experiment is given here.

Firstly, a description of the $^{171}\text{Yb}^+$ optical frequency standard is given. Next, the preparation of the ion and detection of the clock signal are described. After that, the frequency measurements and the method of frequency correction using data from

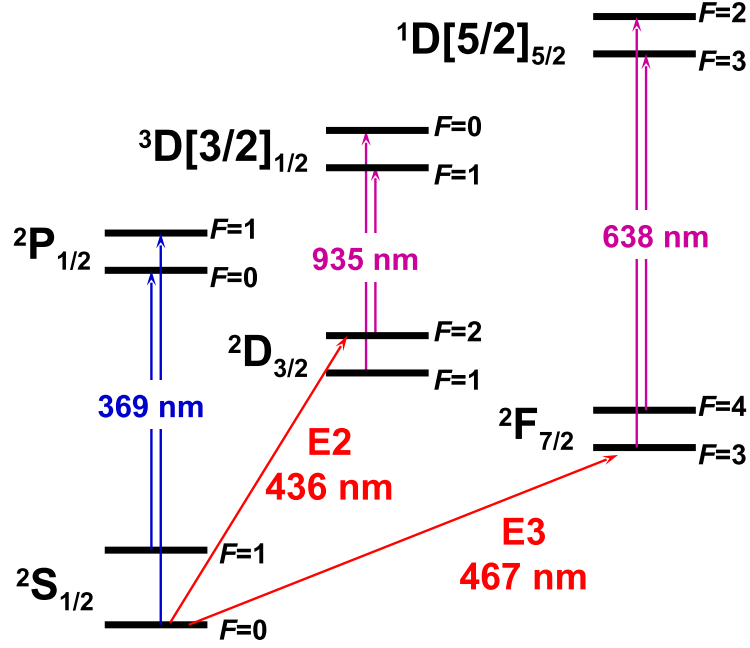


Figure 6.1: Partial term scheme for $^{171}\text{Yb}^+$ showing the electric quadrupole (E2) and electric octupole (E3) clock transitions at 436 nm and 467 nm respectively and cooling and repumper wavelengths.

the BIPM publication Circular T are presented. Finally, the result of the absolute frequency measurement is given and compared with an independent measurement made by the PTB group.

6.1 $^{171}\text{Yb}^+$ optical frequency standard

Figure 6.1 shows a partial term scheme for the $^{171}\text{Yb}^+$ ion. The transition at 369 nm is used for Doppler cooling of the ion to a temperature of around a millikelvin, confining its motion to the bottom of the trapping potential as described in Section 2.4.1.4. However, the ion can decay from the upper level of the cooling transition to the $^2\text{D}_{3/2}$ level, therefore a repumper laser at 935 nm is used to return the ion to the ground state via the $^3\text{D}[3/2]_{1/2}$ level. Another repumper transition at 638 nm is used to drive the

ion out of the $^2F_{7/2}$ state to the the $^1D[5/2]_{5/2}$ level from which it subsequently decays to the ground state. Due to the hyperfine structure of the energy levels involved in the transitions two different laser frequencies are required for each of the cooling and repumper transition.

There are two optical clock transitions in the $^{171}\text{Yb}^+$ ion: the electric quadrupole (E2) transition at 436 nm with a natural linewidth of 3.1 Hz and the electric octupole (E3) transition at 467 nm. Due to the extremely long upper state lifetime of approximately 6 years [108], the natural linewidth of the E3 transition is of order one nanohertz.

Both clock transitions are being extensively studied at the Physikalisch-Technische Bundesanstalt (PTB), Germany and NPL, UK. The frequency of the E2 transition has been measured at PTB with a relative uncertainty of 1.1×10^{-15} [12] and two frequency standards operating on the E2 transition have been compared with a relative uncertainty of 4×10^{-16} [155]. The frequency of the E3 transition has been measured with a fractional uncertainty of about 1×10^{-15} [152, 95].

One of the applications of optical clocks is tests of fundamental physical theories. The presence of two clock transitions makes the $^{171}\text{Yb}^+$ ion particularly attractive for looking for possible time variations of the fine structure constant α , as it opens the possibility of comparing two transition frequencies in a single ion [6]. The $^2F_{7/2}$ state has the largest known sensitivity to changes in α , with the sign opposite to the dependency of the $^2D_{3/2}$ state, which results in an effective sensitivity factor larger than the sensitivity of each state. The limit to the accuracy of the measured frequency ratio is determined by the systematic uncertainties associated with the two transitions and under identical environmental conditions the sources of some of these uncertainties are the same or strongly correlated [6]. Therefore, the uncertainty of the frequency ratio measured within one ion can be reduced compared to the frequency ratio of the two independent frequency standards in two different traps.

The first step towards the frequency ratio measurements is an absolute frequency measurement of each of the clock transitions. Historically, the investigation of the $^{171}\text{Yb}^+$

ion at NPL was focused on the E3 transition [156, 157]. The first absolute frequency measurement of the E2 electric quadrupole transition at NPL [11] is described in the following sections.

6.2 Measurements of the absolute frequency of the E2 clock transition

This section describes an absolute frequency measurement of the electric quadrupole clock transition at 436 nm in a frequency standard based on a single $^{171}\text{Yb}^+$ trapped ion. Firstly, a description of the preparation of the $^{171}\text{Yb}^+$ ion and the method used for detection of the atomic transition are given. Next, the measurements of the frequency of the clock signal are described and the method of frequency correction using data from the BIPM publication Circular T is detailed. Finally, the result of the absolute frequency measurement and an outline of the applied corrections to the systematic frequency shifts are given and compared with an independent measurement made by the PTB group.

6.2.1 $^{171}\text{Yb}^+$ ion preparation and detection

A single ion is confined in an endcap trap as described in Section 2.4.1.1, and is Doppler cooled at 369 nm (see Fig. 6.1). The ion is prepared in the $^2\text{S}_{1/2}(F = 0)$ ground state with the repumper light at 935 nm present in both the cooling and the state preparation phases, after which it is probed with light from the clock laser at 436 nm. Fluorescence from the cooling transition is observed with a photomultiplier tube and quantum jumps are detected through the absence of this fluorescence as described in Section 2.4.1.5. The process of recording a potential quantum jump is divided into four periods: cooling, state preparation, probing and detection as shown in Fig. 6.2. Since the probability of the ion making the transition to the $^2\text{F}_{7/2}$ level is

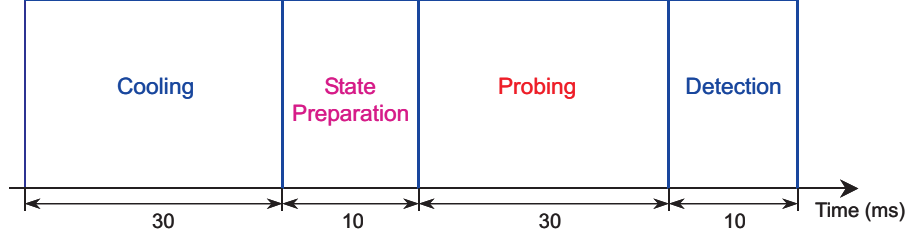


Figure 6.2: Schematic showing the timing sequence for a single quantum jump detection.

very small, the repumper light at 638 nm was only switched on when this level had to be depopulated, which happened about once a day.

The experimental arrangement used for absolute frequency measurements of the E2 clock transition in the $^{171}\text{Yb}^+$ ion is shown in Fig. 6.3. The clock laser light at 436 nm is generated by frequency doubling a diode laser at 871 nm. The frequency of the diode laser is locked to a mode of a high-finesse, ultra-low-expansion optical cavity using the Pound-Drever-Hall technique as described in Section 2.4.1.3, and is tuned by stepping a frequency offset provided by a double-passed acousto optic modulator (AOM) whilst maintaining the laser lock to the cavity. Therefore, the frequency of the clock laser light reaching the ion is given by

$$f_{436} = 2(f_{\text{cav}} + 2f_{\text{off}}), \quad (6.1)$$

where f_{cav} is the frequency of the cavity mode and f_{off} is the drive frequency of the AOM. To observe the atomic transition, the laser is repeatedly scanned over the transition and the offset frequency corresponding to individual quantum jumps is recorded. An example of such data is shown in Fig. 6.4, where the offset frequency f_{off} corresponding to individual quantum jumps is plotted as a function of time for 10 scans of the clock laser frequency across the 436 nm transition. After removal of the cavity drift the data were used to generate the atomic absorption spectrum with a 61 Hz full-width at half-maximum (FWHM) of a Lorentzian fit to the data as shown

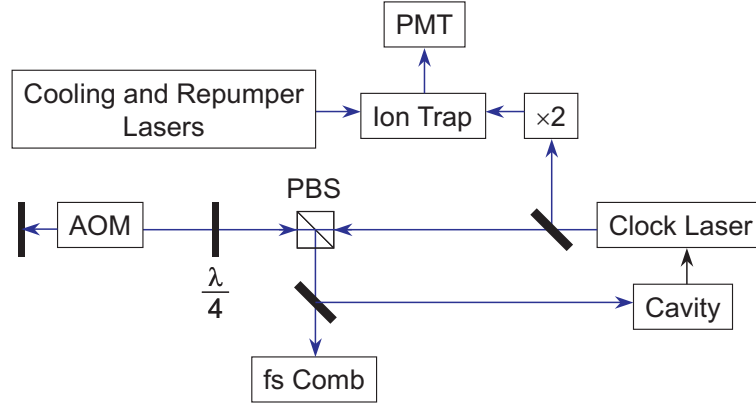


Figure 6.3: Schematic diagram of the experimental setup for frequency measurements of the electric quadrupole clock transition in the $^{171}\text{Yb}^+$ ion. AOM - acousto-optic modulator; PBS - polarizing beam-splitter; PMT - photomultiplier tube; $\times 2$ - frequency doubling. The blue lines indicate optical paths and the black line indicates an electrical signal path.

in Fig. 6.5 [11].

6.2.2 Frequency measurements and data analysis

The signal from the clock laser was transmitted to the combs lab via a fibre link and the frequency of the cavity mode f_{cav} was measured using the fibre-laser-based frequency comb described in Sec. 3.1 whilst simultaneously recording the AOM offset frequency corresponding to individual quantum jumps. As can be seen from Fig. 6.6, the cavity frequency drifts with time at a mean rate of about 0.25 Hz/s. Therefore, to minimise errors in calculations of the frequency of each quantum jump, it is vital to ensure that the data-acquisition systems for the ion trap and the optical frequency comb are synchronised. In this experiment the data collecting computers were synchronised with an uncertainty of ± 1 s. In order to test for the presence of a quadrupole shift the measurements were performed over a range of magnetic field amplitudes and orientations providing 18 independent scans across the clock transition.

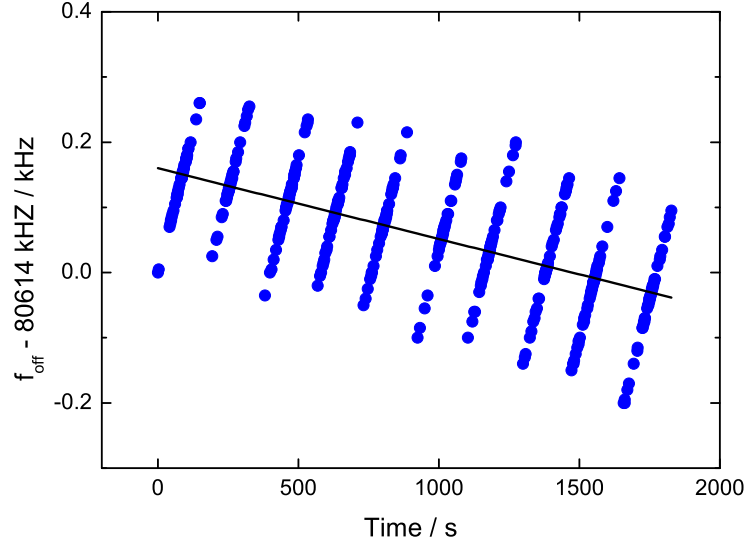


Figure 6.4: The offset frequency f_{off} corresponding to individual quantum jumps as a function of time for 10 scans of the clock laser frequency.

The measurements were carried out over a period of six days.

The result of measurements of the frequency of the optical cavity mode performed on one day is shown in Fig. 6.6.

Although the cavity drift appears linear in Fig. 6.6, the residuals of the linear fit averaged over 100 s show that the cavity demonstrates non-linear behaviour as shown in Fig. 6.7. In order to select the most appropriate curve fit, different order polynomial fits were investigated. Figure 6.8 shows the residuals for second, third and fourth order polynomial fits averaged over 100 s. One can see that going from a second order to a third order polynomial fit reduces the residuals; however increasing the order of the polynomial to four does not bring significant further improvement. Therefore, the measured cavity frequency was fitted with a third order polynomial and the result was used to calculate the frequency of each quantum jump using equation 6.1.

All synthesisers and counters used in the optical frequency comb and the synthesiser

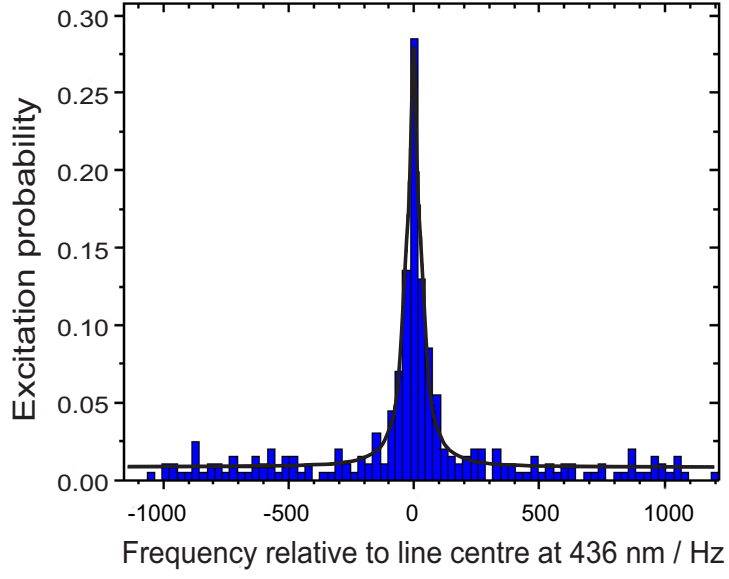


Figure 6.5: Atomic absorption spectrum of the E2 clock transition at 436 nm. The bin width is 20 Hz and the FWHM of a Lorentzian fit to the data is 61 Hz.

generating the AOM offset frequency were referenced to the 10-MHz output of the hydrogen maser which is used to generate the timescale UTC(NPL).

The result of any absolute frequency measurement must be given in the form

$$f_{\text{E2}} = k f_{\text{SI}} \quad (6.2)$$

where

$$f_{\text{SI}} \equiv 1\text{Hz} \quad (6.3)$$

is the SI unit of frequency.

In this experiment the frequency of the E2 transition was measured relative to the hydrogen maser which is used to generate the UTC(NPL) time scale, therefore the measured frequency is given by

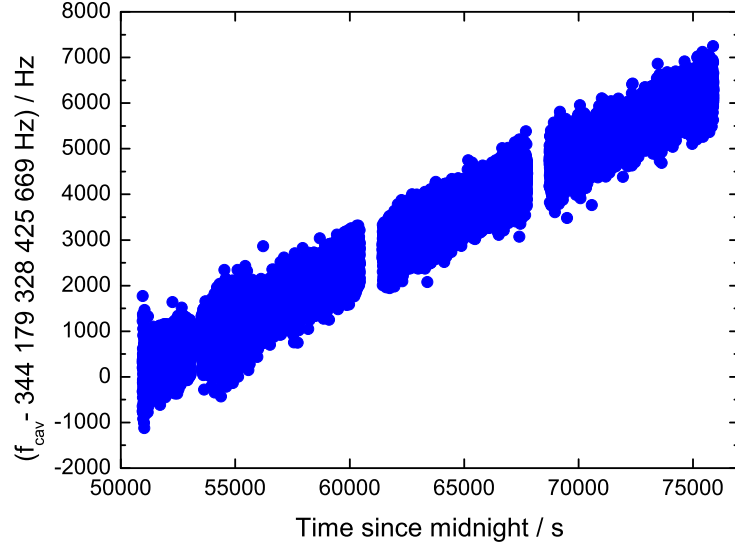


Figure 6.6: The frequency of the optical cavity mode measured by the optical frequency comb on one day of the measurement period. Each point is a 1 s average.

$$f_{\text{meas}} = k f_{\text{UTC(NPL)}}, \quad (6.4)$$

where $f_{\text{UTC(NPL)}}$ is the unit of frequency as realised via the hydrogen maser. In order to relate the measured frequency to the SI second, a correction for the difference between f_{SI} and $f_{\text{UTC(NPL)}}$ has to be applied.

6.2.3 Frequency correction using Circular T

Typically the correction to the measured frequency is made during the data processing. The difference between UTC and national timescales (including UTC(NPL)) is published by the International Bureau of Weights and Measures (BIPM) in the monthly “Circular T” bulletin [151] in the form

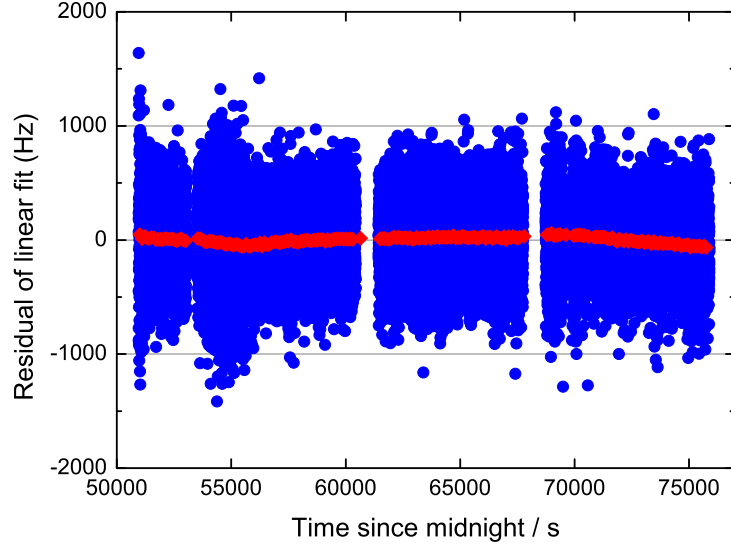


Figure 6.7: The residuals of a linear fit to the frequency comb data. Blue circles represent 1 s averaging time, red diamonds are a moving average over one hundred 1 s data points.

$$\text{UTC} - \text{UTC}(\text{NPL}) = t_{\text{offset}}, \quad (6.5)$$

with a 5 day interval between data points. The frequency difference can be calculated as

$$f_{\text{UTC}} - f_{\text{UTC}(\text{NPL})} = \frac{n}{T} - \frac{n}{T + t_{\text{offset}_2} - t_{\text{offset}_1}}, \quad (6.6)$$

where n is the number of oscillations over the period T , while t_{offset_1} and t_{offset_2} are the time differences between UTC and UTC(NPL) at the beginning and end of the period T .

Since $t_{\text{offset}_2} - t_{\text{offset}_1} \ll T$, using a Taylor series expansion equation 6.6 can be written as

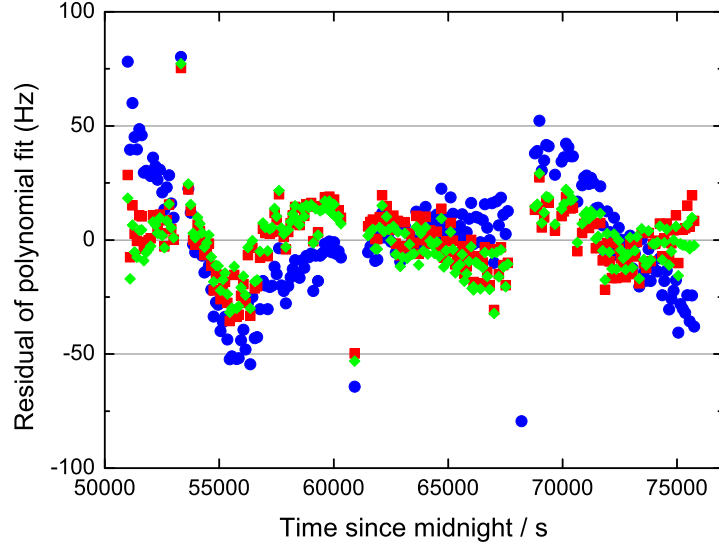


Figure 6.8: The residuals of polynomial fits to the frequency comb data. Blue circles are for a second order polynomial fit, red squares are for a third order polynomial fit and green diamonds are for a fourth order polynomial fit. Each point corresponds to an average over one hundred 1 s data points.

$$f_{\text{UTC}} - f_{\text{UTC(NPL)}} = \frac{n}{T} \frac{t_{\text{offset}_2} - t_{\text{offset}_1}}{T} = f_{\text{UTC}} \frac{\Delta t_{\text{offset}}}{T}, \quad (6.7)$$

or

$$\frac{\Delta f}{f_{\text{UTC}}} = \frac{f_{\text{UTC}} - f_{\text{UTC(NPL)}}}{f_{\text{UTC}}} = \frac{\Delta t_{\text{offset}}}{T} = \frac{dt_{\text{offset}}}{dt}. \quad (6.8)$$

Other data necessary for the frequency corrections is the fractional deviation d of the scale interval of UTC from the SI second on the geoid. The estimate of d is based on all available primary frequency standard measurements and is calculated by BIPM for the period of each Circular T (one month) by comparison of the UTC frequency with the frequencies of individual primary frequency standards. In the case when $d > 0$ the frequency of the SI second is greater than the frequency of the UTC second and

can be calculated as

$$f_{\text{SI}} = f_{\text{UTC}} + d f_{\text{SI}} \quad (6.9)$$

or

$$f_{\text{SI}} = \frac{f_{\text{UTC}}}{1 - d}. \quad (6.10)$$

Combining Eq. 6.8 and Eq. 6.10

$$f_{\text{SI}} = \frac{1}{(1 - d)} \frac{f_{\text{UTC(NPL)}}}{\left(1 - \frac{dt_{\text{offset}}}{dt}\right)}. \quad (6.11)$$

Therefore, the absolute frequency of the E2 transition is given by

$$f_{\text{E2}} = f_{\text{meas}} \frac{f_{\text{SI}}}{f_{\text{UTC(NPL)}}} \quad (6.12)$$

or

$$f_{\text{E2}} = \frac{f_{\text{meas}}}{(1 - d)\left(1 - \frac{\Delta f}{f_{\text{UTC}}}\right)}. \quad (6.13)$$

6.2.4 Results and discussion

Figure 6.9 shows the difference between UTC and its local realisation at NPL, UTC(NPL), as taken from Circular T for the period from 30/12/2007 until 28/01/2010. In order to keep UTC(NPL) as close as possible to UTC, the frequency of the clock used for the realisation of UTC(NPL), the hydrogen maser HM2, is periodically steered. These steers correspond to changes of slope in Fig. 6.9. To estimate the

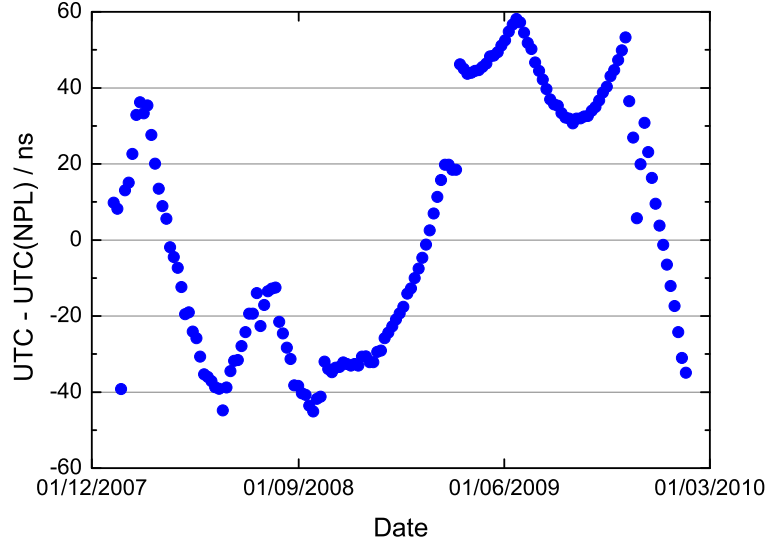


Figure 6.9: Computed values of UTC-UTC(NPL) taken from Circular T for the period from 30/12/2007 until 28/01/2010.

rate of change of the difference UTC-UTC(NPL) for each of the days of measurements the part of the graph corresponding to the period between two steering events (from 24/12/2008 until 14/03/2009) was fitted with a second order polynomial as shown in Fig. 6.10.

Figure 6.11 shows the fractional offset of the NPL maser frequency from UTC as a function of time calculated from a second order polynomial fit to data covering different periods. One can see that the calculated frequency offset depends on the data sets used for the curve fit. The spread of the values gives an estimate of the uncertainty of the frequency correction to the maser frequency. For these measurements a conservative estimate of the uncertainty of the maser frequency, also taking into account the uncertainty of d (1×10^{-15}), was 1×10^{-14} . The deviations of the maser frequency from 10 MHz for each day of measurements calculated from a second order polynomial fit to the period between two steering events (from 24/12/2008 until 14/03/2009) are given in table 6.1.

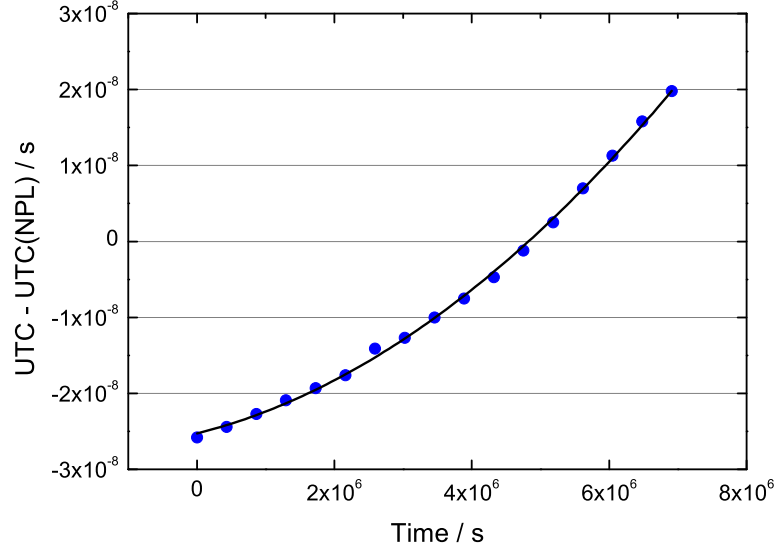


Figure 6.10: Computed values of UTC-UTC(NPL) taken from Circular T for the period from 24/12/2008 until 14/03/2009, fitted with a second order polynomial.

Apart from the correction to the maser reference frequency, there are several systematic frequency shifts that need to be taken into account when the frequency of the E2 transition is calculated from the measurement data.

Although there is no linear Zeeman shift associated with the E2 transition in $^{171}\text{Yb}^+$ ion, the second-order Zeeman shift induced by the applied magnetic field has to be corrected for. A blackbody Stark shift results from the influence of blackbody radiation arising from the temperature of environments immediately surrounding the ion. The interaction between the electric quadrupole moments of the atomic states and any residual electric field gradient present at the position of the trapped ion leads to an electric quadrupole shift. Since the quadrupole shift depends on the relative orientations of the electric field gradient and the magnetic field, its presence was tested by repeating the frequency measurements for a range of magnetic field orientations. For some of these measurements three orthogonal directions of the magnetic field were used. The analysis of these data shows no significant correlation between the

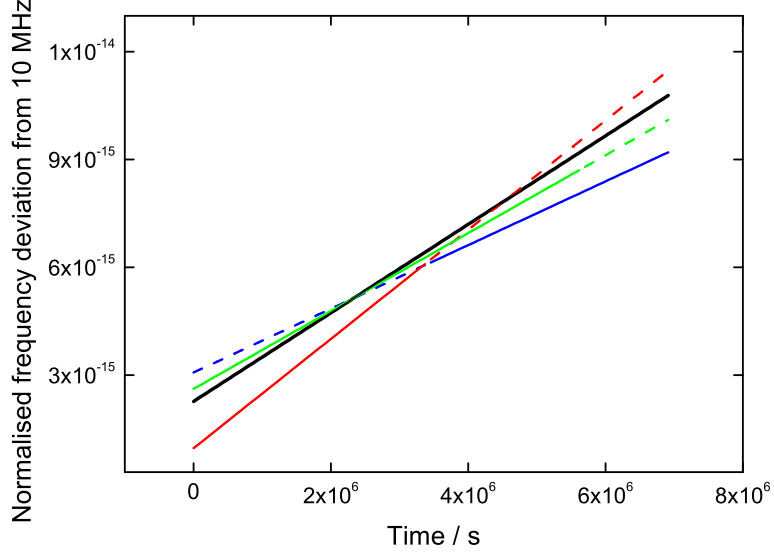


Figure 6.11: Normalised frequency deviation of the NPL maser HM2 from UTC 10-MHz, as calculated from a second order polynomial fit to Circular T data for the periods of: from 24/12/2008 until 28/01/2009 (red), from 02/02/2009 until 14/03/2009 (blue), from 24/12/2008 until 27/02/2009 (green), and from 24/12/2008 until 14/03/2009 (black). The solid lines show the part of the data used for the curve fit, the dashed lines correspond to the extrapolation.

frequency and magnetic field direction, and so the quadrupole shift is unresolved at this level of precision.

To estimate the frequency of the E2 transition each point was corrected for the second-order Zeeman shift, the deviation of the maser reference frequency from 10-MHz as determined by comparison with UTC and a blackbody Stark shift.

To give a conservative estimate of the uncertainty of the calculated frequency the maximum quadrupole shift of 3.6 Hz derived from a measurement of the secular frequencies of the ion motion in the trap was added in quadrature to the error on the weighted mean of all the data. The statistical uncertainty was calculated as a standard error on the mean of the fits to the transition frequency data and the

Day	$\Delta f/f_{\text{UTC}}$	d
11/02/2009	7.48E-15	5.2E-15
12/02/2009	7.59E-15	5.2E-15
17/02/2009	8.12E-15	5.2E-15
18/02/2009	8.23E-15	5.2E-15
19/02/2009	8.33E-15	5.2E-15
20/02/2009	8.44E-15	5.2E-15

Table 6.1: Fractional frequency corrections applied for each day of measurements.

frequency comb data. Systematic uncertainties due to the correction to the maser reference frequency (6.9 Hz) and the blackbody Stark shift (0.07 Hz) were also added in quadrature to the statistical error on the weighted mean. Other systematic shifts do not contribute significantly at this level of precision. The final value obtained for the frequency of the E2 transition is $688\,358\,979\,309\,310 \pm 9$ Hz, corresponding to a fractional uncertainty of 1.3×10^{-14} . This value is in good agreement with the value of $688\,358\,979\,309\,306.62 \pm 0.73$ Hz reported by PTB in [12]. The higher uncertainty of the measurements performed at NPL is attributed to the different method of the data acquisition where the clock laser is repeatedly scanned over the transition and its frequency is measured referenced to the hydrogen maser. The fractional uncertainty of 1.3×10^{-14} can be reduced by locking the clock laser to the clock transition as described in [158]. Also, calibrating the maser frequency using a caesium fountain would reduce the uncertainty in the reference frequency corrections.

6.3 Conclusions

In this chapter an absolute frequency measurement of the electric clock quadrupole transition at 436 nm in a frequency standard based on a single $^{171}\text{Yb}^+$ trapped ion was described. The absolute frequency of the transition was determined to be

$688\,358\,979\,309\,310 \pm 9$ Hz. This value is in good agreement with the value previously reported by PTB in [12] within the uncertainty of the measurements. The main contributions to the measurement uncertainty – the statistical uncertainty and the uncertainty in the frequency of the hydrogen maser – can be reduced by locking the clock laser to the atomic transition and direct comparison of the frequency of the transition to the frequency of the caesium fountain clock via the frequency comb.

Chapter 7

Conclusions and summary

This chapter summarises the work described in this thesis and discusses its continuation.

7.1 Technical Summary

The work described in this thesis was devoted to the investigation of femtosecond frequency combs as a tool for precise optical frequency measurements. As described in Chapter 2, in the past 14 years the frequency comb has become a commonly used tool to perform absolute frequency measurements in the optical spectral region. However, work on improvements to comb performance as well as the design of new types of combs is continuing. Chapter 2 reviews the various femtosecond laser sources used for comb generation to date from the optical clock perspective and discusses the performance, advantages and disadvantages of each type of frequency comb.

In chapter 3 the design of two of the three NPL frequency combs as they were at the start of my research project was described, highlighting their advantages and disadvantages. While one of these combs, the fibre-laser-based comb, is based on a commercially available optical frequency synthesiser, the Ti:Sapphire-laser-based

comb was designed and built from discrete optical components which allowed for improvements to be made to the overall comb performance via changes to single building blocks or redesigning of subsystems.

These improvements were described in Chapter 4. Introducing separate spectral broadening stages for detection of the carrier envelope offset frequency f_0 and for the beat signal between the comb and the measured frequency f_b led to improved SNR in both beats. However, the main emphasis of the work was the design of a novel system for f_0 detection.

Firstly, the KTP non-linear crystal used for SHG in the original f -to- $2f$ self-referencing scheme was changed for the more efficient PPKTP. The experimental comparison of the SNR in the f_0 beat generated in a Mach-Zehnder interferometer configuration confirmed the SNR enhancement resulting from this change to be 10 dB.

The next step was the design of a new self-referencing setup with better noise immunity. The new system used Wollaston prisms for compensation of the group delay between the fundamental and the frequency doubled green pulses to provide temporal overlap at the detector. The common optical path in the Wollaston prism based interferometer led to significant common-mode noise rejection, which was assessed by comparison with a Michelson interferometer based f -to- $2f$ self-referencing setup, showing significantly better short-term and long-term performance of the Wollaston prism based interferometer. Phase noise measurements of the f_0 beat signal demonstrated up to 15 dB noise reduction in the acoustic and low-frequency regions by using the Wollaston prism based interferometer rather than the Michelson interferometer-based system, illustrating the enhanced immunity of the Wollaston prism based f -to- $2f$ self-referencing setup to acoustic noise as well as air currents and thermal drifts.

Some of the sources of systematic uncertainty and frequency shifts originating from the microwave reference signal that can affect frequency measurements performed with frequency combs were investigated in Chapter 5. The stability and accuracy of the signal produced by three frequency sources, a GPS-disciplined oscillator, a hydrogen

maser and a Cs primary frequency standard, used as references for the frequency combs were evaluated. The total uncertainty for the NPL-CsF2 fountain is currently 2.3×10^{-16} , which places a limit on the accuracy of optical frequency measurements. However, during frequency measurements the NPL combs are referenced to a hydrogen maser and not directly to the Cs fountain. Since the maser is not located in the same laboratory as the combs, the signal passes through a distribution system comprising cables and a number of distribution amplifiers, which can potentially degrade its stability. The distribution system was shown to degrade the stability of the maser signal by a factor of 1.5.

As the repetition rate frequency f_{rep} is stabilised using a maser-referenced synthesiser, the synthesiser itself can be a source of frequency error. To evaluate the potential error, the temperature dependence of the accuracy of two synthesisers, the IFR 2030A and the HP 8662A, was tested. The results showed that the maximal rate of temperature change observed in the combs laboratory produced fractional frequency errors of $1.4(0.5) \times 10^{-15}$ in case of the IFR synthesiser and $1.16(0.14) \times 10^{-13}$ for the HP synthesiser. Hence, only the IFR synthesiser is suitable for accurate frequency measurements and its temperature should be stabilised and monitored during frequency measurements.

An example of an absolute frequency measurement performed with the fibre comb was described in Chapter 6. The absolute frequency of the electric quadrupole clock transition at 436 nm in a frequency standard based on a single $^{171}\text{Yb}^+$ trapped ion was determined to be $688\,358\,979\,309\,310 \pm 9$ Hz [11]. This value is in good agreement with the value previously reported by PTB in [12] within the uncertainty of the measurements. The main contributions to this uncertainty are the statistical uncertainty and the uncertainty of the hydrogen maser frequency, and can be reduced by improved design of the $^{171}\text{Yb}^+$ trapped ion experiment and calibration of the maser frequency throughout the measurement period using the local caesium fountain primary standard. Some of these improvements have since been implemented and are described in detail in [152]. With these improvements, the total relative standard uncertainty of

the octupole transition frequency in a single $^{171}\text{Yb}^+$ trapped ion was evaluated to be 1.0×10^{-15} , an improvement by a factor of 20 compared to the previously published value for this transition [157]. A similar level of uncertainty reduction can be expected when the electric quadrupole clock transition in a $^{171}\text{Yb}^+$ trapped ion is remeasured.

7.2 Further Work

A logical continuation of the work described in this thesis could be further improvements to the noise performance of the low repetition rate Ti:sapphire frequency comb. Below some of these improvements which have been already implemented at NPL during the time passed since the work described in this thesis was finished are described. The results of the work described in Chapter 4 were also used to upgrade the self-referencing scheme of the third NPL frequency comb (a higher repetition rate Ti:sapphire comb), where the original Mach-Zehnder interferometer was replaced by a Wollaston prism based interferometer.

The whole of the low repetition rate Ti:sapphire comb has now been enclosed in a wooden box lined with acoustic foam. The repetition rate frequency detection is realised via detection of the harmonic of the repetition rate and mixing this frequency with another frequency from an RF synthesiser to obtain a low frequency difference signal. This method allows f_{rep} to be measured with a precision greater than can be achieved by direct counting. The original scheme was designed to detect the beat at the ninth harmonic of f_{rep} (Sec. 3.2.2.1), however using a higher harmonic of the repetition rate gives better resolution for the f_{rep} detection. This change was implemented on both the low repetition rate Ti:sapphire comb and the fibre comb, providing a detected signal at approximately 8 GHz, which required new high speed photodetectors. Also, the counters used for the f_0 , f_b and f_{rep} measurements have been changed to new zero dead-time counters.

The absolute frequency of the octupole transition frequency in a single $^{171}\text{Yb}^+$ trapped

ion has been measured simultaneously using the low repetition rate Ti:sapphire comb and the fibre comb which were referenced to a common maser-referenced RF synthesiser [152]. The values measured with each of the two combs agreed to the level of 1.0×10^{-17} , demonstrating that the combs themselves introduced negligible uncertainty. The total relative standard uncertainty of the octupole transition frequency in a single $^{171}\text{Yb}^+$ trapped ion was evaluated to be 1.0×10^{-15} , an improvement by a factor of 20 compared to the previously published value for this transition [157]. A similar level of uncertainty reduction can be expected when the electric quadrupole clock transition in an $^{171}\text{Yb}^+$ trapped ion is remeasured. However, the uncertainty introduced by the RF frequency distribution and the uncertainty in the frequency of the microwave reference signal places a limit on the accuracy of absolute optical frequency measurements.

Improvements in accuracy and short-term stability can be achieved by direct measurement of the ratio of optical frequencies instead of measuring the absolute frequencies of two transitions and then taking the ratio. For example, two combs were used to measure the ratio of the frequencies of the lasers used to probe the quadrupole and octupole clock transitions in $^{171}\text{Yb}^+$ ion. Initial measurements demonstrated agreement between two combs at the 2.0×10^{-19} level. This result shows that the frequency uncertainty of the combs does not limit the accuracy of neither an absolute optical frequency measurements or the optical frequency ratio measurements.

Bibliography

- [1] H. S. Margolis. Optical frequency standards and clocks. *Contemporary Physics*, 51:37–58, 2010.
- [2] P. Gill. When should we change the definition of the second? *Phil. Trans. R. Soc. A*, 369:4109–4130, 2011.
- [3] G. K. Campbell and W. D. Phillips. Ultracold atoms and precise time standards. *Phil. Trans. R. Soc. A*, 369:4078–4089, 2011.
- [4] H. Katori, M. Takamoto, V.G. Palchikov, and V.D. Ovsiannikov. Ultrastable optical clock with neutral atoms in an engineered light shift trap. *Phys. Rev. Lett.*, 91:173005, 2003.
- [5] J. L. Flowers and B. Petley. Progress in our knowledge of the fundamental constants of physics. *Rep. Prog. Phys.*, 64:1191–1246, 2001.
- [6] S. N. Lea. Limits to time variation of fundamental constants from comparison of atomic frequency standards. *Rep. Prog. Phys.*, 70:1473–1523, 2007.
- [7] T. M. Fortier, N. Ashby, J. C. Bergquist, M. J. Delaney, S. A. Diddams, T. P. Heavner, L. Hollberg, W. M. Itano, S. R. Jefferts, K. Kim, F. Levi, L. Lorini, W. H. Oskay, T. E. Parker, J. Shirley, and J. E. Stalnaker. Precision atomic spectroscopy for improved limits on variation of the fine structure constant and local position invariance. *Phys. Rev. Lett.*, 98:070801, 2007.

- [8] A. Antognini, F. Nez, K. Schuhmann, F. D. Amaro, F. Biraben, J. M. R. Cardoso, D. S. Covita, A. Dax, S. Dhawan, M. Diepold, L. M. P. Fernandes, A. Giesen, A. L. Gouvea, T. Graf, T. W. Hänsch, P. Indelicato, L. Julien, C.-Y. Kao, P. Knowles, F. Kottmann, E.-O. Le Bigot, Y.-W. Liu, J. A. M. Lopes, L. Ludhova, C. M. B. Monteiro, F. Mulhauser, T. Nebel, P. Rabinowitz, J. M. F. dos Santos, L. A. Schaller, C. Schwob, D. Taqqu, J. F. C. A. Veloso, J. Vogelsang, and R. Pohl. Proton structure from the measurement of 2S-2P transition frequencies of muonic hydrogen. *Science*, 339:417–420, 2013.
- [9] Bureau International des Poids et Mesures. Comptes rendus de la 17^e CGPM (1983, resolution 1).
- [10] V. Tsatourian, H.S. Margolis, G. Marra, D.T. Reid, and P. Gill. Common-path self-referencing interferometer for carrier-envelope offset frequency stabilization with enhanced noise immunity. *Opt. Lett.*, 35:1209–1211, 2010.
- [11] S. Webster, R. Godun, S. King, G. Huang, B. Walton, V. Tsatourian, H. Margolis, S. Lea, and P. Gill. Frequency measurement of the $^2S_{1/2}$ – $^2D_{3/2}$ electric quadrupole transition in a single $^{171}\text{Yb}^+$ ion. *IEEE Trans. Ultrason. Ferroelec. and Freq. Contr.*, 57:592–599, 2010.
- [12] C. Tamm, S. Weyers, B. Lipphardt, and E. Peik. Stray-field induced quadrupole shift and absolute frequency of the 688–THz $^{171}\text{Yb}^+$ single ion optical frequency standard. *Phys. Rev. A*, 80:043403, 2009.
- [13] Bureau International des Poids et Mesures. Comptes rendus de la 13^e CGPM (1967/68, resolution 1; CR, 103).
- [14] R. A. Nelson, D. D. McCarthy, S. Malys, J. Levine, B. Guinot, H. F. Fliegel, R. L. Beard, and T. R. Bartholomew. The leap second: its history and possible future. *Metrologia*, 38:509–529, 2001.
- [15] F. Riehle. *Frequency Standards Basics and Applications*. WILEY-VCH Verlag GmbH & Co. KGaA, 2004.

- [16] Th. Udem, R. Holzwarth, and T. W. Hänsch. Optical frequency metrology. *Nature*, 416:233–237, 2002.
- [17] H Schnatz. Measurement of optical frequencies and frequency ratios. *Meas. Sci Technol*, 14:1200–1215, 2003.
- [18] L. Hollberg, S. Diddams, A. Bartels, T. Fortier, and K. Kim. The measurement of optical frequencies. *Metrologia*, 42:S105–S124, 2005.
- [19] S. T. Cundiff, J. Ye, and J. L. Hall. Optical frequency synthesis based on mode-locked lasers. *Rev. Sci. Instrum.*, 72:3749–3771, 2001.
- [20] J. L. Hall. Optical frequency measurement: 40 years of technology revolutions. *IEEE J. Selected Topics Quantum Electron*, 6:1136–1144, 2000.
- [21] T. W. Hänsch. Nobel lecture: passion for precision. *Rev. Mod. Phys.*, 78:1297–1309, 2006.
- [22] J. L. Hall. Nobel lecture: defining and measuring optical frequencies. *Rev. Mod. Phys.*, 78:1279–1295, 2006.
- [23] D. A. Jennings, K. M. Evenson, and D. J. E. Knight. Optical frequency measurements. *Proceedings of the IEEE*, 74:168–179, 1986.
- [24] L. O. Hocker, A. Javan, D. Ramachandra Rao, L. Frenkel, and T. Sullivan. Absolute frequency measurement and spectroscopy of gas laser transitions in the far infrared. *Appl. Phys. Lett.*, 10:147–149, 1967.
- [25] K. M. Evenson, G. W. Day, J. S. Wells, and L. O. Mullen. Extension of absolute frequency measurements to the cw He-Ne laser at 88 THz (3.39 μm). *Appl. Phys. Lett.*, 20:133–134, 1972.
- [26] K. M. Evenson, J. S. Wells, F. R. Petersen, B. L. Danielson, and G. W. Day. Accurate frequencies of molecular transitions used in laser stabilization: the 3.39 μm transition in CH_4 and the 9.33– and 10.18 μm transitions. *Appl. Phys. Lett.*, 22:192–196, 1973.

- [27] K. M. Baird, K. M. Evenson, G. R. Hanes, D. A. Jennings, and F. R. Petersen. Extension of absolute-frequency measurements to the visible: frequencies of ten hyperfine components of iodine. *Opt. Lett.*, 4:263–364, 1979.
- [28] B. G. Whitford. Uncertainty in frequency measurements at 88 THz made with the NRC frequency chain: frequency of the NCR He-Ne/CH₄ laser. *Metrologia*, 30:145–154, 1993.
- [29] D. A. Jennings, C. R. Pollock, F. R. Petersen, R. E. Drullinger, K. M. Evenson, J. S. Wells, J. L. Hall, and H P Layer. Direct frequency-measurement of the I₂-stabilized He-Ne 473-THz (633-nm) laser. *Opt. Lett.*, 8:136–138, 1983.
- [30] O. Acef, J. J. Zondy, M. Abed, D. G. Rovera, A. H. Gerard, A. Clairon, Ph. Laurent, Y. Millerioux, and P. Juncar. A CO₂ to visible optical frequency synthesis chain: accurate measurement of the 473 THz He-Ne/I₂ laser. *Opt. Commun.*, 97:29–34, 1993.
- [31] C. O. Weiss, G. Kramer, B. Lipphardt, and E. Garcia. Frequency measurement of a CH₄ hyperfine line at 88 THz “optical clock”. *IEEE J. Quantum Electron.*, 24:1970–1972, 1988.
- [32] H. Schnatz, B. Lipphardt, J. Helmcke, F. Riehle, and G. Zinner. First phase-coherent frequency measurement of visible radiation. *Phys. Rev. Lett.*, 76:18–21, 1996.
- [33] T. G. Blaney, C. C. Bradley, G. J. Edwards, B. W. Jolliffe, D. J. E. Knight, W. R. C. Rowley, K. C. Shotten, and P. T. Woods. Measurement of the speed of light. *Nature*, 251:46, 1974.
- [34] H. R. Telle, D. Meschede, and T. W. Hänsch. Realization of a new concept for visible frequency division: phase locking of harmonic and sum frequencies. *Opt. Lett.*, 15:532–534, 1990.
- [35] N. C. Wong. Optical frequency division using an optical parametric oscillator. *Opt. Lett.*, 15:1129–1131, 1990.

- [36] D. A. van Baak and L. Hollberg. Proposed sum-and-difference method for optical-frequency measurement in the near infrared. *Opt. Lett.*, 19:1586–1588, 1994.
- [37] C. Koch and H. R. Telle. Four-wave mixing in laser diodes for difference-frequency synthesis. *J. Opt. Soc. Am. B*, 13:1666–1678, 1996.
- [38] M. Kourogi, K. Nakagawa, and M. Ohtsu. Wide-span optical frequency comb generator for accurate optical frequency difference measurement. *IEEE J. Quantum Electron.*, 29:2693–2701, 1993.
- [39] M. Kourogi, B. Widiyatomo, Y. Takeuchi, and M. Ohtsu. Limit of optical frequency comb generation due to material dispersion. *IEEE J. Quantum Electron.*, 31:2120–2126, 1995.
- [40] K. Imai, M. Kourogi, and M. Ohtsu. 30-THz span optical frequency comb generation by self-phase modulation in an optical fiber. *IEEE J. Quantum Electron.*, 34:54–60, 1998.
- [41] Robert Thomson, Christopher Leburn, and Derryck Reid. *Ultrafast Nonlinear Optics*, chapter Chapter 4: Advances in Solid-State Ultrafast Laser Oscillators, pages 73–103. Springer, 2013.
- [42] Anthony E. Siegman. *Lasers*, chapter Chapter 27: Active Laser Mode Coupling, pages 1041–1103. Oxford University Press, 1986.
- [43] J. N. Eckstein, A. I. Ferguson, and T. W. Hänsch. High-resolution 2-photon spectroscopy with picosecond light-pulses. *Phys. Rev. Lett.*, 40:847–850, 1978.
- [44] D. E. Spence, J. M. Evans, W. E. Sleat, and W. Sibbett. Regeneratively initiated self-mode-locked Ti:sapphire laser. *Opt. Lett.*, 16:1762–1764, 1991.
- [45] D. E. Spence, P. N. Kean, and W. Sibbett. 60-fsec pulse generation from a self-mode-locked Ti:sapphire laser. *Opt. Lett.*, 16:42–44, 1991.

- [46] T. Udem, J. Reichert, R. Holzwarth, and T. W. Hänsch. Accurate measurement of large optical frequency differences with a mode-locked laser. *Opt. Lett.*, 24:881–883, 1999.
- [47] R. Holzwarth T. Udem, J. Reichert and T. W. Hänsch. Absolute optical frequency measurement of the cesium D₁ line with a mode-locked laser. *Phys. Rev. Lett.*, 82:3568–3571, 1999.
- [48] S. T. Cundiff and J. Ye. Femtosecond optical frequency combs. *Rev. Mod. Phys.*, 75:325–342, 2003.
- [49] D. J. Jones, S. A. Diddams, J. K. Ranka, A. Stentz, R. S. Windeler, J. L. Hall, and S. T. Cundiff. Carrier-envelope phase control of femtosecond mode-locked lasers and direct optical frequency synthesis. *Science*, 288:635–639, 2000.
- [50] H. R. Telle, G. Steinmeyer, A. E. Dunlop, J. Stenger, D. H. Sutter, and U. Keller. Carrier-envelope offset phase control: A novel concept for absolute optical frequency measurement and ultrashort pulse generation. *Appl. Phys. B*, 69:327–332, 1999.
- [51] A. Apolonski, A. Poppe, G. Tempea, Ch. Spielmann, Th. Udem, R. Holzwarth, T. W. Hänsch, and F. Krausz. Controlling the phase evolution of few-cycle light pulses. *Phys. Rev. Lett.*, 85:740–743, 2000.
- [52] J. C. Knight, T. A. Birks, P. St. J. Russell, and D. M. Atkin. All-silica single-mode optical fiber with photonic crystal cladding. *Opt. Lett.*, 21:1547–1549, 1996.
- [53] J. K. Ranka, R. S. Windeler, and A. J. Stentz. Visible continuum generation in air-silica microstructure optical fibers with anomalous dispersion at 800 nm. *Opt. Lett.*, 25:25–27, 2000.
- [54] T. A. Birks, J. C. Knight, and P. St. J. Russell. Endlessly single-mode photonic crystal fiber. *Opt. Lett.*, 22:961–963, 1997.

- [55] L. Matos, D. Kleppner, O. Kuzucu, T. R. Schibli, J. Kim, E. P. Ippen, and F. X. Kärtner. Direct frequency comb generation from an octave-spanning, prismless Ti:sapphire laser. *Opt. Lett.*, 29:1683–1685, 2004.
- [56] T. M. Fortier, A. Bartels, and S. A. Diddams. Octave-spanning Ti:sapphire laser with a repetition rate > 1 GHz for optical frequency measurements and comparisons. *Opt. Lett.*, 31:1011–1013, 2006.
- [57] A. Bartels and H. Kurz. Generation of a broadband continuum by a Ti:sapphire femtosecond oscillator with a 1-GHz repetition rate. *Opt. Lett.*, 27:1839–1841, 2002.
- [58] J. Reichert, R. Holzwarth, T. Udem, and T. W. Hänsch. Measuring the frequency of light with mode-locked lasers. *Opt. Commun.*, 172:59–68, 1999.
- [59] L. Xu, Ch. Spielmann, A. Poppe, T. Brabec, F. Krausz, and T. W. Hänsch. Route to phase control of ultrashort light pulses. *Opt. Lett.*, 21:2008–2010, 1996.
- [60] R. Holzwarth, T. Udem, T. W. Hänsch, J. C. Knight, W. J. Wadsworth, and P. St. J Russell. Optical frequency synthesizer for precision spectroscopy. *Phys. Rev. Lett.*, 85:2264–2267, 2000.
- [61] A. Poppe, R. Holzwarth, A. Apolonski, G. Tempea, C. Spielmann, T. W. Hänsch, and F. Krausz. Few-cycle optical waveform synthesis. *Appl. Phys. B*, 72:373–376, 2001.
- [62] U. Morgner, R. Ell, G. Metzler, T.R. Schibli, F.X. Kärtner, J.G. Fujimoto, H.A. Haus, and E.P. Ippen. Nonlinear optics with phase-controlled pulses in the sub-two-cycle regime. *Phys. Rev. Lett.*, 86:5462–5465, 2001.
- [63] A. Bartels, D. Heinecke, and S. A. Diddams. 10-GHz self-referenced optical frequency comb. *Science*, 326:681, 2009.

- [64] B. R. Washburn, S. A. Diddams, N. R. Newbury, J. W. Nicholson, M. F. Yan, and C. G. Jørgensen. Phase-locked, erbium-fiber-laser-based frequency comb in the near infrared. *Opt. Lett.*, 29:250–252, 2004.
- [65] W.C. Swann, J.J. McFerran, I. Coddington, N.R. Newbury, I. Hartl, M.E. Fermann, P.S. Westbrook, J.W. Nicholson, F.S. Feder, C. Langrock, and M.M. Fejer. Fiber-laser frequency combs with subhertz relative linewidths. *Opt. Lett.*, 31:3046–3048, 2006.
- [66] A. Ruehl, A. Marcinkevicius, M. E. Fermann, and I. Hartl. 80 W, 120 fs Yb-fiber frequency comb. *Opt. Lett.*, 35:3015–3017, 2010.
- [67] H.-W. Chen, G. Chang, S. Xu, Z. Yang, and F. X. Krtner. 3 ghz, fundamentally mode-locked, femtosecond Yb-fiber laser. *Opt. Lett.*, 37:3522–3524, 2012.
- [68] I. Hartl, H. A. McKay, R. Thapa, B. K. Thomas, A. Ruehl, L. Dong, and M. E. Fermann. Fully stabilized GHz Yb-fiber laser frequency comb. *Advanced Solid-State Photonics*, OSA Technical Digest Series (CD):MF9, 2009.
- [69] D. Chao, M. Sander, G. Chang, J. Morse, J. Cox, G. Petrich, L. Kolodziejski, F. Kaertner, and E. Ippen. Self-referenced erbium fiber laser frequency comb at a GHz repetition rate. *OFC2012*, page OW1C.2, 2012.
- [70] A. Cingoz, D. C. Yost, T. K. Allison, A. Ruehl, M. E. Fermann, I. Hartl, and J. Ye. Broadband phase noise suppression in a Yb-fiber frequency comb. *Opt. Lett.*, 36:743–745, 2011.
- [71] R. Holzwarth, M. Zimmermann, Th. Udem, T. W. Hänsch, P. Russbuldt, K. Gabel, R. Poprawe, J. C. Knight, W. J. Wadsworth, and P. S. J. Russell. White-light frequency comb generation with a diode-pumped Cr:LiSAF laser. *Opt. Lett.*, 26:1376–1378, 2001.
- [72] K. L. Corwin, I. Thomann, T. Dennis, R. W. Fox, W. Swann, E. A. Curtis, C. W. Oates, G. Wilpers, A. Bartels, S. L. Gilbert, L. Hollberg, N. R. Newbury, S. A.

- Diddams, J. W. Nicholson, and M. F. Yan. Absolute-frequency measurements with a stabilized near-infrared optical frequency comb from a Cr:forsterite laser. *Opt. Lett.*, 29:397–399, 2004.
- [73] S. A. Meyer, J. A. Squier, and S. A. Diddams. Diode-pumped Yb:KYW femtosecond laser frequency comb with stabilized carrier-envelope offset frequency. *Eur. Phys. J. D*, 48:19–26, 2008.
- [74] S. Schilt, N. Bucalovic, V. Dolgovskiy, Ch. Schori, M. C. Stumpf, G. Di Domenico, S. Pekarek, A. E. H. Oehler, Th. Südmeyer, U. Keller, and P. Thomann. Fully stabilized optical frequency comb with sub-radian ceo phase noise from a sesam-modelocked $1.5 - \mu\text{m}$ solid-state laser. *Opt. Express*, 19:24171–24181, 2011.
- [75] S. Pekarek, T. Sudmeyer, S. Lecomte, S. Kundermann, J. M. Dudley, and U. Keller. Self-referenceable frequency comb from a gigahertz diode-pumped solid-state laser. *Opt. Express*, 19:16491–16497, 2011.
- [76] W. Paul. Electromagnetic traps for charged and neutral particles. *Rev. Mod. Phys.*, 62:531–540, 1990.
- [77] N. Yu and W. Nagourney. Analysis of Paul-Straubel trap and its variations. *J. Appl. Phys.*, 77:3623–3630, 1995.
- [78] C. Schrama, E. Peik, W.W. Smith, and H. Walther. Novel miniature ion traps. *Opt. Commun.*, 101:32–36, 1993.
- [79] J.D. Prestage, G.J. Dick, and L. Maleki. New ion trap for frequency standard applications. *J. Appl. Phys.*, 66:1013–1017, 1989.
- [80] L. Hollberg, C. W. Oates, E. A. Curtis, E. N. Ivanov, S. A. Diddams, T. Udem, H. G. Robinson, J. C. Bergquist, R. J. Rafac, W. M. Itano, R. E. Drullinger, and D. J. Wineland. Optical frequency standards and measurements. *IEEE J. Quantum Electron.*, 37:1502–1512, 2001.

- [81] H. Katori. Spectroscopy of strontium atoms in the Lamb-Dicke confinement. In P.Gill, editor, *Proceedings of the 6th Symposium on Frequency Standards and Metrology*, pages 323–330. World Scientific, 2002.
- [82] M. Takamoto and H. Katori. Spectroscopy of the 1S_0 – 3P_0 clock transition of ^{87}Sr in an optical lattice. *Phys. Rev. Lett.*, 91:223001, 2003.
- [83] R.W.P. Drever, J.L. Hall, F.W. Kowalski, J. Hough, G.M. Ford, A.J. Munley, and H. Ward. Laser phase and frequency stabilization using an optical resonator. *Appl. Phys. B*, 31:97–105, 1983.
- [84] S.A. Webster, M. Oxborrow, and P. Gill. Vibration-insensitive optical cavity. *Phys. Rev. A*, 75:011801(R), 2007.
- [85] D. J. Wineland and W. M. Itano. Laser cooling of atoms. *Phys. Rev. A*, 20:1521–1540, 1979.
- [86] H.G. Dehmelt. Proposed $10^{14} \delta\nu < \nu$ laser fluorescence spectroscopy on Tl^+ mono-ion oscillator ii. *Bull. Am. Phys. Soc.*, 20:60, 1975.
- [87] W. Nagourney, J. Sandberg, and H.G. Dehmelt. Shelved electron amplifier: observation of quantum jumps. *Phys. Rev. Lett.*, 56:2797–2799, 1986.
- [88] A.L. Lance, W.D. Seal, and F. Labaar. Phase noise and AM noise measurements in the frequency domain. *Infrared and Millimetre Waves*, 11:239–289, 1984.
- [89] J. Levine. Introduction to time and frequency metrology. *Rev. Sci. Instrum.*, 70:2567–2596, 1999.
- [90] R. S. Conroy. Frequency standards, metrology and fundamental constants. *Contemporary Physics*, 44:99–135, 2003.
- [91] C. W. Chou, D. B. Hume, J. C. J. Koelemeij, D. J. Wineland, and T. Rosenband. Frequency comparison of two high-accuracy Al^+ optical clocks. *Phys. Rev. Lett.*, 104:070802, 2010.

- [92] T. Rosenband, D. B. Hume, P. O. Schmidt, C. W. Chou, A. Brusch, L. Lorini, W. H. Oskay, R. E. Drullinger, T. M. Fortier, J. E. Stalnaker, S. A. Diddams, W. C. Swann, N. R. Newbury, W. M. Itano, D. J. Wineland, and J. C. Bergquist. Frequency ratio of Al^+ and Hg^+ single-ion optical clocks; metrology at the 17th decimal place. *Science*, 319:1808–1812, 2008.
- [93] J. E. Stalnaker, S. A. Diddams, T. M. Fortier, K. Kim, L. Hollberg, J. C. Bergquist, W. M. Itano, M. J. Delany, L. Lorini, W. H. Oskay, T. P. Heavner, S. R. Jefferts, F. Levi, T. E. Parker, and J. Shirley. Optical-to-microwave frequency comparison with fractional uncertainty of 10^{-15} . *Appl. Phys. B*, 89:167–176, 2007.
- [94] A. A. Madej, P. Dube, J. E. Bernard Z. Zhou, and M. Gertsvolf. $^{88}\text{Sr}^+$ 445-Thz single-ion reference at the 10^{-17} level via control and cancellation of systematic uncertainties and its measurement against the si second. *Phys. Rev. Lett.*, 109:203002, 2012.
- [95] N. Huntemann, M. Okhapkin, B. Lipphardt, S. Weyers, Chr. Tamm, and E. Peik. High-accuracy optical clock based on the octupole transition in $^{171}\text{Yb}^+$. *Phys. Rev. Lett.*, 108:090801, 2012.
- [96] Y. Huang, Q. Liu, J. Cao, B. Ou, P. Liu, H. Guan, X. Huang, and K. Gao. Evaluation of the systematic shifts of a single- $^{40}\text{Ca}^+$ -ion frequency standard. *Phys. Rev. A*, 84:053841, 2011.
- [97] M. Chwalla, J. Benhelm, K. Kim, G. Kirchmair, T. Monz, M. Riebe, P. Schindler, A. S. Villar, W. Hänsel, C. F. Roos, R. Blatt, M. Abgrall, G. Santarelli, G. D. Rovera, and Ph. Laurent. Absolute frequency measurement of the $^{40}\text{Ca}^+$ $4s^2s_{1/2} - 3d^2d_{5/2}$ clock transition. *Phys. Rev. Lett.*, 102:023002, 2009.
- [98] J. von Zanthier, T. Becker, M. Eichenseer, A. Y. Nevsky, C. Schwedes, E. Peik, H. Walther, R. Holzwarth, J. Reichert, T. Udem, T. W. Hänsch, P. V. Pokasov,

- M. N. Skvortsov, and S. N. Bagayev. Absolute frequency measurement of the In^+ clock transition with a mode-locked laser. *Opt. Lett.*, 25:1729–1731, 2000.
- [99] R. Le Targat, L. Lorini, Y. Le Coq, M. Zawada, J. Guna, M. Abgrall, M. Gurov, P. Rosenbusch, D. G. Rovera, B. Nagrny, R. Gartman, P. G. Westergaard, M. E. Tobar, M. Lours, G. Santarelli, A. Clairon, S. Bize, P. Laurent, P. Lemonde, and J. Lodewyck. Experimenting an optical second with strontium lattice clocks. *Nature Communication*, 4:arXiv:1301.6046, 2013.
- [100] N. D. Lemke, A. D. Ludlow, Z. W. Barber, T. M. Fortier, S. A. Diddams, Y. Jiang, S. R. Jefferts, T. P. Heavner, T. E. Parker, and C. W. Oates. Spin-1/2 lattice clock. *Phys. Rev. Lett.*, 103:063001, 2009.
- [101] C. G. Parthey, A. Matveev, J. Alnis, B. Bernhardt, A. Beyer, R. Holzwarth, A. Maistrou, R. Pohl, K. Predehl, Th. Udem, T. Wilken, N. Kolachevsky, M. Abgrall, D. Rovera, Ch. Salomon, P. Laurent, and Th. W. Hänsch. Improved measurement of the hydrogen 1S-2S Transition Frequency. *Phys. Rev. Lett.*, 107:203001, 2011.
- [102] J. J. McFerran, L. Yi, S. Mejri, S. Di Manno, W. Zhang, J. Guena, Y. Le Coq, and S. Bize. Neutral atom frequency reference in the deep ultraviolet with fractional uncertainty 5.7×10^{-15} . *Phys. Rev. Lett.*, 108:183004, 2012.
- [103] G. Wilpers, C. W. Oates, S. A. Diddams, A. Bartels, T. M. Fortier, W. H. Oskay, J. C. Bergquist, S. R. Jefferts, T. P. Heavner, T. E. Parker, and L. Hollberg. Absolute frequency measurement of the neutral ^{40}Ca optical frequency standard at 657 nm based on microkelvin atoms. *Metrologia*, 44:146–151, 2007.
- [104] M. Petersen, R. Chicireanu, S. T. Dawkins, D. V. Magalhães, C. Mandache, Y. Lecoq, A. Clairon, and S. Bize. Doppler-free spectroscopy of the $^1\text{S}_0$ – $^3\text{P}_0$ optical clock transition in laser-cooled fermionic isotopes of neutral mercury. *Phys. Rev. Lett.*, 101:183004, 2008.

- [105] N. Poli, Z. W. Barber, N. D. Lemke, C. W. Oates, L. S. Ma, J. E. Stalnaker, T. M. Fortier, S. A. Diddams, L. Hollberg, J. C. Bergquist, A. Brusch, S. Jefferts, T. Heavner, and T. Parker. Frequency evaluation of the doubly forbidden 1S_0 – 3P_0 transition in bosonic ^{174}Yb . *Phys. Rev. A*, 77:050501R, 2008.
- [106] X. Baillard, M. Fouché, R. Le Targat, P. G. Westergaard, A. Lecallier, Y. Le Coq, G. D. Rovera, S. Bize, and P. Lemonde. Accuracy evaluation of an optical lattice clock with bosonic atoms. *Opt. Lett.*, 32:1812–1814, 2007.
- [107] J. Guena, M. Abgrall, D. Rovera, P. Laurent, B. Chupin, M. Lours, G. Santarelli, P. Rosenbusch, M. E. Tobar, R. Li, K. Gibble, A. Clairon, and S. Bize. Progress in Atomic Fountains at LNE-SYRTE. *IEEE T. Ultrason. Ferr.*, 59:391–410, 2012.
- [108] M. Roberts, P. Taylor, G. P. Barwood, W. R. C. Rowley, and P. Gill. Observation of the $^2S_{1/2}$ – $^2F_{7/2}$ electric octupole transition in a single $^{171}\text{Yb}^+$ ion. *Phys. Rev. A*, 62:020501, 2000.
- [109] P. O. Schmidt, T. Rosenband, C. Langer, W. M. Itano, J. C. Bergquist, and D. J. Wineland. Spectroscopy using quantum logic. *Science*, 309:749–752, 2005.
- [110] S. Bourzeix, B. de Beauvoir, F. Nez, M. D. Plimmer, F. de Tomasi, L. Julien, F. Biraben, and D. N. Stacey. High resolution spectroscopy of the hydrogen atom: determination of the 1S Lamb shift. *Phys. Rev. Lett.*, 76:384–387, 1996.
- [111] L.-S. Ma, Z. Bi, A. Bartels, K. Kim, L. Robertsson, M. Zucco, R. S. Windeler, G. Wilpers, C. Oates, L. Hollberg, and S. A. Diddams. Frequency uncertainty for optically referenced femtosecond laser frequency combs. *IEEE J. Quant. Electron.*, 43:139–46, 2007.
- [112] Menlo Systems. *Optical Frequency Synthesizer FC1500, Operation Manual Version 1.3*, June 2006.

- [113] B. R. Walton, H. S. Margolis, V. Tsatourian, and P. Gill. Transportable optical frequency comb based on a mode-locked fibre laser. *IET Optoelectronics*, 2:182–187, 2008.
- [114] S. N. Lea, W. R. C. Rowley, H. S. Margolis, G. P. Barwood, G. Huang, P. Gill, J.-M. Chartier, and R. S. Windeler. Absolute frequency measurements of 633 nm iodine-stabilized helium-neon lasers. *Metrologia*, 40:84–88, 2003.
- [115] H. S. Margolis, G. Huang, G. P. Barwood, S. N. Lea, H. A. Klein, W. R. C. Rowley, P. Gill, and R. S. Windeler. Absolute frequency measurement of the 674-nm $^{88}\text{Sr}^+$ clock transition using a femtosecond optical frequency comb. *Phys. Rev. A*, 67:032501, 2003.
- [116] K. Szymaniec, S. E. Park, G. Marra, and W. Chalupczak. First accuracy evaluation of the NPL-CsF2 primary frequency standard. *Metrologia*, 47:363–376, 2010.
- [117] V. Tsatourian, H.S. Margolis, G. Marra, D.T. Reid, and P. Gill. Noise-insensitive self-referencing interferometer for carrier envelope offset frequency stabilization of a Ti:sapphire laser. In *Lasers and Electro-Optics/Quantum Electronics and Laser Science Conference: 2010 Laser Science to Photonic Applications, CLEO/QELS 2010*, San Jose, CA, 2010.
- [118] V. Tsatourian, H. S. Margolis, S. N. Lea, B. R. Walton, G. Marra, D. T. Reid, and P. Gill. Improvements to the robustness of a Ti:Sapphire-based femtosecond comb at NPL. In L. Maleki, editor, *Proceedings of the 7th Symposium on Frequency Standards and Metrology*, pages 291–295. World Scientific, 2009.
- [119] F. W. Helbing, G. Steinmeyer, J. Stenger, H. R. Telle, and U. Keller. Carrier-envelope-offset dynamics and stabilization of femtosecond pulses. *Appl. Phys. B*, 74 [Suppl.]:S35–S42, 2002.
- [120] P. A. Franken and J. F. Ward. Optical harmonics and nonlinear phenomena. *Rev. Mod. Phys.*, 35:23–39, 1963.

- [121] T. Y. Fan, C. E. Huang, B. Q. Hu, R. C. Eckardt, Y. X. Fan, R. L. Byer, and R. S. Feigelson. Second harmonic generation and accurate index of refraction measurements in flux-grown KTiOPO_4 . *Appl. Opt.*, 26:2390–2394, 1987.
- [122] B. Wyncke and F. Brehat. Calculation of the effective second-order non-linear coefficients along the phase matching directions in acentric orthorhombic biaxial crystals. *J. Phys. B: At. Mol. Opt. Phys.*, 22:363–376, 1989.
- [123] I. Shoji, T. Kondo, A. Kitamoto, M. Shirane, and R. Ito. Absolute scale of second-order nonlinear-optical coefficients. *J. Opt. Soc. Am. B*, 14:2268–2294, 1997.
- [124] F. Brethat and B. Wyncke. Calculation of double-refraction walk-off angle along the phase-matching directions in non-linear biaxial crystals. *J. Phys. B: At. Mol. Opt. Phys.*, 22:1891–1898, 1989.
- [125] G. D. Boyd and D. A. Kleinman. Parametric interaction of focused Gaussian light beams. *J. Appl. Phys.*, 39:3597–3639, 1968.
- [126] J. Yao, W. Sheng, and W. Shi. Accurate calculation of the optimum phase-matching parameters in three-wave interactions with biaxial nonlinear-optical crystals. *J. Opt. Soc. Am. B*, 9:891–902, 1992.
- [127] M. M. Fejer, G. A. Magel, D. H. Jundt, and R. L. Byer. Quasi-phase-matched second harmonic generation: tuning and tolerances. *IEEE J. Quantum Elect.*, 28:2631–2654, 1992.
- [128] A. Arie, G. Rosenman, V. Mahal, A. Skliar, M. Oron, M. Katz, and D. Eger. Green and ultraviolet quasi-phase-matched second harmonic generation in bulk periodically-poled KTiOPO_4 . *Opt. Commun.*, 142:265–268, 1977.
- [129] G. P. Agrawal. *Fiber-optic communication systems*, chapter Chapter 4: Optical Detectors and Receivers, pages 136–184. John Wiley and Sons, Inc., 1992.

- [130] PerkinElmer silicon avalanche photodiodes datasheet. <http://www.perkinelmer.co.uk/CMSResources/Images/44-3477DTS-C30902.pdf>.
- [131] Dispersion equations for optical materials. <http://www.cvimellesgriot.com/newlineproducts/Documents/Catalog/Dispersion-Equations.pdf>.
- [132] M. Pawłowska, F. Ozimek, P. Fita, and C. Radzewicz. Collinear interferometer with variable delay for carrier-envelope offset frequency measurement. *Rev. Sci. Instrum.*, 80:083101, 2009.
- [133] E. Moon, Chengquan Li, Zuoliang Duan, J. Tackett, K. L. Corwin, B. R. Washburn, and Zenghu Chang. Reduction of fast carrier-envelope phase jitter in femtosecond laser amplifiers. *Opt. Express*, 14:9758–9763, 2006.
- [134] D. J. Jones, T. M. Fortier, and S. T. Cundiff. Highly sensitive detection of the carrier-envelope phase evolution and offset of femtosecond mode-locked oscillators. *J. Opt. Soc. Am. B*, 21:1098–1103, 2004.
- [135] T.M. Fortier, P. A. Roos, D. J. Jones, and S.T. Cundiff. Carrier-envelope phase-controlled quantum interference of injected photocurrents in semiconductors. *Phys. Rev. Lett.*, 92:147403–1, 2004.
- [136] C. Grebing, S. Koke, B. Manschwetus, and G. Steinmeyer. Performance comparison of interferometer topologies for carrier-envelope phase detection. *Appl. Phys. B*, 59:81–84, 2009.
- [137] T. R. Schibli, K. Minoshima, F.-L. Hong, H. Inaba, A. Onae, H. Matsumoto, I. Hartl, and M. E. Fermann. Frequency metrology with a turnkey all-fiber system. *Opt. Lett.*, 29:2467–2469, 2004.
- [138] T. Fuji, J. Rauschenberger, A. Apolonski, V. S. Yakovlev, G. Tempea, T. Udem, C. Gohle, T. W. Hänsch, W. Lehnert, M. Scherer, and F. Krausz. Monolithic carrier-envelope phase-stabilization scheme. *Opt. Lett.*, 30:332–334, 2005.

- [139] O. Mucke, R. Ell, A. Winter, J.-W. Kim, J. Birge, L. Matos, and F. Kärtner. Self-referenced 200 MHz octave-spanning Ti:Sapphire laser with 50 attosecond carrier-envelope phase jitter. *Opt. Express*, 13:5163–5169, 2005.
- [140] Y. Jiang, Z. Bi, L. Robertsson, and L.-S. Ma. A collinear self-referencing set-up for control of the carrier-envelope offset frequency in Ti:sapphire femtosecond laser frequency combs. *Metrologia*, 42:304–307, 2005.
- [141] M. J. Padgett and A. R. Harvey. A static fourier-transform spectrometer based on wollaston prisms. *Rev. Sci. Instrum.*, 66:2807–2811, 1995.
- [142] Calcite crystal. <http://www.redoptronics.com/Calcite-crystal.html>.
- [143] Ch. Iaconis and I. A. Walmsley. Self-referencing spectral interferometry for measuring ultrashort optical pulses. *IEEE J. Quantum Electron.*, 35:501–509, 1999.
- [144] L. Essen and J. V. L. Parry. The caesium resonator as a standard of frequency and time. *Phil. Trans. Roy. Soc. A*, 250:45–69, 1957.
- [145] T.P. Heavner, S.R. Jefferts, E.A. Donley, J. Shirley, and T.E. Parker. NIST-F1: recent improvements and accuracy evaluations. *Metrologia*, 42:411–422, 2005.
- [146] S. Weyers, V. Gerginov, N. Nemitz, R. Li, and K. Gibble. Distributed cavity phase frequency shifts of the caesium fountain PTB-CSF2. *Metrologia*, 49:82–87, 2012.
- [147] N. F. Ramsey. A molecular beam resonance method with separated oscillating fields. *Phys. Rev.*, 78:695–699, 1950.
- [148] G. Santarelli, Ph. Laurent, P. Lemonde, A. Clairon, A. G. Mann, S. Chang, A. N. Luiten, and C. Salomon. Quantum projection noise in an atomic fountain: A high stability cesium frequency standard. *Phys. Rev. Lett.*, 82:4619–4622, 1999.

- [149] R. Wynands and S Weyers. Atomic fountain clock. *Metrologia*, 42:64–79, 2005.
- [150] R Li, K. Gibble, and K. Szymaniec. Improved accuracy of the NPL-CsF2 primary frequency standard: evaluation of distributed cavity phase and microwave lensing frequency shifts. *Metrologia*, 48:283–289, 2011.
- [151] BIPM report Circular T 265. <ftp://ftp2.bipm.org/pub/tai/publication/cirt.265>.
- [152] S. A. King, R. M. Godun, S. A. Webster, H. S. Margolis, L. A. M. Johnson, K. Szymaniec, P. E. G. Baird, and P. Gill. Absolute frequency measurement of the $^2S_{1/2}$ – $^2F_{7/2}$ electric octupole transition in a single ion of $^{171}\text{Yb}^+$ with 10^{-15} fractional uncertainty. *New J. Phys.*, 14:013045, 2012.
- [153] F. Overney, Th. Schildknecht, G. Beutler, L. Prost, and U. Feller. GPS time transfer using geodetic receivers: Middle term stability and temperature dependence of the signal delays. In *Proceedings 11th European Frequency and Time Forum*, pages 504–508, 4–7 March 1997. Neuchatel, Switzerland.
- [154] E. Powers, P. Wheeler, D. Judge, and D. Matsakis. Hardware delay measurements and sensitivities in carrier phase time transfer. In *30th Annual Precise Time and Time Interval (PTTI) Meeting*, pages 293–305, 1998.
- [155] C. Tamm, B. Lipphardt, H. Schnatz, R. Wynands, S. Weyers, T. Schneider, and E. Peik. $^{171}\text{Yb}^+$ single-ion optical frequency standard at 688 THz. *IEEE Trans. Instr. Meas.*, 56:601–604, 2007.
- [156] K. Hosaka, S. A. Webster, P. J. Blythe, A. Stannard, D. Beaton, H. S. Margolis, S. N. Lea, and P. Gill. An optical frequency standard based on the electric octupole transition in $^{171}\text{Yb}^+$. *IEEE Trans. Instrum. Meas.*, 54:759–762, 2005.
- [157] K. Hosaka, S. A. Webster, A. Stannard, B. R. Walton, H. S. Margolis, and P. Gill. Frequency measurement of the $^2S_{1/2}$ – $^2F_{7/2}$ electric octupole transition in a single $^{171}\text{Yb}^+$ ion. *Phys. Rev. A*, 79:033403, 2009.

- [158] H. R. Telle, B. Lipphardt, and J. Stenger. Kerr-lens, mode-locked lasers as transfer oscillators for optical frequency measurements. *Appl. Phys. B*, 74:1–6, 2002.